Search for New Physics in Final States with One Muon and Missing Transverse Energy with CMS Data

MASTERARBEIT IN PHYSIK

von
FABIAN SCHNEIDER

vorgelegt der
Fakultät für Mathematik, Informatik und Naturwissenschaften
der Rheinisch-Westfälischen Technischen Hochschule Aachen

im Dezember 2012

angefertigt im
III. Physikalischen Institut A
Prof. Dr. Thomas Hebbeker
Zweitgutachter
Prof. Dr. Christopher Wiebusch

Zusammenfassung

In dieser Arbeit wird die Suche nach neuer Physik im Endzustand $\mu + \nu$ behandelt. Diesbezüglich potenzielle Standardmodellerweiterungen werden betrachtet. Zwei Referenzmodelle werden untersucht, zum einen Kontaktwechselwirkungen zwischen vier Fermionen, sowie in einem einfachen Vergleichsmodell der Zerfall von einem neuen, schweren geladenen Eichboson W'. Als Datensatz dienen Messungen von Proton-Proton-Kollisionen, durchgeführt im Jahr 2012 mit dem CMS-Experiment am CERN bei einer Schwerpunktsenergie von $\sqrt{s} = 8$ TeV, welche einer integrierten Luminosität von 10.3 fb^{-1} entsprechen. Da keine Abweichungen von der Vorhersage des Standardmodells entdeckt worden sind, werden Ausschlussgrenzen auf die hier betrachteten Modelle neuer Physik bestimmt. Es ergeben sich Ausschlussgrenzen auf die W'-Masse $M_{W'} < 2.9$ TeV, unter der Annahme von W-ähnlichen Kopplungen sowie auf die Energieskala der Kontaktwechselwirkung von $\Lambda < 10.0$ TeV, jeweils für ein Konfidenzintervall von 95 %. Außerdem wird durch eine Kombination mit den Ergebnissen aus dem Zerfallskanal $W' \rightarrow e\nu$ eine Verbesserung des Ausschlusslimits auf $M_{W'} < 3.0$ TeV erzielt. Ergebnisse der vorliegenden Studie mit einem Datensatz von 3.7 fb^{-1} wurden in [1] veröffentlicht.

Abstract

This analysis deals with the search for new physics in the $\mu + \nu$ final state. Regarding this, a four-fermion contact interaction is considered as a potential standard-model extension as well as the decay of a new heavy, charged gauge boson W' in a simplified reference model. The dataset comprises proton-proton collisions recorded at a center-of-mass energy of $\sqrt{s} = 8$ TeV with the CMS experiment at the LHC in 2012 corresponds to an integrated luminosity of 10.3 fb^{-1}. Since no deviations from the standard model prediction have been found, exclusion limits are set on the considered new-physics models. Exclusion limits on the W' mass of $M_{W'} < 2.9$ TeV under the assumption of W-like couplings are obtained, as well as on the contact interaction energy scale of $\Lambda < 10.0$ TeV, each for a 95 % confidence interval. Furthermore, an improvement of the exclusion limit to $M_{W'} < 3.0$ TeV is achieved by combining results with the decay channel $W' \rightarrow e\nu$. Results of the analysis with a dataset of 3.7 fb^{-1} have been published in [1].

Contents

1. Theoretical Considerations

In this chapter a brief introduction to the Standard Model of particle physics is given, based on [2, 3]. Its shortcomings are described and the possible extensions that are the subjects of this thesis are motivated.

Conventions

In particle physics it is common to describe quantities like energy and momentum in 'natural units', i.e. $\hbar = c = 1$, where $\hbar$ is the reduced Planck constant and c is the speed of light.
As a result, energies, masses and momenta can be stated in units of electron volt; 'eV' with 1 eV=$1.602 \cdot 10^{-19}$ J. In this thesis 'GeV' (Giga electron volt, i.e. 10^9 eV) and 'TeV' (Tera electron volt, i.e. 10^{12} e are the most common units.
Especially in the first chapter, electric charges are given in units of the elementary charge e=$1.602 \cdot 10^{-19}$ C.
In the next section the Einsteinian summation convention is used as a compact notation of contracting four-vectors, following:

$$A^\mu B_\mu = -\sum_{i=1}^{3} A_i \cdot B_i + A_0 \cdot B_0. \tag{1.1}$$

The CMS Coordinate System

Due to its cylindrical symmetry, points inside the detector are parametrized with polar coordinates with the origin in the nominal interaction point located in the center of the detector. The x-axis points radially towards the center of the LHC ring, while the y-axis points vertically upwards. The z-axis points along the beam pipe with direction towards the Jura mountains. ϕ denotes the angle between the x-axis and the y-axis, starting at the former and θ is the polar angle, starting at z. In practice, often the pseudorapidity η is used instead of the polar angle, which is calculated by:

$$\eta = -\ln(\tan(\frac{\theta}{2})) \tag{1.2}$$

The reason is that differences in pseudorapidity are Lorentz-invariant and therefore are the same in the center-of-mass system and in the laboratory system.

1.1. The Standard Model of Particle Physics

The Standard Model (SM) of particle physics is the very successful convergence of several theoretical constructs modelling many different observations in the world of elementary particles. It is a local, relativistic gauge theory of quantum fields and provides a description of all known matter and its interaction concerning three out of the four fundamental forces[1]: the electromagnetic force mediated by the massless photon, the strong force mediated by eight massless gluons, and the weak force mediated by the massive $W^{\pm}$ and Z. Those force carriers, summarized as gauge bosons, carry a spin of 1 and are defined as quantum excitations of the corresponding gauge field. The fact that the masses of the gauge bosons of weak interaction are measured to be non-zero, leads to the postulation of another boson, the scalar Higgs-Boson. All attempts to discover the Higgs-Boson have been futile until the aera of the LHC, whose two major collaborations ATLAS and CMS independently claimed a higgs-boson-compatible discovery [4, 5]. Matter (and antimatter) is represented by fermionic fields (spin $\frac{1}{2}$) and is divided into the group of leptons and the group of quarks. There are three electrically charged leptons (electron, muon and tau) and three corresponding neutral, very light particles observed (called electron neutrino, muon neutrino and tau neutrino). Three of the six observed quarks have an electrical charge of $+\frac{2}{3}$ (the so called up quark, charm quark and top quark), the other three have a charge of $-\frac{1}{3}$ (down quark, strange quark, bottom quark). Apart from their different electric charges and masses (see figure 1.1), quarks, unlike leptons, underlie the strong interaction.

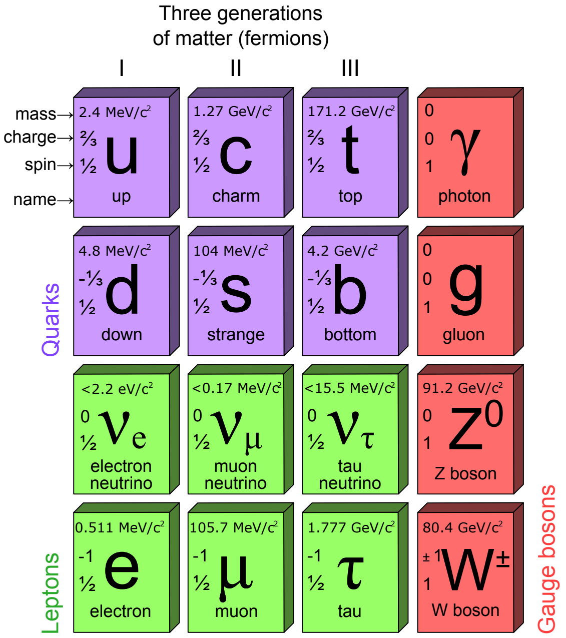

Figure 1.1.: Fermions and gauge bosons of the Standard Model [6]

---

[1] The gravitational force still holds out against quantization.

In the following subsections the most important theoretical components of the Standard Model are introduced using the Lagrange formalism.

The Lagrange density (Lagrangian) $\mathscr{L}(\phi_i, \partial\phi_i)$ is a function of the quantum fields ϕ_i and $\partial\phi_i$ from which, if known for a certain system, the dynamics can directly be derived via the Euler-Lagrange equations

$$\frac{\partial\mathscr{L}}{\partial\phi_i} = \partial_\mu \frac{\partial\mathscr{L}}{\partial(\partial_\mu\phi_i)} \tag{1.3}$$

The basis of the SM as a quantum field theory is the idea to postulate that certain local transformations leave the Lagrangian unchanged, which is called gauge invariance. This idea, called gauge principle, maintains that the considered field theory is renormalizable, i.e. being capable of making finite predictions after absorbing infinite terms into parameters.

1.1.1. Quantum Electrodynamics

A successful attempt to find an extension to the Schrödinger equation to describe relativistic quantum fields was made by Paul Dirac [7]. A free Dirac fermion can be described via the Dirac equation

$$(i\gamma^\mu\partial_\mu - m)\psi(x) = 0 \tag{1.4}$$

which can be derived from the Lagrangian

$$\mathscr{L}_0 = i\bar{\psi}(x)\gamma^\mu\partial_\mu\psi(x) - m\bar{\psi}(x)\psi(x). \tag{1.5}$$

Here, m is the mass of the fermion, ψ is its four-dimensional[2] spinor and $\gamma^{\mu=0,1,2,3}$ are the Dirac matrices. $\mathscr{L}_0$ is invariant under global $U(1)$ transformation

$$\psi(x) \to \psi(x)e^{iQ\theta}, \tag{1.6}$$

but not under local $U(1)$ transformation, where $\theta = \theta(x)$. To maintain phase invariance under local gauge transformations (i.e. to fulfil the gauge principle), a new spin-1 field $A_\mu(x)$ is introduced, which transforms as:

$$A_\mu(x) \to A_\mu(x) + \frac{1}{e}\partial_\mu\theta. \tag{1.7}$$

Now, the covariant derivative defined as

$$D_\mu\psi(x) = (\partial_\mu - ieQA_\mu(x))\psi(x) \tag{1.8}$$

replaces the partial derivative ∂_μ to receive the $U(1)$ gauge invariant Lagrangian:

$$\mathscr{L} = \mathscr{L}_0 + eQA_\mu(x)\bar{\psi}(x)\psi(x) \tag{1.9}$$

---

[2] one dimension for every spin configuration of the particle and the antiparticle

After adding a kinematic term

$$\mathscr{L}_{kin} = -\frac{1}{4}F_{\mu\nu}(x)F_{\mu\nu}(x), \tag{1.10}$$

where $F_{\mu\nu}(x) = \partial_\mu A_\nu(x) - \partial_\nu A_\mu(x)$, one yields the complete Lagrangian of quantum electrodynamics (QED):

$$\mathscr{L}_{QED} = i\bar{\psi}(x)\gamma^\mu\partial_\mu\psi(x) - m\bar{\psi}(x)\psi(x) + eQA_\mu(x)\bar{\psi}(x)\psi(x) - \frac{1}{4}F_{\mu\nu}(x)F\mu\nu(x), \tag{1.11}$$

in which e is associated with the coupling constant of the QED (elementary charge) and Q being the the charge of the fermion. The first term is interpreted as the kinetic energy of the fermion, the second one is its mass term, the third one describes the interaction between a charged particle and a photon and the fourth is the kinetic term of the photon.

1.1.2. Quantum Chromodynamics

As already mentioned, only quarks do interact via the strong interaction [8]. Quarks are observed to exist only in bound states consisting of either a quark-antiquark pair (meson) or three (anti-)quarks (baryon). To explain this and further observations a new quantum number is postulated: the colour charge. Each quark is either red, green or blue, and baryons and mesons are all colourless from the outside. This, together with an increase of the strong coupling for higher distances, is called the confinement hypothesis. The existence of three colours leads to 12-dimensional[3] spinors for the quark fields in the QCD. Demanding local $SU(3)$ gauge invariance of the free Lagrangian leads to eight independent gauge parameters and therefore the postulation of eight different strong force exchange particles, the gluons. The fact that the eight $SU(3)$ matrices do not commutate gives rise to two differences between the QED and the QCD. At first, the gauge field does interact with itself. Cubic and quartic gluon self-interactions are possible. The second difference is that the coupling α_s between all quarks and the gluons is the same, namely $\alpha_s(s = M_Z^2) = \frac{g_s^2}{4\pi} \approx 0.12$, where g_s is the strong coupling constant.

1.1.3. Electroweak Unification

The term electroweak unification [9, 10] describes the effort to create a gauge invariant Lagrangian, which satisfies the experimentally observed phenomena of electrodynamics and weak interaction. The latter are (among others) the parity violation for weak interactions (100 % for $W^\pm$, less for Z), the apparent non-existence of (anti-)neutrinos with right-handed chirality, the possible flavour-mixing involving quarks and charged currents (weak eigenstates are different from mass eigenstates), the absence of flavour changing neutral currents and the non-zero masses of three gauge bosons. The symmetry group has to take into account the appearance of left-handed doublets as well as the electromagnetic interaction. The simplest symmetry group to consider is therefore

$$SU(2)_L \times U(1)_Y, \tag{1.12}$$

---

[3] three from the colour times four of the QED spinors

where L stands for left-handed fields and Y is called the electroweak hypercharge and defines the couplings inside the $U(1)$ group, analogously (but not equal) to the electric charge Q inside the $U(1)_{QED}$. The corresponding quantum number to the $SU(2)_L$ is the weak isospin I, which is related to Y and Q via

$$\frac{Y}{2} = Q - I_3. \tag{1.13}$$

The quantum numbers of the weak interaction are summarized in table 1.1.

	Q	I	I_3	Y
ν_L	0	1/2	1/2	-1
e_L	-1	1/2	-1/2	-1
e_R	-1	0	0	-2
u_L	2/3	1/2	1/2	1/3
d_L	-1/3	1/2	-1/2	1/3
u_R	2/3	0	0	4/3
d_R	-1/3	0	0	-2/3

Table 1.1.: Quantum numbers of the electroweak theory: Q is the electric charge, I is the weak isospin and Y is the hypercharge. $u_{L/R}$ and $d_{L/R}$ refer to all up and down quarks, respectively. For antiparticles, the signs of the quantum numbers are inverted [3].

Since the $SU(2)_L$ has three generators and the $U(1)_Y$ one, four gauge fields result, two charged ($W^{1,2}$) and two neutral ones (W^3 and B). The electroweak covariant derivative reads

$$D^\mu = \partial^\mu + \sum_{i=1}^{3} ig\tau_i \cdot W_i^\mu + ig'\frac{Y}{2} \cdot B^\mu, \tag{1.14}$$

where τ_i stands for the three generators of the $SU(2)$, e.g. the Pauli matrices, and g and g' are the two coupling strengths corresponding to $SU(2)_L$ and $U(1)_Y$. In order to maintain the four gauge bosons $W^\pm$, Z and A with their observed properties,they can be identified as linear combinations of the newly introduced gauge fields:

$$W^\pm = \frac{1}{\sqrt{2}}(W^1 \pm iW^2) \tag{1.15}$$

and

$$A = \cos\theta_W \cdot B + \sin\theta_W \cdot W^3 \tag{1.16}$$

$$Z = -\sin\theta_W \cdot B + \cos\theta_W \cdot W^3. \tag{1.17}$$

Here, θ_W is a free mixing parameter and called Weinberg angle. It is related to the couplings via

$$\cos\theta_W = \frac{g}{\sqrt{g^2 + g'^2}} \tag{1.18}$$

and can be measured (as a direct result of the Higgs mechanism, see next subsection) via the boson masses

$$\cos\theta_W = \frac{m_W}{m_Z} \tag{1.19}$$

to $\theta_W \approx 28.74°$. As a direct consequence of the gauge symmetry of the electroweak Lagrangian, the couplings of quarks and leptons are universally the same for charged currents, while this is not the case for neutral currents. Another consequence is the existence of cubic and quartic self-interactions of the gauge bosons with always at least one pair of W bosons. While those two consequences hold against experimental result, the gauge symmetry also forbids mass terms for bosons (same reason as in the QED) and also for all fermions (fermionic masses would communicate the left- and right-handed fields which also leads to a breaking of the symmetry in the electroweak theory). Since this is not compatible with experimental results, a new mechanism must be introduced to break this symmetry.

1.1.4. Spontaneous Symmetry Breaking

In the 1960s several theoretical physicists [11, 12, 13, 14] provided a possible solution to the contradiction between massless gauge bosons in theory and massive ones in observation: The spontaneous symmetry breaking. This mechanism allows to maintain an invariant Lagrangian and therefore a renormalizable theory, despite of a non-symmetric vacuum. In order to achieve that, a $SU(2)_L$ doublet of complex scalar fields $\phi(x) = \begin{pmatrix} \phi^{(+)}(x) \\ \phi^{(0)}(x) \end{pmatrix}$ is introduced with the Lagrangian

$$\mathscr{L}_S = \partial^\dagger_\mu \partial^\mu \phi - V(\phi), \tag{1.20}$$

where $V(\phi)$ is a potential of the form

$$V(\phi) = \mu^2 \phi^\dagger \phi + h(\phi^\dagger \phi)^2, \qquad \mu^2 < 0, \quad h > 0. \tag{1.21}$$

$\mathscr{L}_S$ is invariant under global $U(1)$ transformations. The potential provides a continuous set of degenerated vacua with the modulus of the vacuum expectation value of the neutral field being $|\langle 0|\phi^{(0)}|0\rangle| = \sqrt{\frac{-\mu^2}{2h}}$, see figure 1.2 for an illustration of the singlet case $\phi(x) = \phi_1 + i\phi_2$.

When a particular minimum, i.e. a vacuum state, with a certain phase θ would be chosen in the symmetric potential, the vacuum would be non-symmetric, or in other words, spontaneously broken. After replacing the scalar field's derivative in 1.20 with the covariant derivative, which contains the electroweak gauge fields, the Lagrangian ends up including mass terms for the $W^\pm$ and Z. In doing so, three degrees of freedom corresponding to three (unphysical) massless Goldstone bosons, which arose from introducing $\phi(x)$, can be absorbed by the additional longitudinal spin polarization of the three now massive gauge bosons. One of the four real scalar fields remains and can be associated with the massive Higgs boson, which is the last Standard Model particle to be detected. In July 2012 ATLAS and CMS claimed independently the discovery of a new massive, Higgs-like boson with spin different from 1 and mass of around 125 GeV. Further data has yet to be analysed to be certain about the new particle being the Higgs boson and to measure its properties.

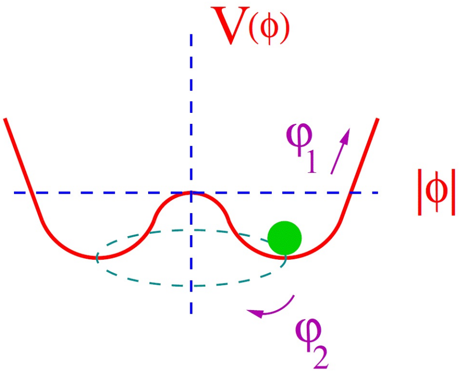

Figure 1.2.: The shape of the scalar potential. The infinite set of degenerated vacua lies on the dashed circle. While a field excitation ϕ_1 would be massive, an excitation ϕ_2 would connect the different states of vacua, would therefore be massless and can be interpreted as a Goldstone particle [2]

.

If a Yukawa-type coupling between the scalar field and the fermions is added to the electroweak Lagrangian, also fermion mass terms are generated by the spontaneous symmetry breaking, which do not spoil the gauge invariance any more.

1.1.5. Deficits of the Standard Model

Whereas the Standard Model of particle physics is one of the best tested models in physics so far, with the Higgs boson as the last piece of the puzzle possil found, still some shortcomings and open questions remain.

- The discrepancy between observed rotation curves of spiral galaxies and the expected ones [15] as well as measurements using gravity lensing [16] like the study of the Bullet Cluster lead to the hypothesis of an unknown type of subatomic particle representing a large part of the mass in the known universe, called dark matter. Since dark matter for now has only been detected indirectly via gravitation, not much is known about its nature. A favoured ansatz for its origin is the theory of supersymmetry, which predicts a global symmetry between bosons and fermions and postulates a dark matter candidate, an only weakly (and gravitationally) interacting, stable neutralino.

- Supersymmetry could also explain other open questions like the *hierarchy problem* that says that, if the Higgs boson mass is of the order of 100 GeV, its bare mass parameter must cancel out the bosonic loop corrections and therefore be accurate over about 30 orders of magnitude, which is unnatural. Also, the wide mass range of Standard Model particles over at least 11 orders of magnitude has no foundations in the theory. Further substructure could be an explanation.

- Supersymmetry would also provide a mechanism to unify the three fundamental forces of particle physics at one very high energy, therefore it would lead to a so called *grand unified theory.* In the Standard Model the three forces approach each other with increasing energy, but do not all meet in one point.

- *Neutrino oscillation* [17] describes the observed flavour transformation of one neutrino to another, e.g. an electron neutrino to a tau neutrino. This effect can be explained by introducing mass differences of the neutrinos and therefore masses to at least two neutrino flavours. But neutrino masses would lead to the existence of right-handed neutrinos, which are not part of the Standard Model.
- In our known universe an extreme *asymmetry* between the occurrence of *baryonic matter and antimatter* is observed. The Sakharov conditions postulate (besides interactions out of the thermal equilibrium) a CP violation and a violation of the baryonic number [18]. While the last one is not observed, a CP violation is observed and part of the Standard Model, but the measured effect is much too low to explain the matter-antimatter asymmetry.
- The *origin of the parity violation* in nature is not understood. Its addition to the Standard Model looks artificial. A possible symmetrization is shown in the following section.

1.2. Possible Extensions of the Standard Model

In this section possible extensions to the Standard Model, which are searched for in this thesis, are briefly theoretically motivated. The main part deals with the search for new heavy charged gauge bosons, but also possible reinterpretations as four-fermion contact interactions and universal extra dimensions are introduced.

1.2.1. Left-right Symmetric Extension to the Standard Model

In [19] a left-right symmetric extension to the Standard Model is discussed with the new symmetry group $SU(2)_L \times SU(2)_R \times U(1)_{\tilde{Y}}$. Changes in the strong sector are not necessary for now and are left unconsidered. In order to reflect the observed parity violation, the new symmetry group must be broken (at least for lower energies) to the known $SU(2)_L \times U(1)_Y$, which itself is still broken to the $U(1)_{QED}$. The $SU(2)_R$ gives rise to right-handed doublets, which replace the right-handed singlets of the Standard Model [20]

$$u_R, d_R \rightarrow \begin{pmatrix} u \\ d \end{pmatrix}_R \quad \text{and} \quad \nu_R, \ell_R \rightarrow \begin{pmatrix} \nu \\ \ell \end{pmatrix}_R, \tag{1.22}$$

and therefore especially gives rise to the existence of a right-handed neutrino. Note that the left- and right-handed fermions still have to have the same electric charge and the $U(1)_{\tilde{Y}}$ works on both of them, we obtain the relation (Gell-Mann-Nishijima formula, see 1.13 for SM case)

$$\frac{\tilde{Y}}{2} = Q - I_{3L} - I_{3R}, \tag{1.23}$$

where $I_{3L/R}$ is the third component of the isospin for the left-/right-handed doublet. Further, it follows that

$$\tilde{Y} = B - L, \tag{1.24}$$

where B is the baryon number and L the overall leptonic number and therefore $\tilde{Y}$ has a direct physical interpretation. This results in $\tilde{Y} = -1$ for leptons and $\tilde{Y} = 1/3$ for quarks. The gauge invariant covariant derivatives (see 1.14) now read for the left- and the right-handed doublets

$$D_L^\mu = \partial + ig_L\tau_i \cdot W_{i,L}^\mu + ig'\frac{\tilde{Y}}{2} \cdot B^\mu \tag{1.25}$$

$$D_R^\mu = \partial + ig_R\tau_i \cdot W_{i,R}^\mu + ig'\frac{\tilde{Y}}{2} \cdot B^\mu. \tag{1.26}$$

In order to give masses to the fermions, Yukawa terms $\psi_L\phi\psi_R$ are needed, which leads to new scalar fields, arranged in a 2x2 matrix.

$$\begin{pmatrix} \phi_1^{(0)} & \phi_1^{(+)} \\ \phi_2^{(-)} & \phi_2^{(0)} \end{pmatrix}. \tag{1.27}$$

Unlike in the Standard Model, the field ϕ cannot be used for symmetry breaking, but other scalar fields have to be added to the theory. While several approaches are possible, the easiest way (so called Minimal Left-Right Symmetric Model [21]) is to add two scalar triplets

$$\Delta_{L/R} = \begin{pmatrix} \delta_{L/R}^{(+)}/\sqrt{2} & \delta_{L/R}^{(++)} \\ \delta_{L/R}^{(0)} & -\delta_{L/R}^{(+)}/\sqrt{2} \end{pmatrix} \tag{1.28}$$

containing a neutral, a singly and a doubly charged scalar field.

Requiring the photon to remain massless, the vacuum expectation values (zero for the charged scalar fields, since electric charge is a conserved quantity) are

$$\phi_0 = \begin{pmatrix} v_1 & 0 \\ 0 & v_2 \end{pmatrix} \quad \text{and} \quad \Delta_{L/R,0} = \begin{pmatrix} 0 & 0 \\ w_{L/R} & 0 \end{pmatrix}. \tag{1.29}$$

The mass eigenstates $W_{1,2}$ are yielded from a mixing of the chiral eigenstates $W_{L,R}$:

$$\begin{pmatrix} W_1 \\ W_2 \end{pmatrix} = \begin{pmatrix} \cos\zeta & -\sin\zeta e^{i\lambda} \\ \sin\zeta e^{-i\lambda} & \cos\zeta \end{pmatrix} \cdot \begin{pmatrix} W_L \\ W_R \end{pmatrix}, \tag{1.30}$$

where $\lambda = \lambda(v_1, v_2)$ and $\zeta \propto m_1^2/m_2^2$. Assuming $|w_L|^2 << |w_R|^2$, one obtains $m_1^2 \approx m_W^2$ and $m_2^2 \approx m_{W'} \approx \frac{g^2}{2}|w_R|^2$. Since left-right symmetry has not been observed, its scale $|w_R|$ and therefore m_W' has to be large. Several model dependent constraints exist, e.g. assuming the same quark mixing matrix for right-handed and left-handed quarks [22]), one obtains from the mass difference of K_L and K_S $m_{W'} > 1.6$ TeV. The large mass difference leads to $\zeta \approx 0$ and hence a suppressed mixing, i.e. $W_1 \approx W_L$ and $W_L \approx W_R = W'$.

1.2.2. The Reference Model

Additional charged (and neutral) gauge bosons are predicted by many other theoretical extensions of the Standard Model, such as Little Higgs Models, Extra Dimensions and higher unification groups ($SU(5), E_6, SO(10)$). The Reference Model [23] by Altarelli et al. provides a generic theory, which produces similar predictions as the different other theories with a more general approach. In this model the two additional charged gauge bosons $W'^{\pm}$ and the neutral Z' are predicted to behave like simple heavier copies of SM gauge bosons. $W'^{\pm}$ and Z' are assumed to have the same couplings to standard-model fermions and bosons as the W and Z, which now allows the W' to decay on-shell to t and b and also the bosonic decay to WZ. The latter is calculated to be dominant, because of a width

$$\Gamma(W' \to WZ) \propto \frac{m_{W'}^5}{m_Z^2 \cdot m_W^2}. \tag{1.31}$$

The full calculation leads to widths bigger than the mass for $m_W' > 500$ GeV. In order to suppress this large width, a suppression factor can be introduced by hand. A factor

$$\zeta = (\frac{m_W}{m_{W'}})^2 \tag{1.32}$$

would occur, if the left-right symmetric model is considered. The partial width into fermions is the same as for the W, scaled with their mass ratio

$$\Gamma(W' \to f_a \bar{f}_b) = \frac{m_{W'}}{m_W} \Gamma(W \to f_a \bar{f}_b). \tag{1.33}$$

1.2.3. The Sequential Standard Model

In this thesis the search for a heavy, charged gauge boson is based on the Sequential Standard Model (SSM) [24], which is implemented in the event generator Pythia 6. It is mainly the same as the Reference Model 1.2.2, but with two important restrictions: First, the W' is strictly required to couple only to right-handed particles. Therefore, interference between the Standard Model W and the W' does not occur. In this analysis the search is only applied in the leptonic decay channels (μ, ν), which by implication involves right-handed neutrinos. Since the SSM only acts as a benchmark model in this search, constraints on right-handed neutrinos are not taken into account for exclusion limits later on. The second change with respect to the Reference Model is that the W' does not couple to W and Z bosons. Thus the decay channel to WZ, which is the dominant one in the Reference Model, is not allowed any more. The total width is then given by [25, 26]

$$\Gamma_{W'} = m_{W'} \cdot \frac{g^2}{96\pi}(18 + 3F(\frac{m_t}{m_{W'}}, \frac{m_b}{m_{W'}})) \approx \frac{m_{W'}}{m_W} \cdot \frac{11}{9} \cdot \Gamma_W, \tag{1.34}$$

$$F(x,y) = (2 - x^2 - y^2 - (x^2 - y^2)^2)\sqrt{(1-(x+y)^2)(1-(x-y)^2)}. \tag{1.35}$$

The value of Γ_W is approximately 2.1 GeV [27], which for example leads to $\Gamma_{W'}(m_{W'} = 2.5\text{ TeV}) \approx 80$ GeV. Note, that F(0,0) = 2, i.e. a high W' mass justifies the approximation in equation 1.34 between the widths of the W and W'. The total width of the W'

increases linearly with its mass and is enhanced by 11/9 due to the now allowed decay into t and b quark. The leptonic branching ratios are then ≈ 8 %, while being $\approx 11\%$ for the SM W. As for the SM W, in the rest frame of the W', the differential cross section $\frac{d\sigma}{d\cos\theta^*}$ (averaged over $W^\pm$) is not uniformly distributed in $\cos(\theta^*)$, as an isotropic decay would induce, but it follows

$$\frac{1}{\sigma}\frac{d\sigma}{d\cos\theta^*} = \frac{3}{8}(1+\cos^2(\theta^*)) \tag{1.36}$$

Here, $\cos\theta^*$ is the angle between the incoming quark and the outcoming fermion. This dependency can be interpreted as induced by conservation of the angular momentum of the quarks in the initial state, which is typical for spin-1 particle exchange via s-channel.

1.2.4. Split Universal Extra Dimensions

As mentioned before, there is a variety of models predicting a W'. One possibility that will be discussed briefly in the following is the prediction of Universal Extra Dimensions (UED). Those models predict a fifth, compact spatial dimension. The known SM particles are then the lowest of many states with excitations in the new dimension (KK-particles). Instead of the regular UED models, the Split UED [28] allows KK-particles to be produced not only in pairs, but also alone (together with SM particles). This is achieved by introducing the so called bulk mass parameter μ. The model then gives rise to excitations of the SM W, called W_n, which partly have the same properties as the W' of the SSM, which allows to apply the results of the SSM search on this model. The parameter of the Split UED are μ and the radius R of the additional dimension. The masses of the KK-W excitations are given by

$$m_{W_n}^2 = m_W^2 + (\frac{n}{R})^2. \tag{1.37}$$

Thus, W_0 denotes the SM W. The coupling g_n of the n-th KK excitation to SM particles is

$$g_n = g^{SM}\mathcal{F}_n(\pi\mu R), \quad \text{with} \tag{1.38}$$

$$\mathcal{F}_n(x) = \begin{cases} 0 & \text{, if } n = 2m \\ \frac{x^2(-1+(-1)^m e^{2x})(\coth x - 1)}{\sqrt{2(1+\delta_{m0})(x^2+m^2\pi^2/4)}} & \text{, if } n = 2m+1 \end{cases} \tag{1.39}$$

Since odd modes do not couple to SM particles because of Kaluza-Klein parity conservation and for modes higher than $n = 3$ the LHC has not sufficient sensitivity at current center-of-mass energies, only the mode $n = 2$ is investigated. The translation of SSM W' mass limits to the split UED model is done in [29].

1.2.5. Contact Interactions to Muon and Neutrino

A further reinterpretation of the W' search is a four-fermion contact interaction. The basic assumption, which is motivated by the observation of mass hierarchies in the fermion sector, is that quarks and leptons are composite objects of fundamental constituents called preons [30]. But also new, very heavy exchange particles could lead to contact interactions. Its first introduction and successful application on the muon decay, which later was explained with W boson exchange, was done by Enrico Fermi. At energies much lower than the binding energy of the preons (or the exchange particle mass), typically called Λ, the quark and lepton compositeness would manifest itself as four-fermion contact interaction. Note that this theory is only an approximate description without knowing the exact structure of the underlying physics. The theory is not renormalizable, because its cross section rises with increasing center-of-mass energy and violates the unitarity bound eventually. There are plenty of possible contact interaction models (e.g. the Left-Left-Isoscalar Model [31]), differing in which particles are composite and in the chiral nature of the interaction. The contact interaction between two quarks, a neutrino and a lepton is described in the Helicity-non-conserving model [31], [32] (HNCM), which is investigated in this thesis. The Lagrangian is

$$\mathcal{L}_{HNC} = -\frac{4\pi}{\Lambda^2}\varepsilon_{ij}\overline{Q}_{Lia}u_{Ra}\overline{L}_{Ljb}\ell_{Rb} + h.c. \tag{1.40}$$

where i, j = 1, 2 are the indices for the electroweak quark and lepton doublets Q and L while a and b refer to the generations and $\varepsilon_{12} = \varepsilon_{21} = 1$. This Lagrangian allows either two charged leptons, or one charged lepton and one neutrino in the final state. For this reinterpretation only the latter combination of lepton and MET is interesting (for an example, see figure 1.3) with the corresponding cross section

$$\frac{d\hat{\sigma}(q\bar{q}' \xrightarrow{\text{CI}} \mu\nu)}{d\cos(\theta^*)} = \pi\frac{\hat{s}}{12\Lambda^4} \tag{1.41}$$

being proportional to the square of the center-of-mass energy and therefore yielding an excess of events at high transverse masses. There is no interference between the Helicity-non-conserving model and the standard model W because of their different chiral structure. While the W only couples to left-handed particles and right-handed antiparticles (in terms of helicity), the contact interaction in this model always involves a right-handed fermion (or a left-handed antifermion). However, the structure of the Lagrangian ensures that no right-handed neutrinos (left-handed antineutrinos) do occur. An example of a possible HNC interaction is shown in figure 1.3, where a right-handed quark and a right-handed anti-quark are in the initial state and a left-handed muon and a left-handed neutrino in the final state. The model is called helicity-non-conserving because two right-handed (anti-)particles convert into two left-handed particles or vice versa. Note that the conservation of angular momentum is not violated at any point in this model. While being not explicitly motivated by a specific underlying compositeness theory [33], the HNCM (similar to the SSM for the W' search) is easy to handle in a search because of the absence of interference with the SM W and can be used as a reference point for other effective theories describing compositeness models.
Apart from compositeness, the HNC model is an effective description of an exchange of a new complex scalar particle ϕ as described by the Lagrangian [34]

$$\mathcal{L} = \lambda_1\phi^i\overline{Q}_{Li}u_R + \lambda_2\phi_k^\dagger\varepsilon^{kj}\overline{L}_j l_R + h.c., \tag{1.42}$$

with the coupling constants $\lambda_{1/2}$. The relation between the scale Λ and the mass m_ϕ of the scalar and its couplings would be

$$\frac{4\pi}{\Lambda^2} \propto \frac{\lambda_1 \lambda_2}{m_\phi^2}. \tag{1.43}$$

Additional heavy scalars are postulated by theories containing 2-Higgs-Doublets, especially supersymmetric theories like the MSSM[4].

The cross section decreases with an increasing energy scale Λ, because the contact interaction coupling is suppressed by Λ^{-2}.

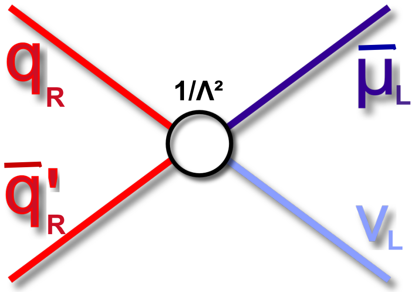

Figure 1.3.: A possible contact interaction with muonic final state, as considered in this analysis. Note that the subscripts L and R denote the state of helicity.

There is no limit in the muon channel on Λ corresponding to the Helicity-non-conserving model, yet. In the electron channel CDF has set a limit on the energy scale of Λ= 2.81 TeV [35].

1.3. Parton Distribution Functions and Cross Sections at Hadron Colliders

The cross section of a considered process has to be known with a sufficient precision to make reliable predictions about its event rate. However, since protons are composite objects consisting of hadrons (quarks and gluons), one has to have information about the statistical distributions of the partons' momenta to evaluate production cross sections. These distributions cannot be calculated with pertubative QCD because of the divergence of the strong coupling α_s, hence it has to be determined by measurements.

A proton consists of the three valence quarks (up, up and down), gluons and a large amount of sea quarks (up, down, strange, charm, bottom and their anti-partners). The

---

[4] Minimal Supersymmetric Standard Model

momentum P of a proton can be written as the sum over all parton momenta p_i, each being a certain fraction x_i of P satisfying

$$\sum_i x_i = 1. \tag{1.44}$$

Thus, the energy of the center-of mass system of two hard scattering protons $\sqrt{\hat{s}}$ can be expressed as

$$\sqrt{\hat{s}} = \sqrt{x_1 x_2 s}, \tag{1.45}$$

with $\sqrt{s}$ being the center-of-mass energy of the two protons. The parton density functions $f_i(Q^2, x)$ describe the probability to have a parton[5] of type i with momentum fraction x and a momentum transfer Q between the two colliding quarks. The $f_i(Q^2, x)$ are normalized such that the integral over x returns the total number of the parton type i in the proton and hence, e.g.

$$\int_0^1 [f_u(Q^2, x) - f_{\bar{u}}(Q^2, x)]dx = 2 \quad \text{and} \quad \int_0^1 [f_s(Q^2, x) - f_{\bar{s}}(Q^2, x)]dx = 0. \tag{1.46}$$

At hadron colliders, the cross section σ depends largely on the PDF set taken as a basis for the calculation and can be determined with the following formula [36]

$$\sigma = \sum_{i,j} \int_0^1 \int_0^1 f_i(x_1, Q^2) f_j(x_2, Q^2) \cdot \hat{\sigma}_{ij}(Q^2) dx_1 dx_2, \tag{1.47}$$

where the sums go over all partons, $\hat{\sigma_{ij}}$ is the cross section of the subatomic process and $Q^2 = x_1 x_2 s$ is the momentum transfer between the interacting partons.
Since the PDFs cannot be derived by theory alone, they are extrapolated from measurements. Therefore, cross sections at hadron colliders are afflicted with a significant uncertainty originating from the measurements and the theory itself. These uncertainties are estimated and discussed in section 4.4.

1.4. The Jacobian Peak and the Transverse Mass

In this section a short explanation of the *Jacobian Peak* in the p_T and transverse mass spectrum of a W' decay is given as a theoretical foundation for section 4.2.2, adapted from [36].

1.4.1. The Jacobian Peak

In the center-of-mass system of a two-body decay (like the W' decay) the momenta and especially the transverse momenta are democratically shared. Therefore, every daughter

---

[5] Quarks and anti-quarks of the same flavour do not share the same PDF, so $f_i(x)$ is different for e.g. d and $\bar{d}$

particle[6] gains the momentum $p = \sqrt{\hat{s}}/2$, which leads to

$$p_T^2 = \frac{1}{4}\hat{s}\sin^2(\theta^*). \tag{1.48}$$

with $\theta^* = \pi - \theta_{\text{CMS}}$ being the angle between CMS z axis and one outgoing particle. p_T is called the transverse momentum and is invariant under Lorentz boosts in z direction. Equations 1.48 and 1.36 lead to a differential cross section

$$\frac{1}{\sigma}\frac{d\sigma}{dp_T^2} = \frac{3}{2\hat{s}}(1 - 2p_T^2/\hat{s})(1 - (4p_T^2/\hat{s})^2)^{-\frac{1}{2}} \tag{1.49}$$

The last term comes from the Jacobian determinant $\frac{dcos(\theta^*)}{dp_T^2}$ and leads to a positive pole at $p_T = \sqrt{\hat{s}}/2 \approx M_{W'}/2$, which causes the *Jacobian Peak*. In reality this divergence is smeared out due to the non-zero width of the W' leading to a p_T distribution as displayed in figure 1.4.

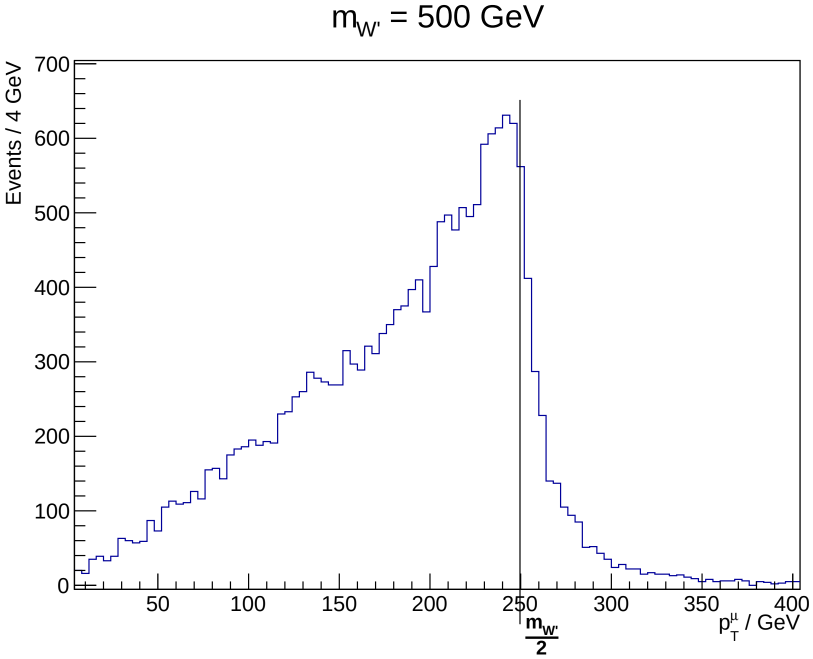

Figure 1.4.: The transverse momentum distribution at generator level of a muon coming from a W' decay with mass $M_{W'}$ =500 GeV, showing a Jacobian peak at $M_{W'}/2$.

---

[6] This is only exactly true for massless particles in the final state, but a reasonable approach, if $\sqrt{\hat{s}}$ is much greater than the masses of the particles in the final state as it is generally the case in this analysis.

1.4.2. The Transverse Mass

The transverse mass M_T of two particles (in this example, muon and neutrino) is defined as

$$M_T = \sqrt{2 \cdot p_T^{\mu} p_T^{\nu} (1 - \cos(\Delta\phi_{\mu,\nu}))}, \tag{1.50}$$

where $\Delta\phi_{\mu,\nu}$ is the angle between the transverse momenta of muon and neutrino, p_T^{μ} and p_T^{ν}. M_T is used as observable rather than M_{inv}, because the neutrino can only be measured indirectly by reconstructing the missing transverse energy in an event, see section 4.2.2 for further discussions. Therefore, $\mathrm{M_T}$ can be seen as projection of the invariant mass M_{inv} into the transverse plane. It fulfils $M_T \leq M_{\text{inv}}$, with equality given, if p^{μ} has no component parallel to the z axis. Due to relation 1.49, a Jacobian peak can also be observed in the transverse mass distribution at $M_T = M_{W'}$.

2. Experimental Setup

In this chapter the experimental setup is described, consisting of the Large Hadron Collider (LHC) and the Compact Muon Solenoid (CMS) as a detector.

2.1. The LHC

The particle accelerators that reach the highest energies have a circular structure, in which particles are held on a closed path by a time-dependent (synchronized) magnetic field. Those ‘synchrotrons’ allow for very high beam energies, because the particles can be accelerated again in every revolution. The limiting parameter is the occurring synchrotron radiation, which depends on the fourth power of the particle mass and thus heavy particles are often favoured over light ones. Unlike fixed-target experiments, circular colliders are able to recycle the particle beam and achieve higher center-of-mass energies. The number of collision events per time is a function of the cross section σ of the process and of the luminosity $\mathscr{L}$,

$$\dot{N} = \sigma \cdot \mathscr{L}. \tag{2.1}$$

At LHC-like colliders[1] the luminosity is

$$\mathscr{L} = \frac{N_b^2 n_b f_{\mathrm{rev}} \gamma_r}{4\pi \epsilon_n \beta^*} F, \tag{2.2}$$

where N_b is the number of particles per bunch, n_b is the number of bunches per beam, f_{rev} is the revolving frequency, γ_r the relativistic gamma factor, ϵ_n the normalized transverse beam emittance[2], β^* the beta function[3] at collision point and F a geometrical correction. The Large Hadron Collider (LHC) [38] is the biggest particle accelerator and collider in the world and achieves the highest center-of-mass energy. It is located near Geneva in Switzerland in a tunnel, 45 to 170 m under the ground and 27 km long. The LHC is run with proton-proton, lead-proton or lead-lead beams. The proton-proton runs, from which the data is taken in this analysis, were operated at a center-of-mass energy of $\sqrt{s} = 8$ TeV during 2012 data taking. The maximum instantaneous luminosity was (as of 19th of September 2012 [39]) 7.5 Hz/nb with a bunch spacing of 50 ns. The magnetic field used to bend the particle beams in the arcs reaches 8.3 T at design beam energy of

---

[1] I.e., with the same number of particles N_b in every bunch and a gaussian particle distribution along the beam.

[2] ϵ_n is a measurement of the parallelism of a beam and has the unit of length [37].

[3] β^* is the value of the amplitude function β at the interaction point. β depends on the magnet configuration and is a measurement of the size of the cross section of the beam. β^* has units of length [37].

7 TeV. The protons run through two different rings with opposite magnetic dipole rings. Four interaction points exist where the two beams are crossed. At these points the four big experiments are placed: CMS, ATLAS, ALICE and LHCb, see figure 2.1. CMS [40] and ATLAS [41] are high-luminosity multi-purpose experiments, LHCb [42] is designed to investigate b-quark physics and ALICE [43] is built to study heavy ion events. There are four different preaccelerators (one linear and three circular accelerators), which bring the protons to an energy of 450 GeV at which they get injected into the LHC. They are then captured, accelerated, stored and collimated using a 400 MHz superconducting cavity system.

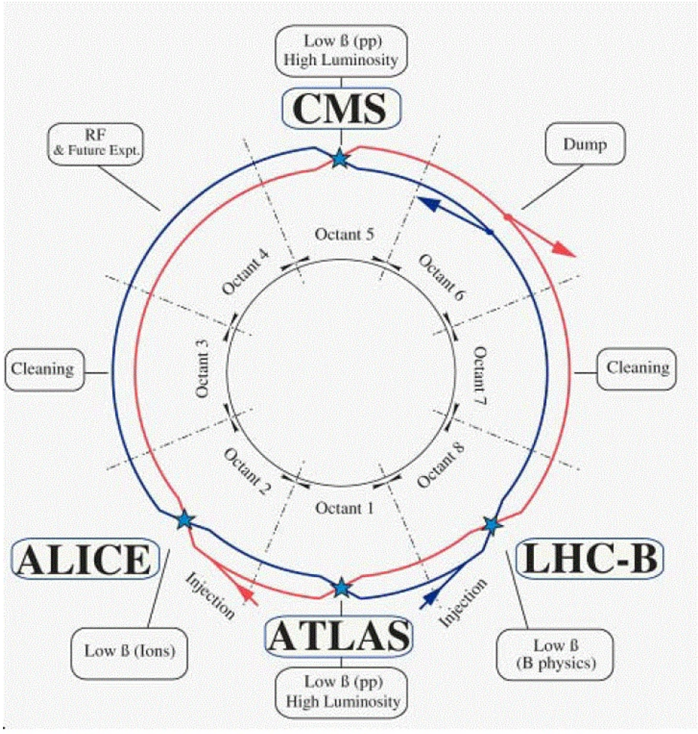

Figure 2.1.: Schematic overview of the LHC with its four interaction points [38]

2.2. The CMS Experiment

The CMS (Compact Muon Solenoid) detector is one of two multi-purpose detectors at the LHC. Its following description with all stated values and figures is based on [40], if not explicitly stated otherwise.

The CMS detector has a cylindrical shape, weighs roughly 14000 t, but measures only 21.6 m in length and 14.6 m in diameter, and is thus called compact. The last part of its name originates from the superconducting, helium-cooled solenoid, which is responsible for the large magnetic field of 3.8 T that is needed to bend trajectories of charged particles to measure their momenta.

The magnetic field is returned by a 10000 t iron yoke to keep it strong in the outer parts of the detector. The detector is geometrically divided into the central region ($|\eta| < 1.2$)[4], where the detector parts are concentrically surrounding the beam pipe and the forward region $|\eta| > 1.2$, where the detectors are oriented orthogonally to the beam pipe as shown in figure 2.2.

Its components are described briefly in the next paragraphs.

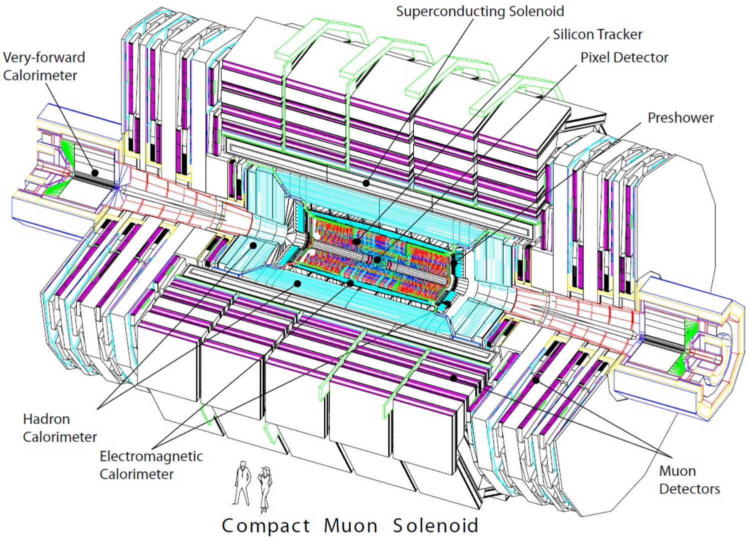

Figure 2.2.: View of the CMS detector with its different subdetector systems [40].

2.2.1. The Tracker System

The CMS tracker is the innermost detector part. It is hit by ≈ 1000 particles per bunch crossing and has to measure charged particle tracks with a momentum greater than 1 GeV and for $|\eta|$ up to 2.5, locate secondary vertices very precisely. It further has to be robust to the enormous radiative exposure and has to have a high granularity and fast readout to be able to resolve the different events in time. Its diameter is 2.5 m and its length 5.8 m. It consists of two kinds of silicon detectors, the pixel detector and the strip detector.

The Pixel Detector

The innermost part of the tracking system is the pixel vertex detector. It provides a good resolution of impact parameters, which is important for dealing with pile-up events and reconstructing secondary vertices and contributes precise tracking points in

---

[4] η denotes the pseudorapidity (cf CMS coordinate system in the introduction).

r-ϕ and z. A single pixel cell has the size of 100 x 150 μm^2 summing up to about 66 million single pixels, distributed over three layers with radii between 4 cm and 10 cm in the central region and two disks in the forward region. Due to charge sharing, a spatial resolution of about 15 μm is reached.

The Strip Tracker

The strip tracker is mainly used to determine the curvature of charged particles to measure their momentum. It follows the pixel detector and reaches from 20 up to 116 cm in the radial direction. The material budget corresponds to 0.4 to 1.8 radiation lengths, causing charged particles to emit bremsstrahlung and photons to convert to electron pairs, which has to be taken into account when reconstructing the track.
It consists (see figure 2.3) of the tracker inner barrel (TIB) and the tracker inner disks (TID) in the inner region, which is surrounded by the tracker outer barrel (TOB) in the central region and by the tracker endcaps (TEC) in the region of $0.9 < |\eta| < 2.5$.

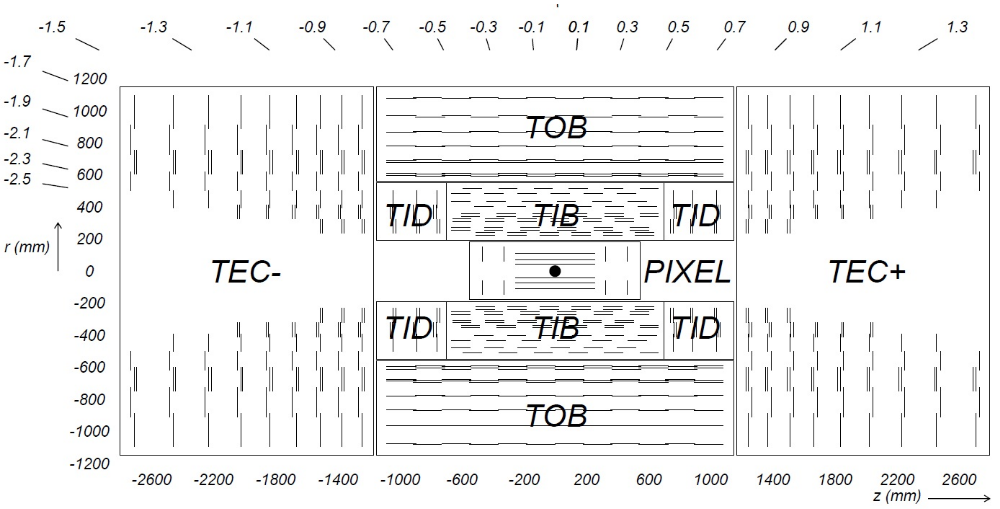

Figure 2.3.: Schematic cross section through the CMS tracker. Each line represents a tracker module [40].

While the TIB has four layers and provides a spatial resolution of 20-40 μm, the TOB has six layers and provides a resolution of 40-50 μm. The slightly worse resolution with respect to the TIB is due to the fact that the layers are more separated in the TOB. All four TID consist of three disks with similar resolution as the TIB. Tracks of particles with energies of 100 GeV are measured with ≈1-2 % uncertainty on their momenta.

2.2.2. The Calorimeters

In this subsection the two calorimeters used at CMS are introduced, namely the Electromagnetic Calorimeter (ECal) and the Hadronic Calorimeter (HCal), which are both in the inside of the solenoid.

The Electromagnetic Calorimeter

The ECal is used to measure the energies of electrons and photons and also of the electromagnetic part of jets. It is made of more than 70000 tungstate ($PbWO_4$) crystals, each 230 mm long, that act as absorber and scintillator. The barrel ECal covers a region up to a pseudorapidity of 1.479 and the endcap part covers $1.179 < |\eta| < 3.0$ with roughly 7000 crystals in each endcap that have slightly different geometry than in the barrel.

Since the crystals are scintillators, they emit light, if a particle traverses them, which can afterwards be detected by photodetectors. Due to different magnetic field conditions in barrel and endcap, two kinds of photodetectors are used. In the barrel avalanche photodiodes are chosen. Because of the high magnetic field, vacuum phototriodes are used in the endcaps. Between $1.653 < |\eta| < 2.6$, a sampling calorimeter is installed as a preshower detector. It consists of lead radiators initiating electron/photon induced showers and silicon strip detectors to measure their energy and the transverse shower profile. Its aim is to distinguish between primary and secondary photons, with the latter coming out of neutral pion decays. It also helps to identify electrons and determine their position.

The Hadronic Calorimeter

The Hadronic Calorimeter (HCal) has the purpose to detect hadronic jets and indirectly measure the momentum transverse to the beam pipe of neutrinos or other (possibly not yet known) particles that do not interact with the detector via missing transverse energy. In figure 2.4 the four parts of the HCal are shown: The hadron barrel (HB), endcap (HE), outer (HO) and forward (HF) calorimeters. The HB covers a region up to $|\eta| < 1.3$.

The HO is a thin layer of scintillating material added in the barrel to make sure a sufficient sample depth is reached. It uses the solenoid as absorber and therefore consists of plastic scintillators only.

To cover the region $1.3 < |\eta| < 3.0$ the HE is installed inside the solenoid. It uses the same detector and absorber materials as the HB, but in a longitudinally segmented placement. The HF is able to reach $2.9 < |\eta| < 5.2$ to allow a precise determination of the very forward jets and missing transverse energy. To account for the higher radiation different materials are chosen in the HF. The 5 mm thick steel plates act as an absorber while quartz fibres are used as active material and photomultipliers detect the emitted cherenkov light generated by traversing particles.

2.2.3. The Muon System

Because of the relative ease and low background occurrence the muon detection and measurement is an important tool to detect signatures of new physics, such as the higgs

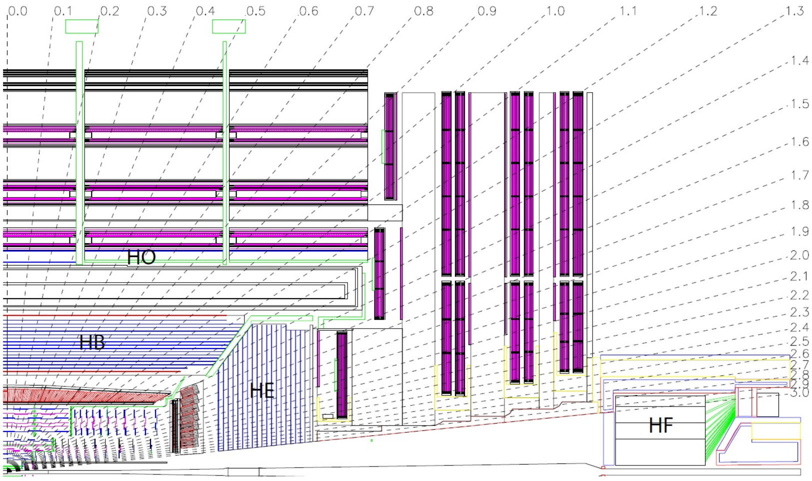

Figure 2.4.: Longitudinal view of the CMS HCal system consisting of the hadron barrel (HB), endcap (HE), outer (HO), and forward (HF) calorimeters [40].

boson decay into four muons via $ZZ^\star$ or the processes that are searched for in this thesis. Therefore, a dedicated detector system for muons is not only justified, but, as the name C$\underline{\text{M}}$S indicates, high in priority. Due to the fact that muons are interacting only slightly with the inner CMS components and have a relatively long lifetime, the muon system is the most distant subdetector being located outside the solenoid and installed between the flux return yokes. The muon system covers pseudorapidities up to $|\eta| < 2.4$, which is possible by using two different types of detectors (see in figure 2.5), namely drift tubes (DT) and cathode strip chambers (CSC), to account for strong physical disparities in the barrel and endcap regimes and an additional type, resistive plate chambers (RPC), for good time resolution and triggering purposes. After combining the measurements of the muon system and the tracker information, a resolution for highly energetic muons with a transverse momentum of ≈ 1 TeV of typically 5-10 % is achieved.

The three detector types of the muon system are described in the following.

The Drift Tubes

In the barrel region ($|\eta| < 1.2$) the magnetic field is homogeneous in good approximation and relatively low (<2 T) outside the solenoid. Also, the particle flux is less than in the endcaps. Those are reasons for the choice to use drift tubes as muon detectors in the barrel. The iron return yoke together with the drift tubes is mounted on five wheels, with the beam pipe in their center. The drift tubes are arranged in four concentric cylinders, called stations, surrounding the beam pipe. A number of only two stations, one inside and one outside the return yoke, would have been insufficient for reliable muon tracking and momentum measurement, so two additional stations are embedded in the yoke. Each station consists of 12 muon drift tubes per wheel, which are separated in ϕ-direction. The supports of the iron yoke, which have to be between the chambers, are causing 12 dead zones in the ϕ direction, although they do not overlap. In

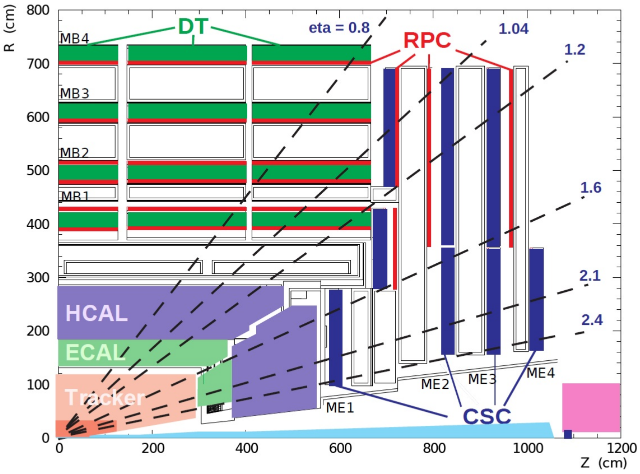

Figure 2.5.: Overview of the muon system with its three types of detector systems, drift tubes (DT) in the barrel region, cathode strip chambers (CSC) in the endcaps and resistive plate chambers (RPC) in both regions [44].

η there are inefficiencies at $|\eta| = 0.25$ and $|\eta| = 0.8$ due to gaps between the DT wheels as well as at $|\eta| = 1.2$ due to the transistion between barrel and endcap. In every DT chamber there are two independent units of drift cells, called superlayers, with anode wires along the z-axis to measure the r-ϕ-coordinate and one superlayer in between the two with wires orthogonal to the beam line to measure the z-coordinate. The latter one is not installed in the station which is most distant to the beam pipe. Every superlayer is made of four layers of rectangular drift cells shifted by half a cell to minimize ambiguities in the reconstruction. A schematic overview of a muon station with three superlayers is given in figure 2.6.

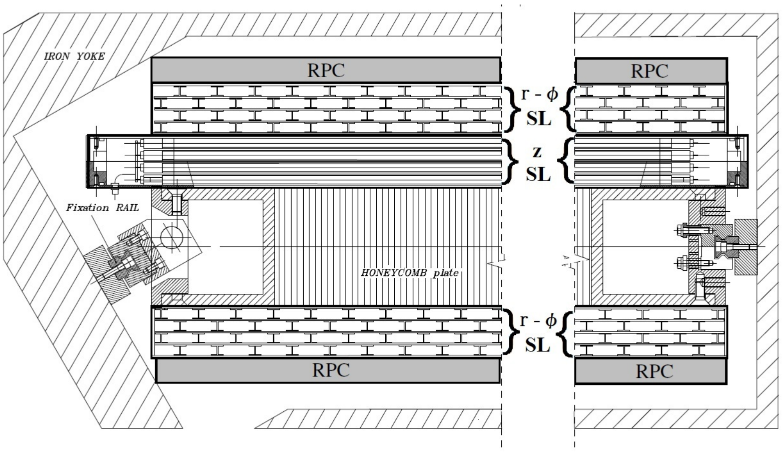

Figure 2.6.: A schematic overview of a muon station with three superlayers, adapted from reference [40].

The drift cell, illustrated in figure 2.7 is 42 mm long, 13 mm high and made of aluminium. In the center of the cell is a 50 μm thick anode wire made of gold-plated stainless-steel at a voltage of 3600 V. Two 50 μm thick aluminium strips at -1200 V at the short side of the rectangular drift cell act as cathodes. The field is additionally formed by two electrode strips at +1800 V, surrounding the anode from the long sides of the cell. The cell is filled with a gaseous mixture of 85 % Ar and 15 % CO_2. If a particle passes the drift cell, the argon atoms are ionized and accelerated towards the cathodes while the electrons move towards the anode. Because of the strong electric field, the particles close to the anode get enough energy to ionize further atoms, leading to a measurable current proportional to the deposited energy. The argon is used because it is a noble gas and therefore does not react, stays atomic and does not produce negatively charged ions, which would be much slower than the electrons. The CO_2 acts as a quenching gas to absorb photons and cool down the electrons via inelastic scattering and therefore making the detector faster. The mixture provides a linear dependency between time and drift path which is essential for the drift tube being a first-level trigger device. The maximal drift time is 380 ns according to an average drift velocity of 55 μm/ns. The single wire resolution is better than 250 μm allowing a global resolution of a chamber in r-ϕ of 100 μm.

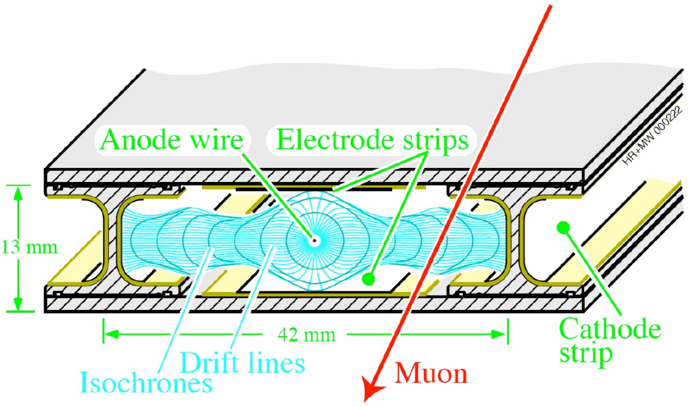

Figure 2.7.: A sketch of a drift cell showing the anode wire and the cathodes and isochones, from reference [40].

The Cathode Strip Chambers

In the endcaps the magnetic field is non-uniform, as well as the particle flux. This implies the choice of a fast and robust muon detector, such as the cathode strip chamber (CSC). The CSCs are trapezoidal and arranged in a circle around the beam direction. The CSCs cover the region of $0.9 < |\eta| < 2.4$. Summing up the data of the 936 CSC of both endcaps, they yield an area of 5000 m^2 and a gas volume of 50 m^3. There are four layers of CSC, separated by the yoke iron. A single CSC covers either 10° or 20° in ϕ.

The CSC are multi-wire proportional chambers made of seven trapezoidal panels of cathode strips with six gas gaps, each containing an anode wire plane. The gas mixture is 40 % Ar, 50 % CO_2 and 10 % CF_4, with CO_2 acting as an inflammable quencher and CF_4 prevents polymerization on wires. As shown in figure 2.8, the ionizing particle passing the CSC, produces ions and electrons that cause an avalanche of further charge carriers due to the high voltage. The cathode strips are directed radially to allow a measurement of ϕ, while the anode wires are oriented in ϕ-direction to obtain the r-coordinate. A spatial resolution for the CSC nearest to the interaction point of 75 μm is reached, while for the others a coarser resolution of 150 μm due to more separated wires is obtained.

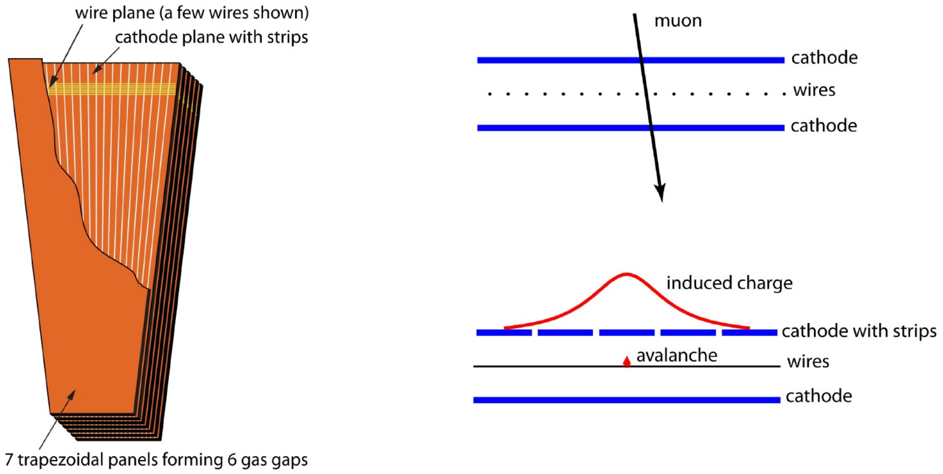

Figure 2.8.: The set-up (left) and functionality (right) of a cathode strip chamber [40].

The Resistive Plate Chambers

Resistive plate chambers (RPC) are implemented in the CMS muon system to provide an adequate spatial resolution and a time resolution ($\ll$ 25 ns) high enough to allow a matching of a certain detected particle and the bunch crossing[5] it originates from. The RPC are operating in avalanche mode and consist of two parallel chambers with a set of common aluminium read-out strips in between surrounded by two gas gaps of $\approx$ 2 mm, see figure 2.9. Each gap is confined by two 2 mm thick graphite coated bakelite plates that serve as electrodes and apply a high voltage of 7-12 kV. A dedicated gas distribution system is used for the RPC to maintain the right mixture of the relatively expensive gas components, mainly consisting of $C_2H_2F_4$. If a charged particle passes the detector, the gas gets ionized and due to the high voltage a charge avalanche is set off that induces a current in the aluminium which is then read out. Six layers of RPC are used in the barrel with a set of two in each of the first two muon stations (see figure 2.5) to obtain four measurements even for low-energy particles. In the endcaps three layers of RPC are installed up to a pseudorapidity of 1.6.

---

[5] A bunch crossing occurs every 50 ns in 2012, the design value is 25 ns.

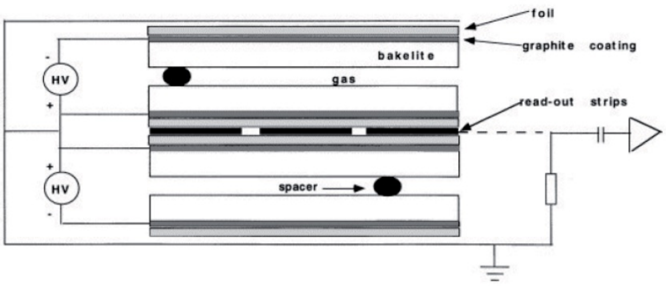

Figure 2.9.: A schematic view of a resistive plate chamber used in CMS. From reference [45].

2.2.4. The CMS Trigger System

In 2012 the LHC was operated at an event rate of 20 MHz, corresponding to a bunch crossing every 50 ns to achieve luminosities high enough to produce very rare processes (like Higgs boson production) at sufficiently high rates. This leads to the fact that the largest fraction of data is not needed to store. Furthermore, storing every event is physically not possible by far. To account for this, a dual triggering system is installed at CMS consisting of the Level-1 trigger and the High Level Trigger (HLT), which will be described briefly in the following.

The Level-1 Trigger

The L1 trigger (L-1) is made of custom-designed, programmable electronics which gather their input from the calorimeters and the muon system. The complete high-resolution data cannot be processed by the L1 because of the high rate and is therefore stored in pipelined memories in the front-end electronics. The L1 only uses a small coarsely resolved fraction of the actual data to decide, if the whole information is directed to the High Level Trigger or rejected. The L1 work flow can be divided into three components. At first, Local Triggers read out energy deposits at the calorimeter or determine track segments or hit patterns in the muon system. Then, the regional Triggers combine those information to form different trigger objects, such as muons or electrons.

Each of these objects is given a certain rank to quantify the confidence of having reconstructed the object sufficiently well. Thus, energy, momentum and the amount of information, as well as the detailed knowledge of the detector and the electronic system are defining how high a trigger object is ranked.

The highest ranked objects are then determined by the Global Calorimeter Trigger or the Muon Trigger, respectively, and transferred to the Global Trigger, which represents the last instance in the L1 system and decides whether the event is rejected or accepted and further investigated by the High Level Trigger. The decision is based on algorithm calculations and the readiness of the subdetector and the storage elements. The L1 trigger has an output rate of about 100 kHz.

The High Level Trigger

The High Level Trigger (HLT) is a purely software-based further data-filtering process. Unlike the L1, the HLT uses every information available to decide, if an event should be recorded or not. In this analysis a Single Muon High Level Trigger [46] is used which required a measured transverse momentum above 40 GeV. First, this trigger reconstructs the muons in the muon stations with basically the full detector information to verify the L1 muon identification and to refine the momentum measurement. Then, the trajectory is extrapolated to the tracker and tracking information is used to match a track to the muon. With information from the ECal and pixel tracker, isolation criteria can be applied to the muon candidate and muons from secondary vertices can be distinguished. The typical rate of the High Level Trigger is of the order of 100 Hz.

2.2.5. Luminosity Measurement

A very important quantity to know for almost every CMS analysis is the integrated luminosity, which is essential for every event count prediction. As can be seen in equation 2.2, the luminosity is computed from well adjustable quantities as number of bunches, number of particles per bunch and the revolving frequency, but also the effective overlap $A_{\text{eff}} = 4\pi\epsilon_n\beta^* F/\gamma_r$ (all quantities explained in equation 2.2) of the two bunches, which can only be determined precisely by measurement.
A possibility of measuring A_{eff} is the *Van der Meer scan* [47]. In this method the beams are shifted against each other in the transverse plane, separately in x and y direction. The event rate is then measured as a function of the shift to determine the beam shape. Since this method needs special fills, it is only performed once, when the beam parameters are changed. It is not directly used to measure the luminosity, but needed as a cross-check and calibration point for the *Pixel Cluster Counting* (PCC) method. The actual luminosity per bunch crossing used in this analysis is determined via the PCC [48], which utilizes the pixels in the most inner part of the CMS detector. Their high number of about $7 \cdot 10^7$ ensures that the probability of hitting one pixel by more than one track is at the per-mil level, even for the high event rates during the high-pileup runs. Thus, the number of hit pixels can be approximated as a linear function of the number of interactions per bunch crossing. The yielded luminosity measurement is provided with an uncertainty of 4.4 % for 2012, mainly stemming from an yet unknown systematic variation of the visible cross section over scan time.

3. Object Reconstruction And Computing Framework

The most important objects for this analysis are muons with high momenta (>100 GeV) and the reconstructed missing transverse energy corresponding to the neutrino. Their reconstruction in CMS is described in this chapter.

3.1. Muon Reconstruction

The following description of the muon reconstruction is based on [49, 50].

3.1.1. Muon Momentum Measurement

The main task of the muon reconstruction is to determine the muon trajectory using the signals of the tracker and the muon system which assign positions in space and time, so called hits, to the muon. The trajectory of the muon is bent by the Lorentz force induced by the strong magnetic field. Thus, measuring the curvature and its direction is sufficient to determine the transverse momentum and the sign of charge of the muon. The total momentum can then be estimated by measuring the polar angle of the muon trajectory.

In a real detector certain distortion parameters have to be taken into account: The magnetic field is not homogeneous in the whole detector, i.e. B=B(x,y,z). Secondly, the particles lose energy while travelling through the detector due to bremsstrahlung and thirdly, stochastic multiple scattering occurs. The latter is most relevant for a particle traversing the iron yoke, but can also occur in other solid detector parts. In order to deal with the distortions occurring in a real detector, dedicated track reconstruction algorithms have been developed for muon tracks, which are explained in the following.

3.1.2. Tracking Algorithm Overview

To convert the hits in the position sensitive subdetectors into a track, a pattern recognition algorithm is used. It is used to reconstruct tracks in the muon system (so called standalone tracks) as well as tracks in the silicon tracker (so called tracker-only tracks). Using the same track finding method in tracker and muon system is possible due to a generic interface shared by both subdetector systems. The tracking algorithm consists of the following four parts:

- **Trajectory Seeding**: To build a trajectory, a starting point, called seed, is needed for the tracking algorithm. A seed requires a set of hits that is compatible with the beam spot as the initial vertex. It is possible to set constraints on the geometric location of the hits seeding the track or on the initial direction.

- **Trajectory Building**: Starting at the trajectory seed, trajectory building proceeds in the direction specified by the seed by successively searching for matching hits in the following detector layers. The decision, if a hit belongs to a track, is based on a combinatorial Kalman filter. Iteratively with every layer, the Kalman filter updates the estimate of the momentum p and its covariance matrix by also taking into account scattering effects and energy losses. Finally, the trajectory estimate is weighted with information of all of the considered layers including the last one. The detailed behaviour of a muon traversing the inhomogeneous magnetic field and matter like the iron yoke has to be taken into account. This is done by using so called *propagators*, algorithms that take into account the dependency of the muon trajectory on the traversed material and the B-field.

- **Trajectory Cleaning** and **Smoothing**: A large amount of trajectories are built by the algorithm, with many of them overlapping each other by sharing large number of same hits. Those ambiguities are resolved e.g. by choosing a measure of quality, e.g. the χ^2 per degree of freedom of the fit, to decide for a certain track and reject others.
  Afterwards, a fit is applied backwards using all covariance matrices and applying them to all intermediate points.

3.1.3. Stand-alone, Global and Tracker Muons

Muon tracks are separately reconstructed in the muon system (standalone muons) and in the silicon tracker (tracker-only muons).

Standalone muon reconstruction starts with a seed state estimated online by the L-1 trigger and with track segments from the offline reconstruction. Before the final filtering of the track is applied (as explained in the previous subsection), a pre-filter which uses a looser χ^2 requirement is applied to reduce the possible bias from the seed. While the pre-filter is applied in inside-out direction, the final filter's direction is reversed. After the fitting, cleaning and smoothing, the tracks are extrapolated to the point of closest approach to the beam line. The resolution of the standalone muon is dominated by multiple scattering for muons with a momentum up to 200 GeV.

In order to combine the independent measurements of tracker and muon system, two different approaches are made depending on the muon momentum and the quality of its reconstruction. Those will be described in this subsection.

The Global Muon

The most important muon reconstruction technique for muons with transverse momenta above several GeV is the global muon reconstruction. The idea behind is to obtain the

most accurate description utilizing as many detector information possible with the inner tracker and the muon system providing measurements of the track parameters complementing each other. After combining tracks and muon information, a global fit to all hits is performed. Starting from the standalone muon track, the algorithm searches for matching tracker-only tracks, so its an outside-in approach. At first, for every standalone track, a region of interest is defined. Every tracker-only track lying inside is considered as a matching track. The origin position is chosen as the reconstructed primary vertex (or beam spot, if no vertex is found). Only tracker tracks are considered with a transverse momentum greater than 60 % of the standalone track.
After reducing the possible tracks geometrically, a global track fit is applied for each of the remaining tracker-only - standalone pairs. If more than one fit is possible, the track with the best χ^2 is chosen. Therefore, only one global track remains for each standalone track.

The Tracker Muon

The global muon method provides a robust and precise reconstruction of most of the detected muons. However, if a muon did produce only very few hits in the muon system because of its very low momentum or traversing blind spots in the detector, a different approach is often more successful. The tracker muon is constructed by starting at a tracker-only track with a transverse momentum higher than a certain threshold. Instead of a global fit, the tracker track is propagated to the calorimeter and then to the muon system taking into account multiple scattering and the B-field. The algorithm stores the energy deposited in all crystals and towers which are crossed by the extrapolated muon track as well as hits nearby the track in the muon system.

3.1.4. Dedicated High p_T Muon Reconstruction

When passing the iron yoke, multiple scattering and energy losses via radiation can impact the muon trajectory and momentum assignment. While the first one is not problematic for high p_T muons, because the deflection angle decreases with higher momentum, the latter one can significantly change the muon energy and particle showering can be induced which makes the reconstruction more difficult. To account for that, several specialised algorithms were developed. Two of them are introduced in the following.

- **Tracker-Plus-First-Muon-Station (TPFMS) fit**: The TPFMS is an algorithm that starts at the global fit. From the muon system, it uses only the very first station hits, thus reducing the sensitivity to particle showering in other stations.

- **The Picky Fit**: This refit also starts at the global fit. The algorithm decides, if a chamber is hit by showers, based on the hit occupancy of the chamber. In such chambers only the hits which are found to be compatible with the refit (based on a χ^2 comparison) are taken into account.

In this thesis the *cocktail algorithm* (or *Tune P*) is used to decide which track is taken into the analysis. It is a mixture of the above mentioned algorithms yielding the best resolution for high-p_T muons as displayed in figure 3.1, where the resolution of the different muon reconstruction algorithms is shown measured with cosmic muons in 2010.

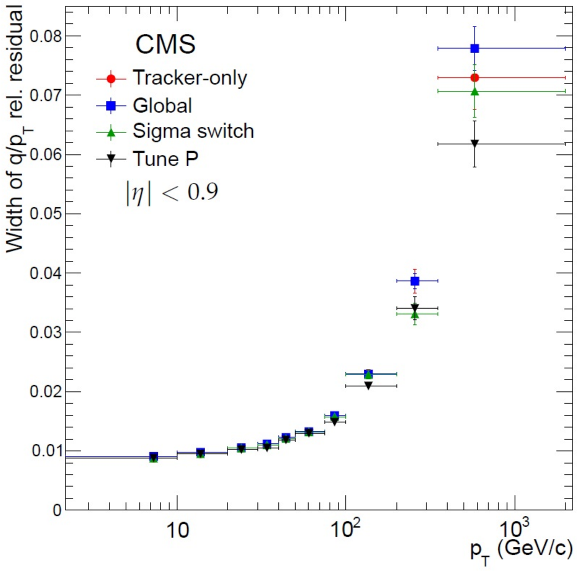

Figure 3.1.: p_T-resolution of the tracker, global and cocktail (Tune P) muon reconstruction algorithms. The cocktail algorithm performs best at high energies. From reference [50].

If the inner tracker $\mathrm{p_T}$ is above 200 GeV, the Picky Fit is chosen, if its track is valid, i.e. the χ^2, and the numbers of degrees of freedom of the fit are above zero. If not, it chooses the TPFMS Fit and then the global tack [51]. If none of these tracks is valid or if the chosen one's fit quality is below a certain threshold, the inner tracker's $\mathrm{p_T}$ is chosen and similar, if the muon's inner tracker $\mathrm{p_T}$ is below 200 GeV.

3.2. Reconstruction Of The Missing Transverse Energy With The Particle Flow Algorithm

The second part of the considered final state in this thesis is the missing transverse energy (MET). Since the transverse momentum of the initial state (two protons) is negligible compared to the final state and momentum conservation applies, the MET has to correspond to one or more particles leaving the detector undetected, i.e. a neutrino. Other sources of MET are misreconstructed momenta and particles leaving the detector outside its acceptance. Those effects cause so called instrumental MET. In order to yield a good estimation of the MET, the transverse momenta of all particles possible have to be measured adequately. There are several approaches to determine the MET. In this analysis particle flow MET is used [52]. The particle flow event reconstruction is based on identifying and then reconstructing all stable particles inside of the detector. Hence, the energy, direction and type of muons, electrons, photons, as well as charged and neutral hadrons are determined by utilizing the corresponding detector components for every particle type. The principle of Particle Flow reconstruction is to reconstruct charged particle tracks with tracker information only using very high quality criteria first, remove their corresponding hits from the collection and then loosen the criteria iteratively to reconstruct further particles. After that other detector information is additionally used, e.g. the muon system for muons. After subtracting muons and electrons from the particle collection, charged hadrons are identified and subtracted by using information of the tracker and the HCal. Remaining calorimeter entries are identified as photons or neutral hadrons, depending on the relative energy entries in HCal and ECal. The information about every particle in each event is then used to calculate the energies or momenta of High-Level objects like jets and the MET.

For this analysis, the so called Type-I Corrected MET was used [53]. It takes into account jet energy corrections applied to jets with a p_T >10 GeV. A correction is needed to translate the measured energies to the true energy of the parton or particle because the calorimeter response has no linear dependence on the jet energy.

Since the particle-flow algorithm does not necessarily determine the same muon p_T as the cocktail algorithm, the MET has to be corrected for this in order to stay consistent.

3.3. Computing Framework

While CERN being the obvious center of the LHC and CMS collaboration, many analysts are working at over 600 universities [54] in more than 80 nations. Not only the physicists, but also the computing resources are spread all over the world to ensure a sufficient computing power for the LHC analyses. The resources are organized in the Worldwide LHC Computing Grid (WLCG) [55]. The WLCG is used to store, distribute and analyse around 15 Petabytes of data produced by the LHC and its experiments on an annual basis. The WLCG is structured in four layers, called ”Tiers” 0, 1, 2, and 3. The Tier 0 located at CERN is the computing center and the starting point for the distribution of all the LHC data, but it makes up less than 20 % of the overall computing capacity. It covers the tasks of the first processing and reconstruction of the LHC data. The eleven Tier 1s are responsible for data-saving, large-scale reprocessing and distributing the data to Tier 2s, being equipped with large storage capacity. At those Tier 2s, which are generally managed by universities, and the smaller Tier 3s, the data is then processed by the analysts. Not only the recorded data, but also a big amount of simulated data is generated at the Tier 1s and distributed to the Tier 2s to be accessible to analyses.

In order to have a global and uniform software framework to analyse the data, the CMS Software (CMSSW) is provided [56]. It is used for object reconstruction and to maintain access to the data and storing it as well as for the production of simulated events, the so called Monte-Carlo samples. The versions used for the processing of data and Monte-Carlo are CMSSW 5_2_X and CMSSW 5_3_X. The CMS data events are stored in three different data formats:

- **RAW**: The RAW data contains the detector data, the level 1 and HLT trigger result and some of the higher-level objects, like jets, created by the HLT. This format needs relatively large event sizes of the order of MB and while in principle it is possible to use it for analyses, the event size is too big for the average analysis.
- **RECO**: RECO is derived from RAW data and contains the objects reconstructed by the event reconstructing program [57]. It contains the high-level objects such as b-jets as well as the lowest level information, e.g. hits and segments, but it is more compact than the RAW format, because the data is more compressed and redundant information is deleted.
- **AOD**: AOD is the most condensed data format of the mentioned three and is derived from the RECO. It provides the detector information and objects in a compact way by not containing all of the hits, which makes it possible for every Tier 1 to store a full copy of the AOD, while only holding a subset of RAW and RECO samples. The average event size is reduced to the order of 100 kB.

In this analysis only the AOD data format is used with the exception of one standard model background Monte Carlo, only available in RECO. Because the AOD format is still not practicable for this analysis, it is further condensed by the use of the ACSUSY-Analysis skimming software [58]. It filters the part of the data needed for the analysis and stores it in NTuples of ROOT data files [59], which reduces the AOD samples to a size manageable by the local computing resources. The evaluation of those NTuples, for instance plotting of results, is done with the ROOT software, which is especially developed for high energy physics purposes as it is capable of processing large amount of data in relatively short time. For statistical analysis the RooStats-based [60] tool developed for the Higgs analysis was used [61].

4. Signal Properties

This thesis covers searches for a SSM W' and four-fermion contact interaction. This chapter is meant to provide an overview of the simulation of the signal samples as well as about their technical and physical properties.

4.1. Generation of Samples

In order to get an idea how those new physics processes would manifest themselves in the detector qualitatively and quantitatively, signal event simulations have been performed. All signal samples used in this analysis have been generated in leading order (LO)[1] with Pythia 6 v.426 [24] by the CMS event generation group. Since both processes do not interfere with the standard model W, it is possible to produce them alone. Despite only using QCD LO calculations, Pythia is capable of simulating hard sub-processes, the underlying event[2] and initial and final state radiation as well as parton showering and hadronization. It uses a combination of analytical results and QCD-based models, since it cannot be calculated perturbatively. Afterwards, the event information on *generator level*[3] is propagated to a detector simulation of the CMS experiment based on the GEANT 4 simulation tool kit [62] to account for the interaction between the produced particles and the detector material. In order to be consistent with the recorded data, also the various triggers are simulated within the event generation.

All Monte Carlo samples have to be weighted according to the integrated luminosity $\mathcal{L}_{\text{int}}$ of the measured data to have a correct estimation of the amount of predicted events. Assuming that a Monte Carlo sample has been produced with a cross section σ and an event count of N_{gen}, the number of predicted events N_{pred} at $\mathcal{L}_{\text{int}}$ is then $N_{\text{pred}} = \sigma \cdot \mathcal{L}_{\text{int}}$. Therefore, each event of the sample has to be weighted with the ratio R between expected and generated events, i.e.:

$$R = \frac{N_{\text{pred}}}{N_{\text{gen}}} = \frac{\sigma \cdot \mathcal{L}_{\text{int}}}{N_{\text{gen}}} \tag{4.1}$$

---

[1] The term leading order denotes that the cross section has been calculated by only taking into account diagrams with the lowest possible (non-zero) number of vertices for the considered process

[2] Processes involving quarks that remain after the inelastic proton-proton scattering

[3] This term summarizes the information about the ”true” kinematics, particle types, etc. before simulating detector effects.

4.2. SSM W' Signal: Production and Properties

As already mentioned in section 1.2.3, the Sequential Standard Model is implemented in Pythia 6 and considered in this analysis. The branching ratio for the decay of the W' to muon and neutrino (decay to WZ suppressed) amounts to around 8 %. Samples with a W' mass from 0.3 to 4.0 TeV have been produced in steps of 0.1 TeV between 2.0 and 3.5 TeV and in steps of 0.2 TeV between 0.3 and 1.9 TeV, as well as for 3.7 and 4.0 TeV. The absence of interference with standard model processes allows for a relatively low generated event count for the signal samples, hence about 20’000 events per W' mass point have been produced.

4.2.1. W' Cross Sections

The W' cross section decreases with increasing $M_{W'}$ because of the reduced phase space to generate such a heavy particle. The cross section given by the event generator Pythia at leading order and the W' Pythia cross sections are scaled to account for higher order diagrams with the so called k-factor, which is in this case defined as

$$k = \frac{\sigma_{\text{NNLO}}}{\sigma_{\text{LO}}}, \tag{4.2}$$

where σ_{NNLO} is the cross section in next-to-next-to leading order in the strong coupling. It is determined with the NNLO calculator FEWZ[4] [63]. The NNLO cross section decreases from 140 pb for $M_{W'} = 0.3$ TeV to 0.2 fb for $M_{W'} = 4.0$ TeV [64], hence over six orders of magnitude. The cross section limit set in [1] of $M_{W'} = 2.75$ TeV is 2.4 fb. The Pythia samples are produced with the PDF set CTEQ6l1 while FEWZ relies on the MSTW2008 scenario. The properties of the two PDF sets are explained in detail in section 4.4. In figure 4.1 the NNLO and LO cross sections are compared. It can be seen that the additional orders result in a constructive contribution to the leading order, i.e. the cross section is increased.

Simply multiplying the LO cross section with the k-factor is done under the assumption that the impact of higher orders to kinematics can be neglected, e.g. the $\mathrm{M_T}$ shape stays the same. The k-factor has a minimum at 2.5 TeV of 1.14 and goes up to around 1.33 for low (0.3 TeV) and high (4.0 TeV) W' masses. Generally, one can deduce from this that the higher-order corrections are getting lower with increasing invariant masses of the produced W'. The subsequent increase of the k-factor for $M_{W'} > 2.5$ TeV is due to the increasing off-shell[5] production, which is shown later in 4.3. The parton-parton center-of-mass energy is then too low to produce the heavy W' on-shell.

4.2.2. W' Signal Properties

At the LHC, a W' would be dominantly produced via quark-antiquark annihilation as shown in figure 4.2.

---

[4] **F**ully **E**xclusive **W** and **Z** production

[5] i.e. far away from the mass resonance

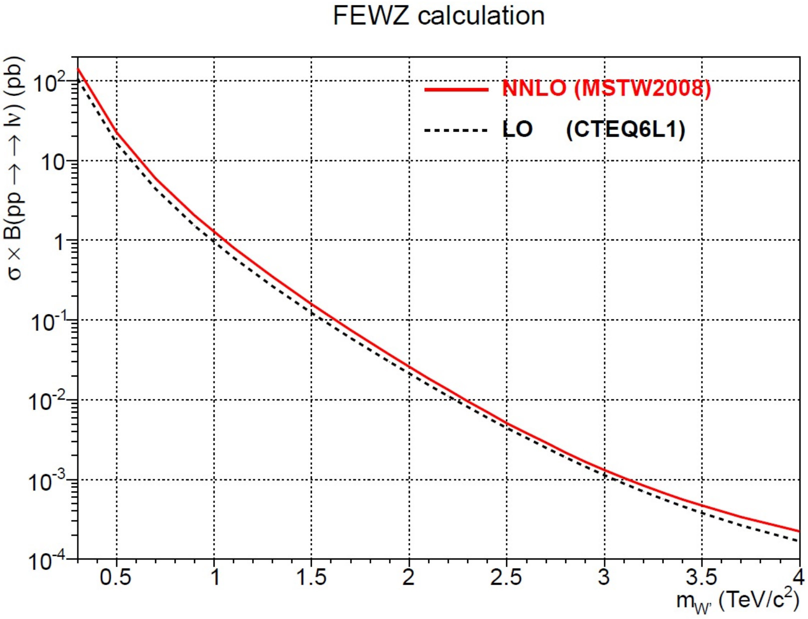

Figure 4.1.: A comparison between LO and NNLO cross sections of the W' as a function of $M_{W'}$. From the analysis note AN-12-172 [64].

Heavy on-shell W' are produced approximately in rest, since almost all energy is incorporated by the mass. Due to the fact that the W' decays into only two particles, the muon and the neutrino have definite momenta $p_\mu = p_\nu = M_{W'}/2$ in the W' rest frame. Full momentum information of both particles would therefore allow to reconstruct the invariant mass of the W', leading to a clear resonance (without taking detector effects into account, yet). Unfortunately, the neutrino cannot be detected directly with CMS. But, since the transverse momentum of the colliding partons is negligible, conservation of momentum allows to reconstruct its transverse momentum as the *missing transverse energy* (MET), which then is computed by (see equation 1.50).

$$M_T = \sqrt{2 \cdot p_T^\mu \cdot \mathrm{MET} \cdot (1 - \cos(\Delta\phi_{\mu,\mathrm{MET}}))}. \tag{4.3}$$

As described in section 1.4.1, a Jacobian peak is expected in the p_T^μ and $\mathrm{M_T}$ distribution. Since a hadronic recoil (see more detailed discussion in section 7.4) can lead to high transverse momenta of the W', the $\mathrm{M_T}$ spectrum is preferred, since it is not as sensitive as p_T^μ. A comparison of the invariant and the transverse mass for different W' masses is given in figures 4.3a and 4.3b. In figure 4.3a the mass resonances can be seen, following a Breit-Wigner distribution. As written in equation 1.33, the width is proportional to $M_{W'}$. The Jacobian peak at the different values of $M_{W'}$ can be seen in figure 4.3b. One can also see that heavier W' are preferably produced off-shell. This can be explained with the PDFs. As displayed in figure 4.6 the probability for a parton to carry a fraction of the proton momentum large enough to reach $\sqrt{s} = M_{W'}$ of about 2-4 TeV is strongly decreasing, which enhances off-shell production. The second peak in the mass distribu-

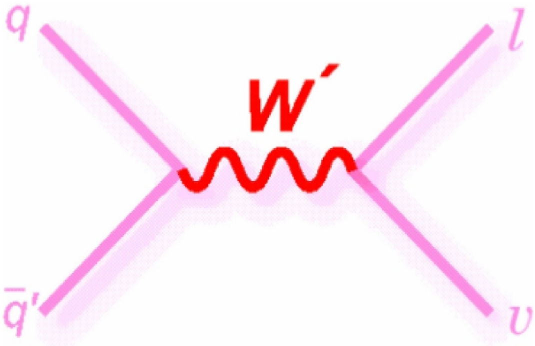

Figure 4.2.: A Feynman diagram of a W' produced at a hadron collider and decaying into a charged lepton and a neutrino.

tion at $M = 0$ GeV is caused by a divergence in the PDF for small x and regularized in Pythia by a closing of the phase space [24].

4.3. Contact Interaction: Production and Properties

As already mentioned, the contact interaction samples have also been produced by the generator group with Pythia 6 v426 in leading order. Because of its different chiral structure compared to the standard model W there is no interference between the CI and SM processes, i.e. the CI signal could also be produced alone. However, the Pythia implementation allows only for a production together with the $W \to \mu\nu$. The reason is that this model has been implemented analogously to another CI model, the left-left-isoscalar model [24], which does interfere with the W and therefore has to be produced together with the W. Unfortunately, the implementation in Pythia does not allow to distinguish between particles produced via CI and via W. In order to get the signal cross section and the signal shape despite of this fact, the W is simply produced separately and subtracted from the CI + W sample.

One problem is encountered, though, regarding statistical limitations. If the cross section of the W is several orders of magnitude above the CI cross section, as it is near to the W resonance, the statistical fluctuation of the W contribution lies in the same order of magnitude as the CI event count, which makes the separation impossible. And also, if the W mass peak is included in the CI+W production, most of the produced events contain an on-shell W with a mass of about 80 GeV. Thus, the generated event rate in the region of interest containing energies of several hundred GeV, where the ratio between signal and background is more advantageous, is much too low. To account for this, the W+CI samples are generated with the requirement that the muon p_T is above 300 GeV in the W and CI center-of-mass system, respectively. In this region the LO W cross section lies at around 18.9 fb, while the pure CI cross section ranges from 541 fb ($\Lambda = 3$ TeV) to 1.57 fb ($\Lambda = 13$ TeV). Here, Λ is the energy scale of the contact interaction model. This can of course only be done after reweighting the W sample and the CI+W sample to the same integrated luminosity. The CI+W samples are produced

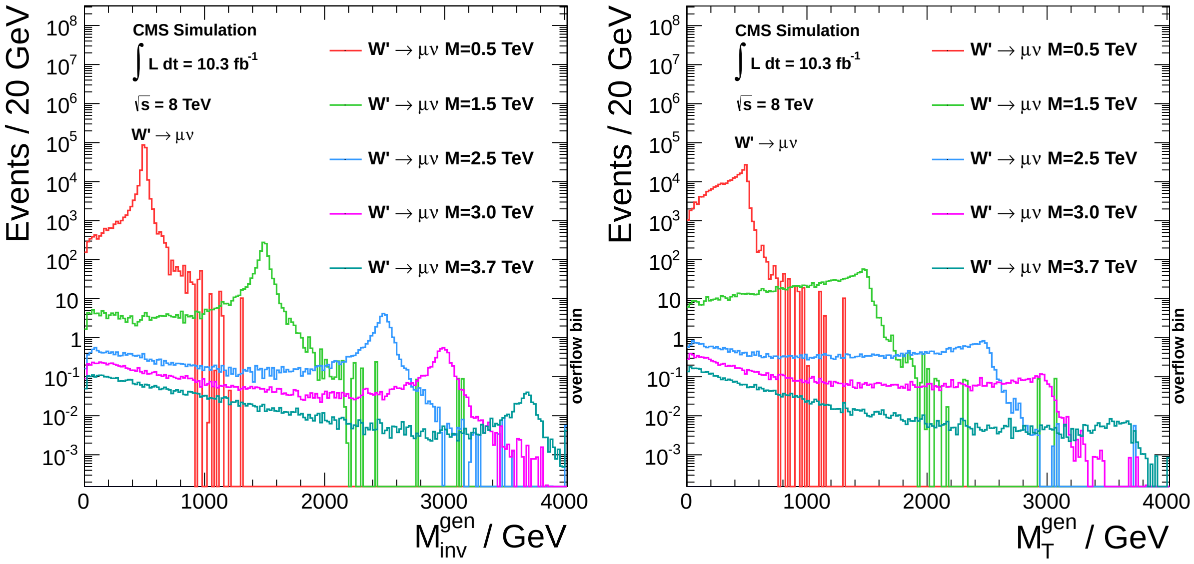

(a) The invariant mass distribution.

(b) The transverse mass distribution.

Figure 4.3.: The invariant (a) and transverse (b) mass distribution of muon and neutrino on generator level for different $M_{W'}$. An increase of the decay width can be seen as well as the decreasing cross section and an increasing off-shell production for higher $M_{W'}$. In (b) the Jacobian peaks can be seen at $M_{W'}$.

with an event count of 10^5 per sample in a range of Λ =3-17 TeV in 1 TeV steps, while the W sample contains 10^6 events.
The cut on the muon p_T does not decrease the sensitivity of the search which is explained further in section 9.1, since the lower p_T region has a much worse signal-to-background ratio.

4.3.1. The Contact Interaction Cross Section

As described in section 4.13, the contact interaction cross section is proportional to Λ^{-4}. This behavior can be seen in figure 4.4.
Next-to-leading-order corrections have not yet been taken into account, since no NLO generator was found, which had the HNC model implemented. Even, if the contact interaction is an effective theory, NLO corrections could be applied to a certain degree without further assumptions to the underlying physical process [34].

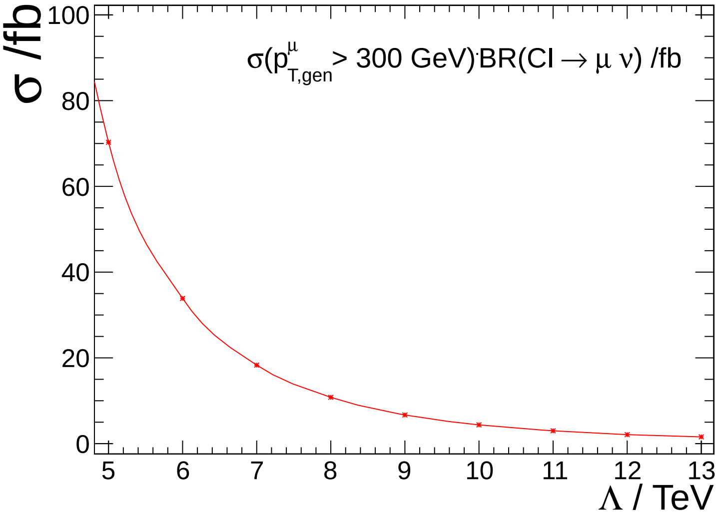

Figure 4.4.: The four-fermion contact interaction cross section as a function of Λ.

4.3.2. Contact Interaction Signal Properties

The contact interaction cross section increases linearly with the center-of-mass energy $\sqrt{\hat{s}}$. However, this behavior is not reflected in the transverse momentum spectrum of the muon or in the transverse mass spectrum of the contact interaction as shown in figure 4.5b. One can see a falling behavior of a non-resonant spectrum. The decrease is of course explained by the PDFs of the quarks involved in the contact interaction which strongly decrease for higher momentum fractions. Therefore, the CI cross section falls, since it is folded with the PDFs. In figure 4.5a the transverse mass distributions of the actual produced samples containing CI and W are shown. The distribution in figure 4.5b is yielded by subtracting the W as explained in the previous section. One can see the

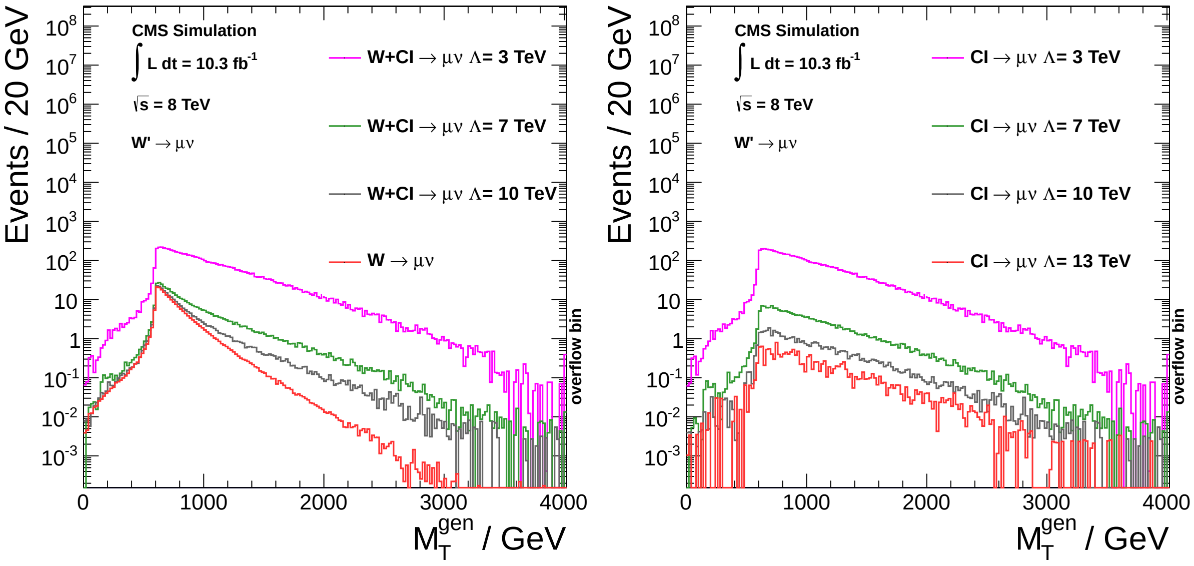

(a) M_T of W+CI.

(b) M_T of the CI only.

Figure 4.5.: The transverse mass distribution of muon and neutrino on generator level for (a) CI+W and (b) CI only. The generator cut on $p^{\mu}_{T,\mathrm{cms}} = 300$ GeV is visible at $M_T = 600$ GeV. In (b) the W is subtracted leading to a higher statistical fluctuation for higher values of Λ.

increasing fluctuation for higher values of Λ due to the decrease of cross section of the CI part relative to the W. One can observe that the shape of two CI signals for different energy scales $\Lambda_1 < \Lambda_2$ does not change, but only the cross section decreases by

$$\sigma_2 = \sigma_1 \cdot \frac{\Lambda_1^4}{\Lambda_2^4}. \tag{4.4}$$

To avoid statistical fluctuations as much as possible, for the limit setting in section 9.1, only the signal efficiency[6] of the $\Lambda = 3$ TeV sample is needed, which can be used to determine the CI part with maximal precision.

In figures 4.5a and 4.5b the generator cut on $p^{\mu}_{T,\mathrm{cms}} = 300$ GeV in the center-of-mass system of the CI and W is visible, since the spectra begin at about $2 \cdot \hat{p_T} = 600$ GeV. Few CI events also occur under the threshold of 600 GeV. The reason for this is that the muon can radiate a γ as final state radiation decreasing its momentum.

4.4. PDF Uncertainties on the Signal Cross Section

As shown in section 1.3, the estimated signal cross section relies on the underlying parton density functions of the proton (PDFs). In the following chapter the calculation of

---

[6] The signal efficiency denotes the ratio of the signal cross section above a certain parameter, here $\mathrm{M_T}$, to the total signal cross section.

the uncertainty on the W' and CI production cross sections is explained. It follows the recommendation of the PDF4LHC [65] working group, which also includes the uncertainty on the strong coupling α_s.

The calculation is based on the three PDF sets CTEQ[7](CT10) [66], MSTW[8]2008 [67] and

NNPDF[9]2.1 [68]. For the production of Monte Carlo signal samples, the PDF set CTEQ6L1 (LO in α_s) was used by the Pythia 6 generator. In figure 4.6 the MSTW (NLO in α_S) results for PDFs of different partons for two different energy scales are shown. For small values of the momentum fraction x, the gluon dominates over the quarks. All PDFs are monotonously falling with the exception of u and d due to the valence quarks. The uncertainty, visualized by the widths of the bands, increases for low values of x.

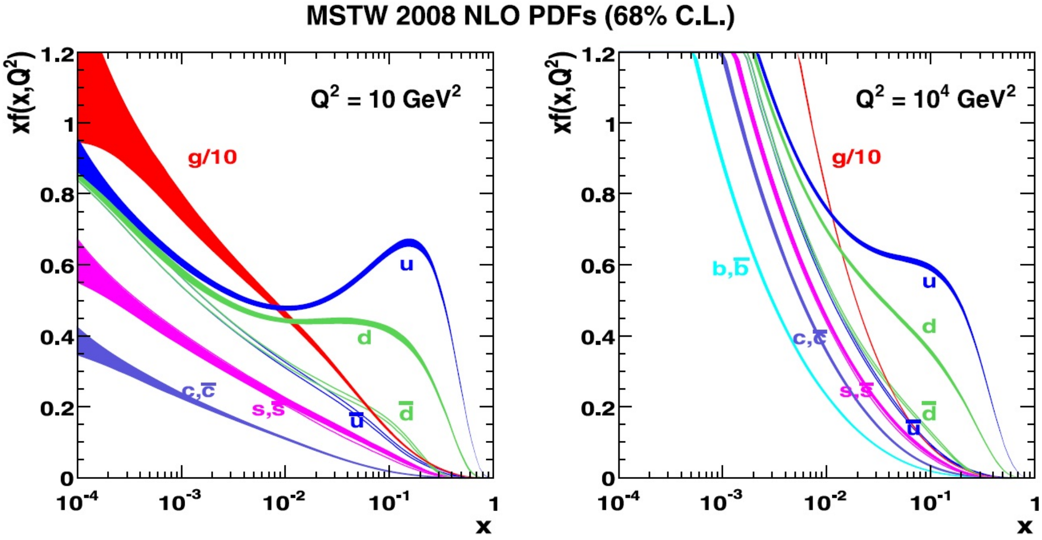

Figure 4.6.: Parton density functions of the proton at two different values of momentum transfer Q. The widths of the bands represent the 68 % C.L. [67]

Since a theoretical estimate of the PDFs is not yet possible due to the divergence of cross sections for small energies in pertubative QCD, the different PDF working groups perform global fits at next-to-leading-order in the strong coupling α_s on the available deep-inelastic scattering (DIS) data, mainly originating from TeVatron, HERA, and fixed-target experiments. If e.g. a DIS cross section σ_{AB} involving parton A and B is measured at a certain scale Q^2 and momentum fractions x_1, x_2, it can be compared to

---

[7] **C**oordinated **T**heoretical-**E**xperiment Project on **Q**CD

[8] **M**artin, **S**tirling, **T**horne, **W**att

[9] **N**eural **N**etwork **P**arton **D**istribution **F**unction

the theoretical prediction via

$$\sigma_{AB}(Q^2, x_1, x_2) = \sum_{a,b=q,g} \hat{\sigma}_{AB} \cdot f_{a/A}(x_1, Q^2) \cdot f_{b/B}(x_2, Q^2), \tag{4.5}$$

analogously to equation 1.47. $\hat{\sigma}_{AB}$ can be expanded as perturbative series in α_s. If one now takes the PDF of a certain type of parton as a function of x at a reference scale Q_0^2 containing about five free fit parameters, one can obtain $\alpha_s(Q_0^2)$[10] and the free parameters from fitting to the measurements of σ_{AB}. The scale dependence of f_i and α_s can then be evaluated using the so called DGLAP[11] evolution equation [69].

CTEQ and MSTW both use a χ^2-based Hessian approach for their fit: The *best fit* is defined as the one with the lowest χ^2. The values of the free parameters obtained by the fit are then varied up and down by one standard deviation to estimate uncertainties. To do so, the parameter space is orthogonalized first via diagonalizing the Hessian matrix to account for possible correlation among the parameters. In this context the Hessian matrix contains the second derivatives of χ^2 with respect to the fit parameters and large off-diagonal elements (relative to the diagonal elements) indicating large correlations. Every variation results in a new PDF. This leads to N_{mem}=$2N_p$+1 different PDFs, including the *best fit*, with N_p being the number of free parameters (N_p=26 for CT10 and N_p=20 for MSTW) and N_{mem} being the number of so called *members* of each PDF set. N_p is the sum of all free parameters of all PDFs $f_{q,g}$.

NNPDF follows a different approach. In the first stage Monte Carlo samples, so called *r*eplicas are produced around points in space of physical parameters where data exists, following a multi-gaussian distribution. Secondly, neural networks are used to interpolate between data points. Instead of the *members* used by CTEQ and MSTW to evaluate uncertainties, NNPDF provides 100 *r*eplicas distributed around the best fit.

Another source of uncertainty is the input value of α_s. Its influence is evaluated varying it by one standard deviation $\Delta\alpha_s(M_Z)$ regarding the theoretical uncertainty at the Z peak. The different input values of the groups are $\alpha_s(M_Z)$ = 0.118 by CTEQ, $\alpha_s(M_Z)$ = 0.119 by NNPDF and $\alpha_s(M_Z)$=0.12018 by MSTW (coming from the MSTW fit).

Since producing new signal samples with all the different PDF sets to determine the influence on the signal cross section would be too resource-intensive, a different method is suggested in [70]. In this analysis every event is then simply reweighted by the ratio between the cross-section prediction of the new PDF set and the prediction by CTEQ6L1, which was used for the signal simulation.

This is done with files provided by the LHAPDF group [71] containing the PDFs defined by the analytic functions that are fitted by the PDF groups, together with the parameter fit results and special Q^2-evolution functions.

For the i-th PDF of a set, a corresponding new cross section $\sigma^{(i)}$ is therefore calculated by multiplying the cross section σ^{prod} corresponding to the CEQ6L1 PDF, with the ratio of the sum over all event weights w_j and the total generated event number

---

[10] $\alpha_s(Q_0^2)$ is only treated as a free fit parameter by MSTW. CTEQ and NNPDF put in a fixed value obtained by other measurements.

[11] **D**ockshitzer-**G**ribov-**L**ipatov -**A**ltarelli-**P**arisi

n^{prod} :

$$\sigma^{(i)} = \sigma^{\text{prod}} \cdot \frac{1}{n^{\text{prod}}} \sum_{j=1}^{n^{\text{prod}}} w_j \tag{4.6}$$

The uncertainties arising from the PDF sets based on the Hessian method are estimated by comparing the different members with the best fit, while for NNPDF a different approach is recommended using the replicas. The two methods are briefly summarized in the following:

For the Hessian-based sets the asymmetric 68 % C.L. PDF uncertainty is calculated with the formulae 4.7, 4.8. $\sigma_{\text{ev}}^{(0)}$ is the cross section in the best fit scenario. $\sigma_{\text{ev}}^{(2i-1)}$ and $\sigma_{\text{ev}}^{(2i)}$ correspond to an upward and downward variation of fit parameter i of one standard deviation. Therefore, $\Delta\sigma^{\text{Hess}}(PDF,+)$ and $\Delta\sigma^{\text{Hess}}(PDF,-)$ take into account the highest positive and negative deviations, respectively. C_x is a factor needed to rescale a x % confidence level interval into a 68 % level which is necessary because of different approaches of the different working groups.

$$\Delta\sigma^{\text{Hess}}(\text{PDF},+) = \frac{1}{C_x}\sqrt{\sum_{i=1}^{N_{\text{mem}}/2} (\max\{\sigma^{(2i-1)} - \sigma^{(0)}, \sigma^{(2i)} - \sigma^{(0)}, 0\})^2} \tag{4.7}$$

$$\Delta\sigma^{\text{Hess}}(\text{PDF},-) = \frac{1}{C_x}\sqrt{\sum_{i=1}^{N_{\text{mem}}/2} (\max\{\sigma^{(0)} - \sigma^{(2i-1)}, \sigma^{(0)} - \sigma^{(2i)}, 0\})^2} \tag{4.8}$$

CTEQ and MSTW also provide $\alpha_s^{\pm}$-PDFs, where α_s is varied up/down by $\Delta\alpha_s$, respectively. The emerging uncertainty $\Delta^{\text{Hess}}(\alpha_s,\pm)$ is calculated in equation 4.9.

$$\Delta\sigma^{\text{Hess}}(\alpha_s,\pm) = \frac{1}{C_x}(\sigma^{(\alpha_s,\pm)} - \sigma^{(0)}) \tag{4.9}$$

The PDF and α_s uncertainties are then added quadratically (see equation 4.10) to yield a total uncertainty.

$$\Delta\sigma^{\text{Hess}}(\alpha_s + PDF,\pm) = \sqrt{(\Delta\sigma^{\text{Hess}}(PDF,+))^2 + (\Delta\sigma^{\text{Hess}}(\alpha_s,\pm))^2} \tag{4.10}$$

In the case of NNPDF $N_{\alpha_s} = 7$ sets are provided, each with a different $\alpha_s(M_Z)$, varied between 0.116 and 0.122 in steps of 0.001. Therefore, a combined PDF and α_s uncertainty $\Delta\sigma^{\text{NNPDF}}(\text{PDF} + \alpha_s)$ is directly computed, which is displayed in equation 4.11. Each set contains $N_{\text{rep}} = 100$ replicas. A Gaussian distribution of $\alpha_s(M_Z)$ with mean 0.119 is assumed and according to that the sets with a high difference in $\alpha_s(M_Z)$ to the mean get a smaller weight w_j than closer ones. σ^{ref} is the weighted mean of all replicas.

$$\Delta\sigma^{\text{NNPDF}}(PDF + \alpha_s) = \sqrt{\frac{1}{N_{\text{rep}} \cdot w_{\text{sum}}} \sum_{j=1}^{N_{\alpha_s}} w_j \cdot \sum_{k_j=1}^{N_{\text{rep}}} [\sigma(PDF^{(k_j,j)}, \alpha_s^{(j)}) - n_{\text{ev}}^{\text{ref}}]^2} \tag{4.11}$$

The uncertainty due to NNPDF is symmetric by construction.
It is recommended by the PDF4LHC [65] working group to take the envelope of the PDF uncertainty as the total PDF error $\Delta_{\mathrm{PDF}}^{\mathrm{total}}$ and symmetrize it afterwards, following:

$$\begin{aligned}\Delta_{\mathrm{PDF}}^{\mathrm{total}} = \frac{1}{2}\{&\max[\Delta\sigma^{\mathrm{CT10}}(\alpha_s+\mathrm{PDF},+),\sigma^{\mathrm{MSTW2008}}(\alpha_s+\mathrm{PDF},+),\sigma^{\mathrm{NNPDF\ 2.1}}(\alpha_s+\mathrm{PDF})]\\ &-\min[\Delta\sigma^{\mathrm{CT10}}(\alpha_s+\mathrm{PDF},-),\sigma^{\mathrm{MSTW2008}}(\alpha_s+\mathrm{PDF},-),\sigma^{\mathrm{NNPDF\ 2.1}}(\alpha_s+\mathrm{PDF})]\}\end{aligned} \tag{4.12}$$

The results of the PDF uncertainty calculations for the W' signal samples, following the above recipe, are summarized in figure 4.7 and table A.1 in the appendix. One can see that the uncertainty envelope is mainly contributed by CT10. Up to higher W' masses, the uncertainty rises due to a higher uncertainty in the PDF functions because of limited data in the high-energy regime and extrapolation errors for high Q^2. For W' masses greater than 2.6 TeV, the uncertainty is decreasing. This is caused by the increasing off-shell production of the W' due to the fact that the center-of-mass energy is not high enough anymore to produce it on-shell. At highest masses, the relative uncertainty reaches $\Delta_{\mathrm{PDF}}^{\mathrm{total}} = 8.5\%$ for $M_{W'} = 2.6$ TeV.

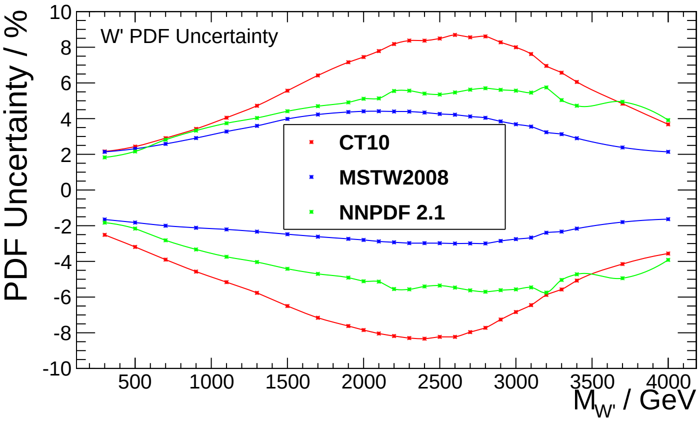

Figure 4.7.: PDF uncertainties on the W' signal cross sections. The uncertainty due to CT10 is making up the total uncertainty envelope except for very high W' masses.

4.4.1. PDFs for Contact Interaction

Since the contact interaction samples are produced together with the W, the uncertainty on the event number of pure contact interaction due to PDF uncertainty is not easily computed. A naive ansatz would be to compute the uncertainty on the W+CI sample and the W-only sample separately and propagate the uncertainties on the cross-section

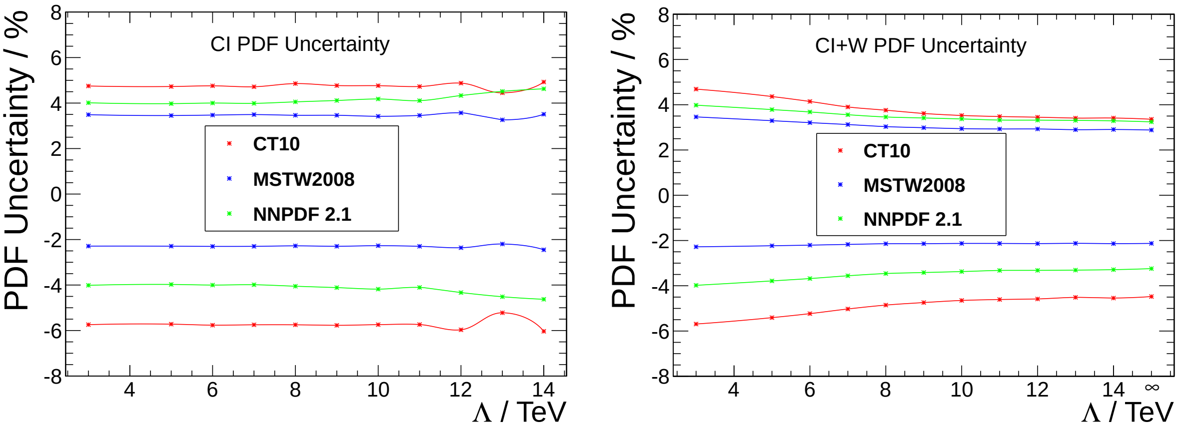

(a) The invariant mass distribution.

(b) The transverse mass distribution.

Figure 4.8.: PDF uncertainties on the CI cross section of (a) CI only and (b) W+CI. In figure (a) the uncertainty is relatively flat due to the fact that the shape of the contact interaction does not differ for different energy scales Λ. In figure (b) one can see that the uncertainty is decreasing with Λ because of the the smaller fraction at higher energies due to the decreasing contact interaction cross section. The limited statistics for high Λ are visible at the uncertainty band of CT10 at $\Lambda = 13$ TeV.

difference

$$\sigma_{CI} = \sigma_{W+CI} - \sigma_W \tag{4.13}$$

in a Gaussian manner. Since the correlation between the uncertainties on σ_{W+CI} and σ_W is not known, this is not a valid option. To avoid correlations, the uncertainty calculation, described before, has been modified. For the Hessian approaches, the formulae 4.7 - 4.10 are also used, but as the input, instead of a single cross section $\sigma^{(i)}$, the cross-section difference $\sigma^{(i)}_{CI+W}$ was inserted following equation 4.13. For NNPDF, formula 4.11 is adjusted analogously.

The results for the contact interaction cross-section uncertainty can be seen in table A.2 in the appendix and figure 4.8a. One can see that the uncertainty is flat in Λ. This is due to the fact that the shape of the contact interaction does not differ for different energy scales Λ. Therefore, the adjustment seems to work correctly. In figure 4.8b the uncertainty for the W+CI samples is displayed for comparison. One can see that the latter is not flat in Λ, but decreasing due to the decreasing cross section of Λ with respect to the W which is rather produced at lower center-of-mass energies.

5. Dataset and Standard Model Backgrounds

In this chapter the dataset, which the analysis is based upon, as well as the simulated samples, which are used for background estimation, are summarized and described.

5.1. Considered Data Sample

For this thesis 2012 proton-proton collision data at a center-of-mass energy of $\sqrt{s} = 8$ TeV from the CMS experiment, recorded from April the 4th to September the 5th, have been analyzed. In figure 5.1 the recorded integrated luminosity of the CMS detector is displayed.

According to luminosity measurements [72] with the hadron forward detector the considered dataset corresponds to an integrated luminosity of (10.3 ± 0.5) fb^{-1}. In this analysis only data is used which is certified by the DQM[1] group [73], which requires that all detector components have been switched on and were functioning. In order to organize the sheer amount of data, system of order is used, dividing the data in different *runs*. Each run is then divided into luminosity sections (*lumi sections*) that contain the collision *events* which are consecutively numbered. The DQM provides the information, which run and luminosity section is marked as good and should be used, in JSON[2] files. The following JSON files have been considered in this thesis:

- *Cert_190456-202016_8TeV_PromptReco_Collisions12_JSON.txt*
- *Cert_190456-196531_8TeV_13Jul2012ReReco_Collisions12_JSON.txt*
- *Cert_190782-190949_8TeV_06Aug2012ReReco_Collisions12_JSON.txt*

The first two numbers denote the runs that are covered by the JSON file. The term "ReReco" corresponds to a change in the events reconstruction algorithms, mainly due to problems with the ECal energy measurement, which made it necessary to redo the event reconstruction.

Concerning the one muon signal signature the *HLT_Mu40eta2p1*-trigger has been chosen which is a single muon trigger requiring an event to contain at least one muon with a transverse momentum of at least 40 GeV within the acceptance of the detector. The

---

[1] Data Quality Management

[2] JavaScript Object Notation. Text files containing the accepted luminosity section ranges of every run.

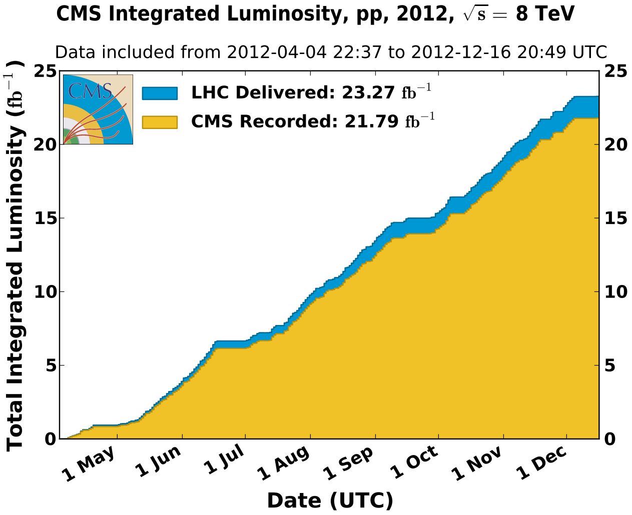

Figure 5.1.: The recorded and delivered integrated luminosity as a function of time. About 95 % of the provided integrated luminosity (”delivered”) have been recorded. From reference [39].

complete 2012 dataset is divided[3] into three sub-datasets, *RunA*, *RunB* and *RunC* corresponding to different integrated luminosities as shown in table 5.1

Dataset	Trigger	Run Range	L(pb^{-1})
/SingleMu/Run2012A-recover-06Aug2012/AOD	HLT_Mu40_eta2p1	190782-190949	82
/SingleMu/Run2012A-13Jul2012-v1/AOD	HLT_Mu40_eta2p1	190645-193621	700
/SingleMu/Run2012B-13Jul2012-v1/AOD	HLT_Mu40_eta2p1	193834-196199	4400
/SingleMu/Run2012C-PromptReco-v1/AOD	HLT_Mu40_eta2p1	198049-198522	490
/SingleMu/Run2012C-PromptReco-v2/AOD	HLT_Mu40_eta2p1	198941-202016	4700
		190782-202016	10300

Table 5.1.: List of the datasets used in the analysis and the corresponding run ranges.

5.2. Standard Model Background

The standard-model background is estimated with the help of simulation of all standard-model processes which are predicted to mimic a signal, either by producing the same physics signature or due to mis-reconstruction. The background samples are produced with Pythia 6 [24] in LO, if not stated otherwise. Since some processes are known to be simulated more accurately in other generators, also Madgraph [74] and Powheg [75] samples are used.

Since the instantaneous luminosity increased with respect to the early runs in 2010,

---

[3] Retrieved 2012-09-05

multiple occurrence of pp-events per bunch crossing plays an important role and has to be simulated, accordingly. The background samples used in this analysis have been simulated with two different pileup scenarios; for further details see table A.3 in the appendix and section 7.1 about pileup. The considered processes are summarized and explained in the following.

- **W** $\rightarrow \mu\nu$
  The main background for a search for W', but also for contact interaction, is the standard model W decaying to a muon and a muon neutrino. Since it produces exactly the same final state, it is an irreducible background. While the majority of W bosons are produced near the mass resonance at 80 GeV, very heavy off-shell W bosons contaminate the signal region at high M_T. Since this background cannot be suppressed, it has to be described accurately via Monte Carlo, also for high M_T, where ordinary W samples run out of statistics. This can be seen by comparing the total NLO $W \rightarrow \mu\nu$ cross section of 12086 pb with the W cross section of producing muons with a p_T greater than 500 GeV, which is about 2 fb. With the typical event count of a multi-jet Monte-Carlo sample of the order of 10 million, there is a high chance of having not a single simulated event with a p_T^μ above 500 GeV. In order to account for that two special W samples have been produced, additionally to the W standard sample, one for 100 GeV$< p_T^\mu <$500 GeV and one with 500 GeV$< p_T^\mu$.
  Since it is the most important background, an electroweak+QCD NLO correction binned in $\mathrm{M_T}$ has been calculated for the W to account for higher-order corrections, even at high M_T. This is described in section 5.2.1.

- **W** $\rightarrow \tau\nu$
  A W decaying into a τ lepton and neutrino can also contribute to the background, since the τ decays inside the detector and can decay into a muon and two neutrinos, therefore producing the sought signature. However, the emerging muon would be much softer. Since the tau comes from a secondary vertex, most muons coming from a high-energy tau decay can be rejected. The $W \rightarrow \tau\nu$ process has also been simulated with three different samples (with the same binning as above), because it is the main background for the $W' \rightarrow \tau\nu$ search.

- **Z**$/\gamma* \rightarrow \ell\ell$
  The Drell-Yan process describes the production of fermion pairs (in this case, lepton pairs) via $Z/\gamma*$ at hadron colliders. Via Drell-Yan, high-energy muons can be produced. Since they come in pairs, one has in principle a good method of rejecting them. But, if one muon leaves the detector undetected, because it misses the acceptance, the single muon signature as well as the corresponding MET are produced. For the $Z/\gamma* \rightarrow \mu\mu$ sample five additional Monte-Carlo samples, binned in the invariant mass M_{inv}, are provided, while the $Z/\gamma* \rightarrow \tau\tau$ sample is accompanied by four tails.

- **Multi-jet background**
  At LHC, hadrons are collided, therefore processes mediated by the strong interac-

tion play an important role. Even if a high-energy muon is faked by a jet only in very rare cases, the enormous cross section gives rise to non-negligible background contribution. Because NLO-calcuations in the strong coupling for QCD processes are not possible, only the LO prediction is available. Due to this and the fact that the high cross section does not allow MC production with sufficient event counts, an estimate of the Multi-jet contribution to the final $\mathrm{M_T}$ distribution is done for cross checks and explained in 7.2. Eleven multi-jet distributions have been generated with a binning in the scale of the hard interaction. These so called muon-enriched samples are produced with an additional filter that rejects all events which do not contain one muon with a p_T of at least 5 GeV.

- **Top-pair and single-top production**
  The high $\sqrt{s}$ at LHC also allows top production. Since top quarks always decay via weak interaction into a bottom quark, a boosted W is produced, decaying into a high-energetic muon and therefore potentially producing one part of the sought signature, in about 10% of the top decays [76]. The $t\bar{t}$ sample considered is generated with Madgraph in LO, while the single-top samples are produced with The NLO generator Powheg. All samples are produced with the underlying PDF set CTEQ6L1, except the single-top samples which are produced with CT10.

- **$\mathbf{WW}, \mathbf{WZ}, \mathbf{ZZ}$**
  Diboson events, containing either the production of $W^+ + W^-$, Z pairs or $W + Z$, are also taken into account, because from a bosonic decay a muon can emerge. Each diboson sample comes with an additional sample generated for $p_T^{W,Z} > 500$ GeV.

5.2.1. NLO corrections to the W Background

Since the process $W \to \mu\nu$ is the main background, it is necessary to have a precise description of it, especially at higher energies, where the sensitivity to the signal is best. To account for higher order corrections, a flat NNLO k-factor of 1.32 is applied, which is the ratio of the total $W \to \mu\nu$ NNLO and LO cross section. But due to the fact that, as shown before, the cross section in the regime of interest ($M_T > 500$ GeV) is several orders of magnitude lower than at the W peak, this k-faktor is not necessarily a good description everywhere. In fact, especially electroweak higher-order corrections, which are negligible at $M_T < 500$ GeV are expected to have a sizeable impact of the order of up to 30% [77] for $M_{\mathrm{inv}} = 2000$ GeV. The significant change of the k-factor also leads to a change of shape in the M_T spectrum. Therefore, higher order corrections have been calculated binned in $\mathrm{M_T}$ up to 2.5 TeV in 10 GeV steps. QCD and electroweak corrections had to be calculated separately, because they are not implemented in the same generator. Electroweak corrections have been estimated with Horace [78] and QCD corrections with MC@NLO [79] by Mark Olschewski [80]. Since for the analysis the W samples have been produced with Pythia 6 at LO with the PDF set CTEQ6L1 and Horace and MC@NLO both use CT10, also a Pythia 6 sample with CT10 is needed to account for the influence of the PDF set. In figures 5.2 the cross-section difference for all the considered generators is displayed. It can be seen that the QCD k-factor

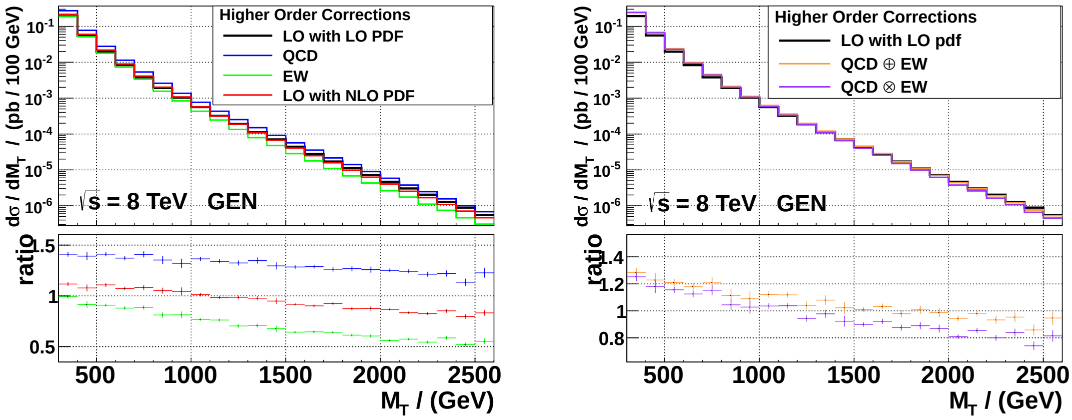

(a) (b)

Figure 5.2.: (a) A comparison of the cross section estimated by different generators as a function of M_T. The term QCD (b) A comparison of the two methods combining the EW and QCD corrections. QCD $\oplus$ EW and QCD $\otimes$ EW represent the the k-factor-combination methods corresponding to k_1 and k_2, respectively.
In both plots LO denotes the cross-section calculation with Pythia 6, while QCD stands for the NLO correction in α_s and EW for the electroweak NLO correction. Both plots are made by Mark Olschewski [80].

(blue) is relatively flat, with a slight decrease down to 1.25. However, the EW k-factor shows a strong decrease down to values around 0.5, therefore the electroweak corrections contribute destructively.

In order to get a total k-factor to scale the Pythia 6 standard samples to get a description as close as possible to nature, one has to combine all corrections. Two approaches for the combination are shown to be reasonable [81], depending on how correlated both corrections are estimated, see equation 5.1. For the actual reweighting of the LO W distribution, the mean of k_1 and k_2 is taken as an approximation.

$$k_1 = \frac{\sigma_{\text{QCD}} + \sigma_{\text{EW}} - \sigma_{\text{Py, CT10}}}{\sigma_{\text{Py,CTEQ6L1}}}; \quad k_2 = \frac{\sigma_{\text{QCD}} \cdot \sigma_{\text{EW}} / \sigma_{\text{Py, CT10}}}{\sigma_{\text{Py,CTEQ6L1}}} \tag{5.1}$$

In order to get a continuous k-factor, a fit is applied (see figure 5.3) in the range where the binned k-factor was calculated. A third degree polynomial has proven to be the best parametrization in the region of interest. As shown in [81], additional NNLO corrections would be relatively small for the energies of interest in this analysis and are therefore neglected.

For lower values of M_T than 200 GeV, the flat NNLO k-factor of 1.322 is taken, which agrees within 6 permille with the k-factor from the parametrization at 200 GeV, thus a smooth transition is given.

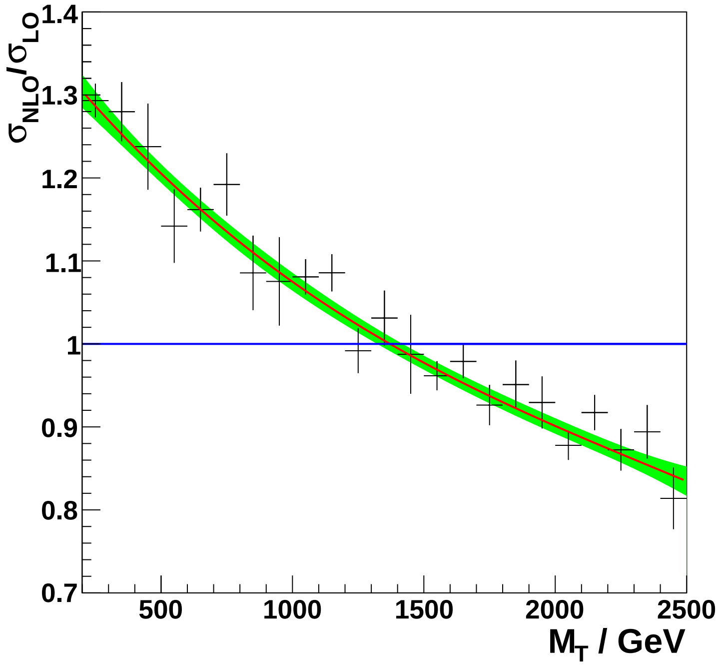

Figure 5.3.: Fit on the M_T binned k-factor $\sigma_{\text{NLO}}^{\text{QCD,EW}}/\sigma_{\text{LO}}$. The green band represents the parametrization uncertainty and is incorporated as systematic uncertainty in section 8.1.

6. Signal Selection

The following chapter is a description of the quality criteria and signal specific requirements that are applied during the event selection in order to suppress mis-identification and gain high signal sensitivity.

6.1. Quality Criteria

As stated in section 5.1, the considered data sample is triggered with a single muon trigger requiring at least one muon per event with a transverse momentum above 40 GeV inside the acceptance $|\eta| < 2.1$. In order to stay above the so called *trigger turn on* at p_T around the trigger threshold, which is not well simulated in the Monte Carlo, the chosen muon is required to carry a transverse momentum greater than 45 GeV. Therefore, the first three event quality requirements, so called *preselections*, are:

Preselection

- High level single muon trigger
- $|\eta| < 2.1$
- $p_T > 45$ GeV

For high-energy muon identification and momentum assignment the cocktail algorithm is the reconstructor of choice, as explained in section 3.1.4.
The following quality criteria correspond to the recommendation of the Muon Particle Object Group [82] for high-p_T muons with minimal adjustment concerning the impact parameter d_0 and the requirement of a tracker muon. They are needed to reject events with bad or mis-reconstructed muons as well as muons not coming from the primary interaction point.

6.1.1. Muon Quality Requirements

- The considered event has to contain a muon that is both a global and a tracker muon, i.e. both reconstruction algorithms, the outside-in and the inside-out (see section 3.1.3) have to agree on the muon identification. This is a first step to ensure a sufficient number of hits in tracker and muon system. The global muon requirement is also natural, since it is a precondition of all cocktail muons. The tracker muon requirement is additional and not part of the official recommendation.

Requirements on hits in the muon detector

- At least one muon chamber hit has to be included in the global muon track fit. This selection is made to suppress hadronic punch-trough and muons from decays in flight. A punch-trough is an high-energetic hadron that possibly enters the muon system and gets eventually absorbed by the iron joke after passing one chamber. Decays-in-flight are processes in which a muon comes from a secondary decay, e.g. from a tau lepton or b quark.
- At least in two muon stations there have to be track segments. This is also a veto against punch-trough, since it is unlikely that the hadronic shower passes the iron yoke. This selection also maintains consistency with the muon trigger logic that also requires at least two stations with segments for a meaningful estimate of the transverse momentum.

Requirements on hits in the tracker

- The number of pixel hit in the vertex detector is required to be greater than zero. This further suppresses muons from decays in flight, since they could be produced outside the innermost part of the detector. A hit in the pixel detector is furthermore a requirement to reconstruct a primary vertex with sufficient precision.
- In order to allow for a reliable p_T measurement with the tracker, a minimal number of hits is necessary. Therefore, a total number of at least nine tracker layers hit by the muon is required in this analysis. For low-p_T muons, this selection step is looser, only six hits are required. It is tightened for high-p_T muons, because their trajectories are much less bent and more hits are needed to estimate the curvature. Furthermore, the rate of mis-identification of other particles as muons is decreased.

Since an update in the tracking algorithm in CMSSW52X [56], the requirement of nine hit tracker layers as applied in this thesis introduces a reconstruction efficiency loss of up to 5 % [82].

In order to reduce this inefficiency, an improved replacement for this important selection has been searched, which provides a comparable rejection of mis-reconstructed muons. The muon object group considered a replacement, where the number of hit layers is lowered back to at least 6 and it is considered to additionally demand a relative p_T uncertainty lower than 0.3. However, this new requirement is not included in the event selection of this analysis, because it is only recommended for a newly adapted cocktail muon momentum assignment logic based on the relative p_T uncertainty which is optimized for the new selection [82].

This new selection was also investigated in the Bachelor Thesis of Tim Poljansek [83]. In figure 6.1, the relation between the relative p_T uncertainty and the number of hit tracker layers is shown. It can be seen that well-reconstructed muons (with low $\Delta p_T/p_T$) are rejected, if $n_{\text{layers}} > 8$ is required. Since the mid of November, the new selection has been included in the official recommendation for high-p_T muons.

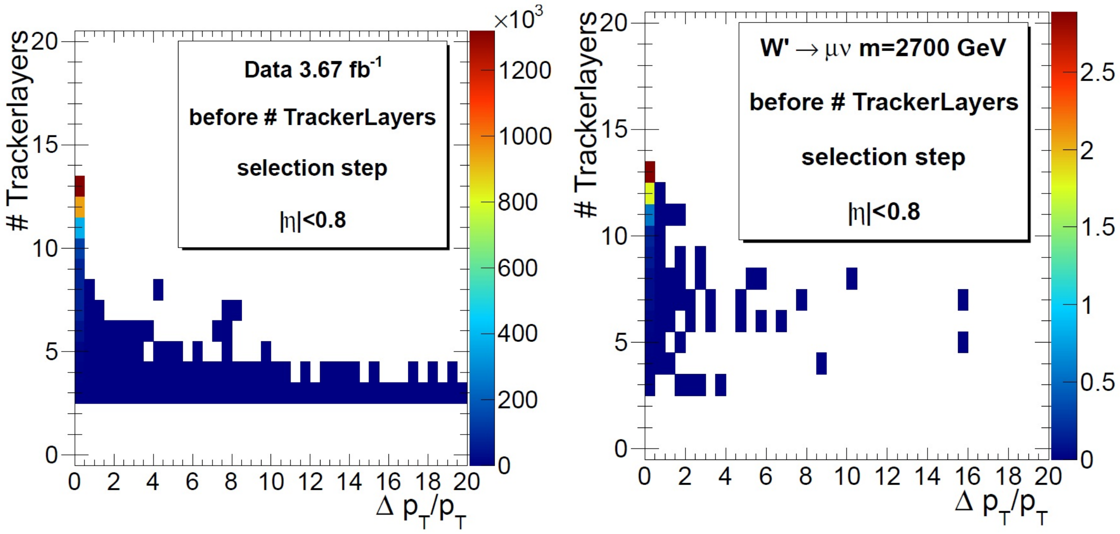

(a) (b)

Figure 6.1.: The relative uncertainty on p_T with respect to the number of hit tracker layers for (a) the data and (b) a W' signal sample. From reference [83].

Requirements on the Impact Parameter

Every event considered in this analysis has to have at least one well-reconstructed primary vertex corresponding to the hard interaction. Here, a well-reconstructed primary vertex is required to have at least four tracks associated, a maximal distance in the longitudinal direction of 24 cm and a small probability of the vertex being faked. If a high-energy muon is considered to be produced via W' decay or contact interaction, it should originate from the primary vertex and not from any secondary process. Therefore, a primary vertex matching is done by applying the following two criteria.

- The longitudinal distance between tracker track and primary vertex is required to be less than 5 mm. This criterion also suppresses events containing a cosmic muon traversing the detector during a bunch crossing and faking a signal. Also pileup-caused signal-like events can be rejected with the vertex restriction.

- Similar, only muons are considered, whose so called transverse impact parameter d_0 is less than 0.02 cm. d_0 is the minimal distance of the extrapolated muon track in the transverse plane with respect to the primary vertex. The original threshold lies at 2 mm, but is very loose and can be tightened further to suppress cosmic muons. Earlier studies [25] have shown that the tightening of the order of one magnitude lowers the signal efficiency by less than 1 %. This is still true as can be seen in figure 6.2. Almost all signal events lie in the first two bins corresponding to a d_0 of less than 0.02 cm. It can be seen that large fractions of QCD events are rejected by this requirement.

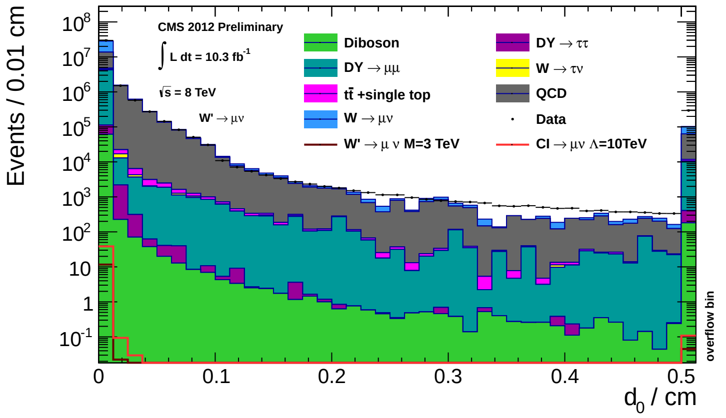

Figure 6.2.: Distribution of the transverse impact parameter d_0 of the leading muon. Both signals are accumulated in the first two bins, fulfilling $d_0 < 0.02$ cm.

Muon Isolation

- The muons originating from a jet are expected to be not isolated, but surrounded by many other entries in the tracker, caused by the multiple charged hadrons the jet consists of. Since a muon from a signal event in principle should not be accompanied by a significant amount of other particles, the muon isolation gives rise to another selection criterion. However, the TeV muons which are basis of this analysis have a significant probability to emit bremsstrahlung and therefore being not isolated, anymore. Also, the high pileup conditions (see section 7.1) can lead to a decrease in isolation. Thus, a relatively loose isolation criterion is applied following the official recommendations [82] and using the relative track information of the tracker.
  At first, a cone with size $\Delta R < 0.3$ is defined in the $\eta - \phi$ space around the muon trajectory vector via $\Delta R = \sqrt{(\Delta\phi)^2 + (\Delta\eta)^2}$. The transverse momenta of all particles reconstructed inside the cone are now summed up. The ratio of the sum and the transverse muon momentum is required to be less than 0.1, in formula:

$$\mathrm{Iso}_{\mathrm{rel}}^{trk} = \frac{\sum_{\Delta R<0.3, i\neq\mu} p_T^{\mathrm{track}\ i}}{p_T^{\mu}} \tag{6.1}$$

  As shown in figure 6.3, more than 99 % of the signal events are nicely isolated and are located in the first bin, therefore a cut at 0.1 retains a high signal efficiency.

6.2. Signal-Specific Selection

Beside the quality criteria, there are three additional requirements applied to yield a better signal-to-background ratio. The first one is a simple veto against events con-

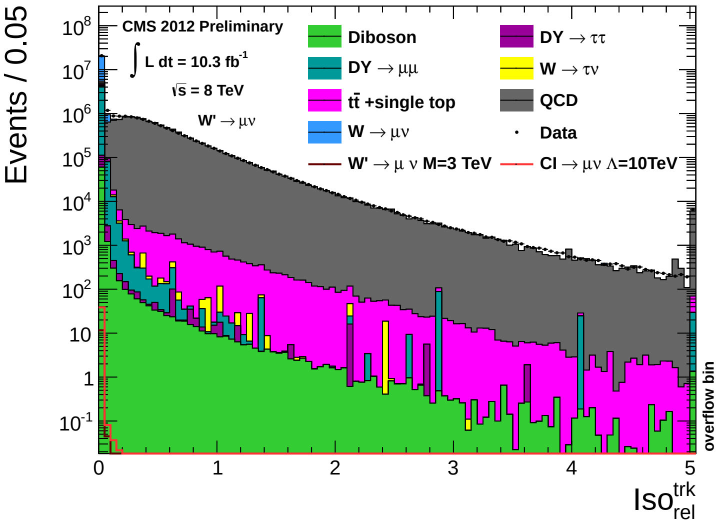

Figure 6.3.: Distribution of the relative tracker isolation of the leading muon. Most events are isolated and lie in the first bin corresponding to an isolation of 0.05.

taining an additional global muon with a $p_T > 25$ GeV, beside the leading muon with $p_T > 45$ GeV. This rejects events with two muons coming from a Drell-Yan process as well as a cosmic muon which is accidentally identified as two muons. The other two selections are exploiting the two-body kinematics of the W' decay and the contact interaction and have already been established in previous searches [84, 85, 86].

Ratio of p_T^μ and MET

As stated in section 4.2.2, W' production, as well as the contact interaction, corresponds to a relatively high $\sqrt{\hat{s}}$. The center-of-mass system of the signal process has low transverse momentum, which could only come from hadronic recoil (see section 7.4) due to the negligible p_T in the initial state. Since only two particles, i.e. the muon and the neutrino are produced, there transverse momenta p_T^μ and p_T^ν should be balanced, even in the detector frame. As shown before, p_T^ν is indirectly determined via MET measurement. Thus, the ratio of the signal p_T^μ and MET should be peaking at one, being washed out mainly by the detector resolution, the pile-up and possibly by hadronic recoil. This behaviour can be seen in figure 6.4 and allows for a new criterion, with thresholds optimized in another thesis [86]:

$$0.4 < \frac{p_T^\mu}{\mathrm{MET}} < 1.5 \tag{6.2}$$

Polar Angle between p_T^μ and MET

Additionally, a geometrical selection criterion emerges from the back-to-back kinematics

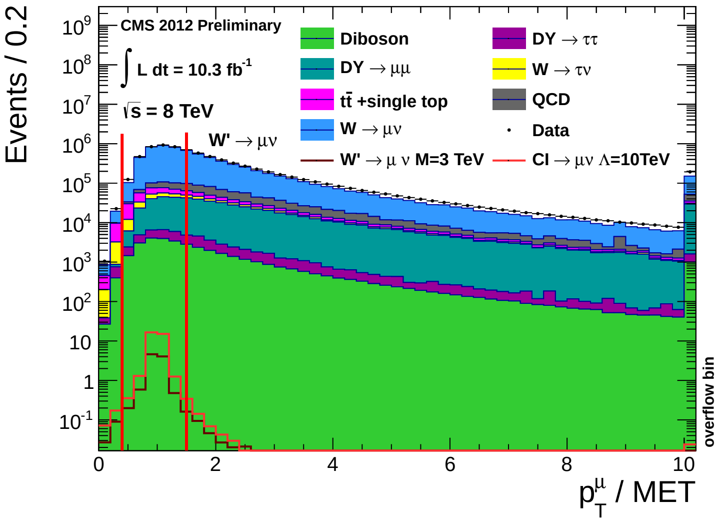

Figure 6.4.: Distribution of the ratio p_T^μ/MET after applying all quality selections and requiring that no second muon with $p_T > 20$ GeV beside the leading muon with $p_T > 20$ GeV is in the event. The mismatch between data and simulation for high values of p_T^μ/MET is caused by the inadequate simulation of the production of more than one jet along with the W production in Pythia 6 simulation [87].

of the two-body final state. The directions of motion of muon and neutrino are exactly opposite in the center-of-mass frame, but since its boost in z direction is unknown and possibly high, the spatial angle between muon and neutrino can be reduced to lower values than π in the lab frame. But the polar angle $\Delta\phi(\ p_T^\mu, \mathrm{MET}\ )$ in between both is invariant under boost in z and can therefore be used as a further event selection criterion:

$$\Delta\phi(\ p_T^\mu, \mathrm{MET}\ ) > 2.5 \tag{6.3}$$

The distribution of $\Delta\phi(\ p_T^\mu, \mathrm{MET}\ )$ is displayed in figure 6.5.

A summary of all selections is given in table 6.1. The influence of the selection on the background is summarized in table 6.2. For the considered signals see table A.4 in the appendix. It is shown that the background is strongly suppressed by the selection while the signals stay at a relatively high efficiency. The W' signal efficiency increases up to about 70 % for heavy on-shell W', but decreases for higher masses due to an increasing fraction of muons with $p_T < 45$ GeV in the off-shell tail. The higher signal efficiency for contact interaction at 77 % is caused by the generator threshold of $\hat{p}_T > 300$ GeV. After performing the complete event selection, the sensitivity on possible signals is increased drastically. The impact of the selection can be seen nicely in the p_T-distribution of the leading muon in every event. A comparison between the spectrum without any quality and selection-specific criterion applied and the spectrum after the full selection is given in figure 6.6. The signal-to-background ratio has been improved significantly by about 5 orders of magnitude for a W' with a mass of 1.3 TeV.

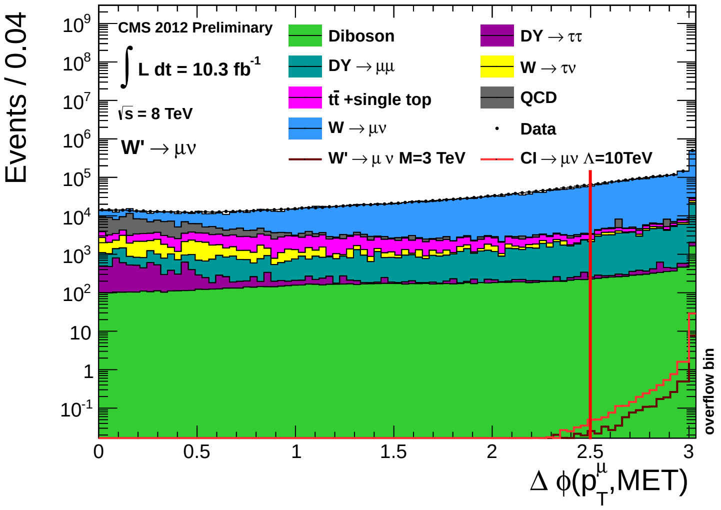

Figure 6.5.: Distribution of the difference in the polar angle $\Delta\phi$ between the muon and MET after applying all quality and signal-specific selections.

Selection Criterion	Quantitative Requirement
Preselection	
Trigger matching	-
p_T	>45 GeV
$\lvert\eta\rvert$	<2.1
Quality Criteria	
Global & Tracker muon	-
Rel. Track Iso.	< 0.1
Hit Tracker layers	> 8
Hits in Muon system	> 0
Matched Muon stations	> 1
Hits in pixel Detector	> 0
Transv. Impact Parameter d_0	> 0.02 mm
Longit. Impact Parameter d_z	> 5 mm
Signal-Specific Selection	
No second muon	$p_T > 20$ GeV
p_T^{μ}/MET	$[0.4, 1.5]$
$\Delta\phi(\mu$/MET)	> 2.5

Table 6.1.: Summary of all criteria applied in the event selection. The table is divided into preselection, quality criteria and signal specific selections. All quantities refer to the selected muon, except the MET.

Background	No Selection	*Preselection*	Quality Selection & only 1 μ	p_T^μ/MET	$\Delta\phi(p_T^\mu$,MET)
$W \rightarrow \mu\nu$	$1.25{\cdot}10^8$ 100%	$6.97{\cdot}10^6$ 5.59% 5.59%	$6.22{\cdot}10^6$ 4.98% 89.2%	$3.00{\cdot}10^6$ 2.40% 48.2%	$1.66{\cdot}10^6$ 1.33% 55.2%
$DY \rightarrow \mu\mu$	$1.99{\cdot}10^7$ 100%	$2.82{\cdot}10^7$ 14.2% 14.2%	562000 2.82% 19.9%	128000 0.640% 22.7%	72000 0.361% 2.40%
QCD	$1.39{\cdot}10^9$ 100%	$9.90{\cdot}10^6$ 0.712% 0.712%	433000 0.0311% 4.37%	128000 0.009% 29.6%	12400 >0.001% 9.66%
Diboson	$1.01{\cdot}10^6$ 100%	50800 5.04% 5.04%	382000 3.78% 75.1%	173000 1.71% 45.2%	6090 0.604% 35.3%
$W \rightarrow \tau\nu$	$1.25{\cdot}10^8$ 100%	116000 0.0928% 0.0928%	103000 0.0827% 89.1%	48300 0.0387% 46.8%	8500 0.00681% 17.6%
$t\bar{t}$ & single top	$3.50{\cdot}10^6$ 100%	277000 7.89% 7.89%	207000 5.92% 75.0%	109000 3.10% 52.38%	15800 0.451% 14.6%
$DY \rightarrow \tau\tau$	$2.02{\cdot}10^7$ 100%	31700 0.157% 0.157%	27400 0.135% 86.3%	9930 0.0491% 36.3%	1560 0.00771% 15.7%
All backgrounds	$1.68{\cdot}10^9$ 100%	$4.56{\cdot}10^7$ 2.71% 2.71%	$7.94{\cdot}10^6$ 0.473% 17.4%	$3.60{\cdot}10^6$ 0.214% 45.3%	$1.78{\cdot}10^6$ 0.106% 49.4%
Data	-	$5.35{\cdot}10^7$	$9.23{\cdot}10^6$	$3.93{\cdot}10^6$	$1.89{\cdot}10^6$

Table 6.2.: Selection efficiencies and predicted event counts according to $\mathcal{L}_{\text{int}} = 10.3\ \text{fb}^{-1}$ for all backgrounds and data of the analysis. The left percentage corresponds to the remaining events relative to the event number before all selections. The right percentage denotes the efficiency relative to the selection stage given before. The discrepancy between simulation and data is about 20 % after the selection, which is mainly due to the limited QCD simulation. Since QCD gets strongly suppressed by the applied selections, the agreement improves with every selection step. The final discrepancy of 7 % is mainly due to a mismatch in the low p_T region between simulation and data. In the next section is shown that this mismatch disappears for higher p_T and M_T, respectively and does not play a role for this analysis.

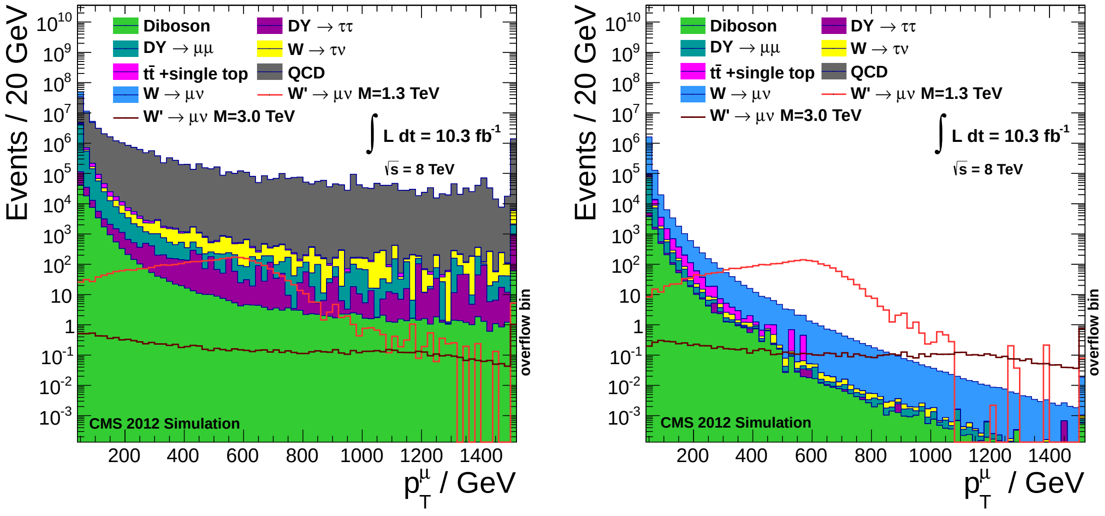

(a) (b)

Figure 6.6.: The distribution of the transverse momentum of the leading muon with (a) no quality and signal-specific selection and (b) after all selection steps.

7. The Final Transverse Mass Distribution

The p_T and MET spectra are shown in figure 7.1. A rebinning is chosen to account for the decreasing resolution of the muon p_T for high momenta.

The final distribution which is scanned for signal-like deviations from the standard model is the transverse mass distribution. As shown in the last chapter, the quality requirements and signal-specific selections lead to a nice suppression of backgrounds in the signal region of high $\mathrm{M_T}$. Before the final statistics-based analysis is started, some final adjustments are applied to the background and an estimation of the multi-jet contribution is performed.

7.1. Pileup Reweighting

The high instantaneous luminosity of around 6-7 Hz/nb (see figure 7.3a) causes a relatively high number of collisions per bunch crossing, leading to an overlap of different events, which is called pileup. As shown in figure 7.4, the average number of interactions per bunch crossing lies at about 18 in 2012 data, but also events with a much higher number of reconstructed vertices are observed as exemplarily displayed in figure 7.3b. The pileup causes a high occupancy of the detector and complicates the event reconstruction significantly, e.g. afflicting the isolation of tracks. Beside the so called in-time pileup, as explained before, pileup is also caused by the small time spacing of only 50 ns between two bunch crossings. The latency of some detector parts, primarily the hadronic calorimeter [40], lie in the same order of magnitude as the bunch spacing which can lead to migration of measurements that correspond to a preceding or following bunch crossing. This is called out-of-time pileup.

All considered Monte Carlo samples have been generated in the official production campaign of early 2012, which also includes a simulation of pileup. Since the pileup conditions have been not exactly known when the first samples have been generated with CMSSW 52X, the number of interactions was overestimated by a factor of about 2, see figure 7.4. In order to account for that the Monte Carlo samples are adjusted to the measured pileup in data by assigning weights to every simulated event. The weights are calculated by comparing the frequency of both in-time and out-of-time pileup in data and simulation. The reweighting for the analysis has been performed using the official pileup reweighting tool provided by [88].

Since the average number of vertices was overestimated, most of the simulated events are given a rather low weight, while few get very high ones. Even if the normalization is not affected by the reweighting, this effectively results in a significant loss of information. Therefore, another production campaign in CMSSW 53X was executed using the

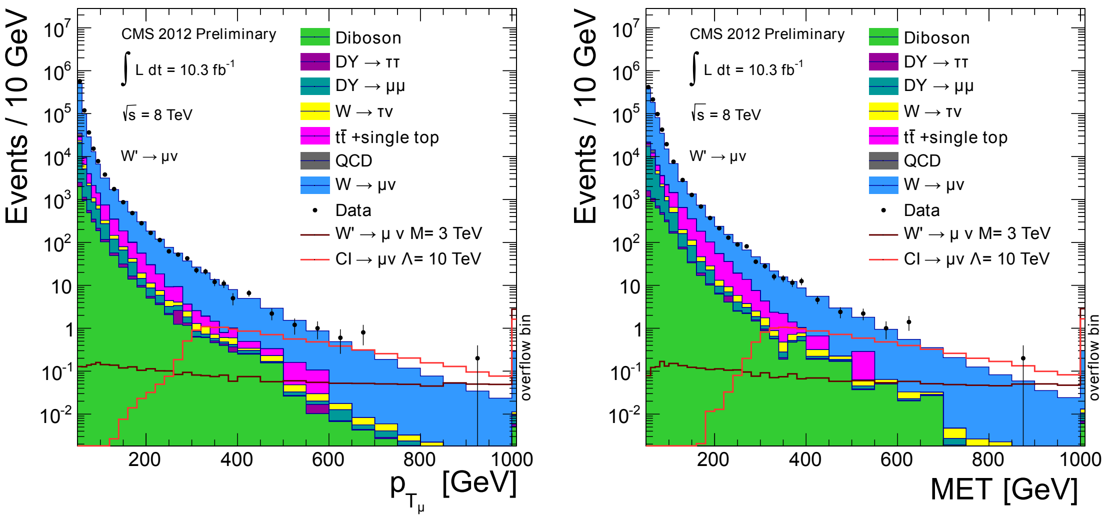

(a) (b)

Figure 7.1.: The muon p_T (a) and MET (b) distribution after applying all selection criteria.

production on matrix element level and detector simulation as in the previous production chain, but with adapted pileup and a new reconstruction simulation. Since some samples have not been available from the new production at the time of this analysis (see table A.3), the background samples are partly from the first production and are therefore assigned with different weights. All signal samples as well as the $W \to \mu\nu$ background are from the 53X generation and thus utilize the provided statistics efficiently. The vertex distribution in data and simulation before and after the reweighting is displayed in figure 7.2 showing a nice agreement afterwards.

7.2. Estimation of Multi-jet Background Contribution

The estimation of the contribution of QCD processes to the background via Monte Carlo samples is not as reliable as for the other standard model processes, since multi-jet events have much higher cross section, which is only known up to leading order. However, isolated high-p_T muons have a very low probability to be faked or produced by multi-jet events. In order to verify that multi-jet events do not contribute to higher masses than 500 GeV a data-driven cross-check was performed based on [25]. The method is divided into two parts; obtaining a normalization and a shape for the QCD prediction.

At first, an estimation of the normalization of QCD events is obtained by making use of the p_T/MET-distribution after applying all muon quality criteria, but before the kinematic selection. The method exploits that the p_T/MET-distribution is W-dominated at 1, but for higher values the influence of QCD increases, since QCD events typically contain relatively low MET. The normalization is yielded by taking the p_T/MET-

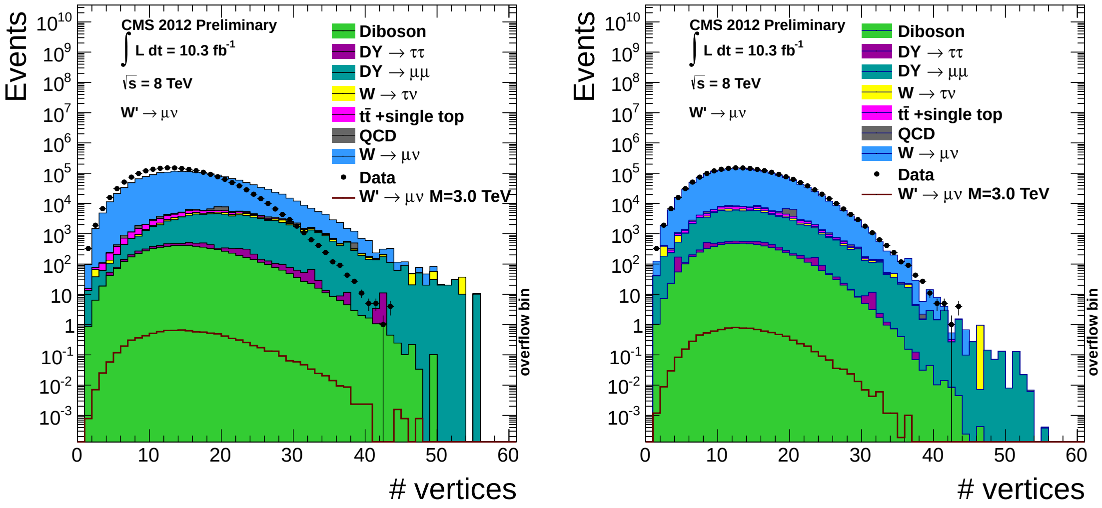

(a)

(b)

Figure 7.2.: The distribution of reconstructed vertices before (a) and after (b) the pileup reweighting. One can see that the agreement between data and simulation agrees well afterwards.

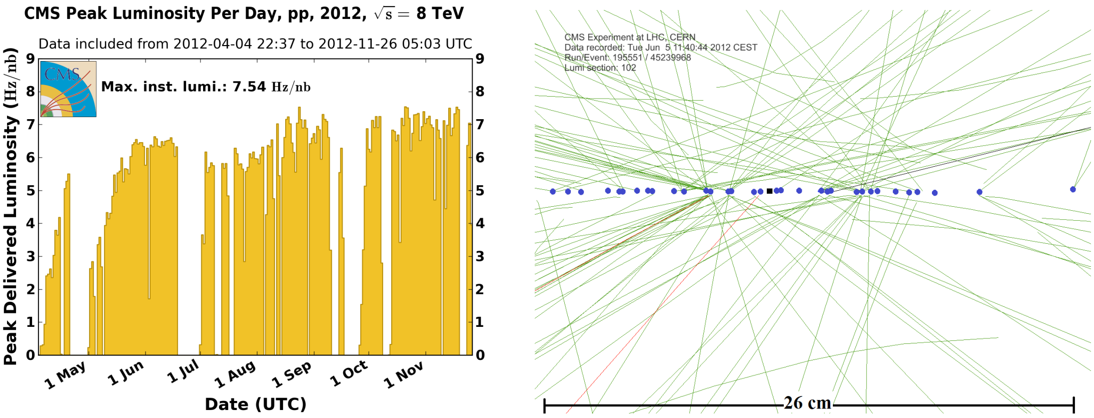

(a)

(b)

Figure 7.3.: (a) The maximal instantaneous luminosity per day at CMS in 2012. The average lies at about 6-7 Hz/nb. (b) A zoom inside an event display from data with 33 reconstructed vertices (blue dots) strung along the z axis and surrounding the beam spot (black rectangle). Tracks with a $p_T > 1.5$ GeV are shown in green and muons in red.

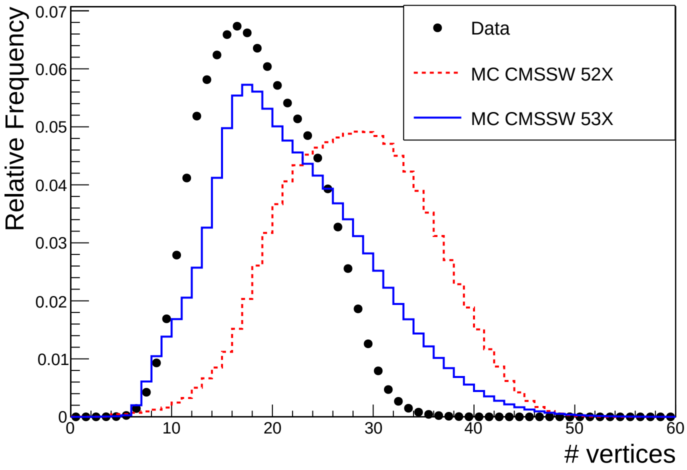

Figure 7.4.: The different pileup in data (dots) compared to the different scenarios in Monte Carlo 52X (dashed line) and 53X (solid line).

distribution from data and subtract all standard model backgrounds except W and QCD. Then a fit is applied on the supposition that the remaining data now only consists of W and QCD events. The W shape is found to be well-described by a Crystal Ball function [89]. For the QCD shape a template is taken from Monte Carlo simulation. The free fit parameters are the ones of the Crystal Ball function and the normalization of the QCD prediction. In figure 7.5a, the fit result (blue solid line), which is the sum of the W (red dashed line) and QCD (blue dashed line) prediction, is shown in comparison to data (black dots). For the QCD normalization one obtains $(1.1 \pm 0.1) \cdot 10^6$ QCD events from the fit after all quality selections and before the two last kinematic signal selections. The given uncertainty takes into account the fit uncertainty and the systematic uncertainties. This is about 2.5 times as much as predicted by simulation, see table 6.2. In order to yield the right normalization for the final M_T distribution, two additional scale factors have to be included as well, since the event count prediction from the p_T/MET-distribution does not include the two kinematic selections. The requirement on the p_T/MET ratio to be between 0.4 and 1.5 is only passed by about 30 % of simulated multi-jet events that have passed the muon quality criteria. Only about 10 % of the multi-jet events that passed the first kinematic selection do also fulfil the second step requiring the polar angle between MET and the muon to be greater than 2.5, cf table 6.2. Therefore, the QCD event count in the final transverse-mass distribution is predicted to be 33000.

In the second step, the shape of the transverse mass distribution of QCD is derived from data. All quality and kinematic selection criteria are applied except requiring the muons to be isolated. Instead, a relative track isolation above 0.25 is demanded. This ensures that the considered data sample is now multi-jet dominated, which can be seen in figure 6.3, and provides much higher statistics than the simulated sample. The non-

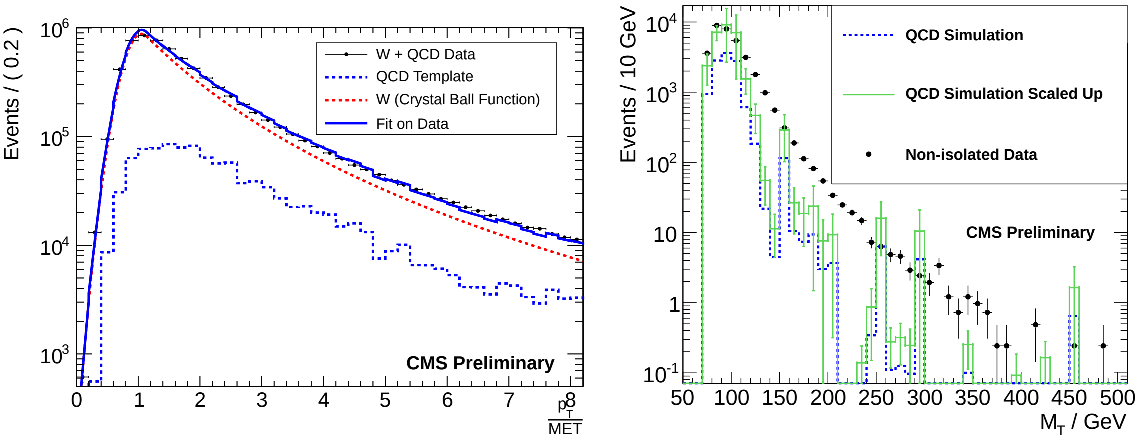

(a) (b)

Figure 7.5.: (a): A shape-based fit (blue line) of W (red dashed line) and multi-jet background (blue-dashed line) to the p_T/MET-distribution of data (black dots) after subtracting all other SM backgrounds. The QCD template is taken from simulation and its normalization is taken as a free fit parameter. (b): Comparison in the $\mathrm{M_T}$ -spectrum between the multi-jet Monte Carlo prediction (blue line) and the data-driven prediction (black dots) obtained from non-isolated events. The QCD prediction is scaled up by the factor 2.5 yielded from the fit to data in the p_T/MET-distribution. The scaled-up prediction (green solid line) is shown with statistical uncertainties, which are relatively high due to the lack of statistics in the QCD Monte-Carlo, which causes the high deficit in the simulation for $M_T > 120$ GeV with respect to the data-driven QCD estimation. The high QCD cross section causes the reweighting factor R (see eqn. 4.1) to be much greater than one leading to high fluctuations in the simulation. The data-driven approach, despite having much more statistics, does not predict QCD events above $M_T > 500$ GeV as well. Therefore, the QCD background can be neglected for this analysis.

isolated data is scaled down in order to fulfil the correct normalization, which has been previously estimated. The final data-driven multi-jet prediction is shown in figure 7.5b. There are no events predicted above a transverse mass of 500 GeV despite significantly higher statistics, therefore the QCD contribution is negligible for this analysis.

7.3. Efficiencies and Scale Factors

The simulation of the efficiency of the muon quality criteria and the trigger may differ from the actual efficiencies seen in data. This can lead to discrepancies between the event prediction and data. If one wants to take MC simulation as a reliable prediction those differences have to be taken into account.

In order to be able to compare reconstruction and trigger efficiencies the "Tag and Probe" method is applied [90]. It exploits the clean signature of the decay of the Z boson into two muons. If one muon, the tag muon, fulfils certain quality criteria, the event is scanned for other muon candidates. If the invariant mass of a candidate and the tag muon is in the Z mass resonance region, here defined as 70-130 GeV, the candidate muon is defined as the probe muon. Now, the requirement for which the efficiency needs to be calculated is applied on the probe muon. If it fulfils the criterion, it *passes*, if not, it *fails*. The efficiency of a requirement is then defined as the ratio of events containing a passing probe and all considered events, i.e.

$$\varepsilon = \frac{N_{\text{passed}}^{\text{probe}}}{N_{\text{passed}}^{\text{probe}} + N_{\text{failed}}^{\text{probe}}}. \tag{7.1}$$

The efficiencies used in this analysis are provided by the muon particle object group [91, 92]. As the requirement for a tag muon, the quality selection described in section 6.1.1 is taken along with a p_T greater than 20 GeV and a matching muon trigger.

The efficiencies considered in this analysis are the muon quality efficiency (also called muon ID efficiencies) ε_{ID} which takes into account all quality criteria from section 6.1.1 except the isolation, the muon isolation efficiency ε_{iso} and the muon trigger HLT_Mu40eta2p1 efficiency $\varepsilon_{\text{trigger}}$. Since the efficiencies are different for muons detected in the barrel and the endcap, they are provided with a binning in the pseudorapidity, discriminating between $0 < |\eta| \leq 0.9$, $0.9 < |\eta| \leq 1.2$ and $1.2 < |\eta| \leq 2.1$.

The efficiencies are estimated separately for RunA+RunB and for RunC (see table 5.1 for information about the runs). The important information derived from the efficiency measurements for this analysis is the comparison between data and simulation. Three scaling factors K_i are then calculated to account for the data-simulation discrepancy via

$$K_i = \frac{\mathcal{L}_{\text{AB}}^{\text{int}} \cdot \frac{\varepsilon_{\text{ID}}^{\text{AB}}}{\varepsilon_{\text{ID}}^{\text{sim}}} \cdot \frac{\varepsilon_{\text{trigger}}^{\text{AB}}}{\varepsilon_{\text{trigger}}^{\text{sim}}} \cdot \frac{\varepsilon_{\text{iso}}^{\text{AB}}}{\varepsilon_{\text{iso}}^{\text{sim}}} + \mathcal{L}_{\text{C}}^{\text{int}} \cdot \frac{\varepsilon_{\text{ID}}^{\text{C}}}{\varepsilon_{\text{ID}}^{\text{sim}}} \cdot \frac{\varepsilon_{\text{trigger}}^{\text{C}}}{\varepsilon_{\text{trigger}}^{\text{sim}}} \cdot \frac{\varepsilon_{\text{iso}}^{\text{C}}}{\varepsilon_{\text{iso}}^{\text{sim}}}}{\mathcal{L}_{\text{AB}}^{\text{int}} + \mathcal{L}_{\text{C}}^{\text{int}}}, \tag{7.2}$$

where $\mathcal{L}^{\text{int}}$ denotes the integrated luminosity and i represents one of the three considered regions in pseudorapidity. All simulated events are then weighted with K_i.

A summary of the yielded scaling factors K_i is given in table 7.1. One can see that the efficiencies in the transition region between barrel and endcap is simulated worst, with a discrepancy of more than 7 %. Since most muons in the high $\mathrm{M_T}$ region of interest carry large transverse momenta, they are predominantly traversing the detector in the barrel region, where the scaling factor lies at about 0.96. The largest contributions come from the ID and trigger scaling factors, which both vary between 0.96-0.99, while $\frac{\varepsilon_{\mathrm{iso}}^{\mathrm{AB}}}{\varepsilon_{\mathrm{iso}}^{\mathrm{sim}}}$ is compatible with one.

Detector Region	$\varepsilon_{Data}/\varepsilon_{MC}$
$\lvert\eta\rvert < 0.9$	0.9590 ± 0.0004
$0.9 < \lvert\eta\rvert < 1.2$	0.9290 ± 0.0012
$1.2 < \lvert\eta\rvert < 2.1$	0.9809 ± 0.0009

Table 7.1.: Scaling factors K_i accounting for the difference of efficiencies in data and simulation. Based on the numbers from reference [92].

A visualization of the signal reconstruction acceptance and efficiency, the latter after applying the scale factors, is given in figure 7.6. Here, the acceptance is defined as the ratio of muons fulfilling $|\eta| < 2.1$ and all other muons coming from W' decays.

7.4. Recoil Correction

As shown in previous analyses [93, 25], the hadronic recoil is not well simulated in Monte Carlo. Here, recoil means a jet being emitted with transverse momentum before the vector boson production and therefore causing a boost of the W or Z in transverse direction. In order to correct for this the hadronic recoil had been derived from $pp \rightarrow Z \rightarrow \mu\mu$ data which is kinematically comparable to the W production and decay and afterwards applied to the W simulation.
However, a migration of the hadronic recoil correction by A. Güth to 8 TeV data is not easily performed, since the pileup conditions changed drastically and the correction is highly pileup-dependent [93]. Since the hadronic recoil only affects the $\mathrm{M_T}$ region up to about 140 GeV [25], its impact for this analysis is negligible. Therefore, a recoil correction was not performed for this analysis.

7.5. The Final $\mathrm{M_T}$-Distribution

After applying the corrections mentioned above including the $\mathrm{M_T}$ -binned k-factor for the W background (see section 5.2.1) the final $\mathrm{M_T}$ spectrum is shown in figures 7.7, 7.8. The cumulative distribution shows no excess for high transverse masses.

At low transverse masses of about 100-120 GeV the simulation predicts less data than measured. This is partly due to not applying a recoil correction and partly due to the fact that the trigger turn is not completely avoided by the requirement on the muon $p_T > 45$ GeV, and therefore the trigger efficiency and also the isolation efficiency

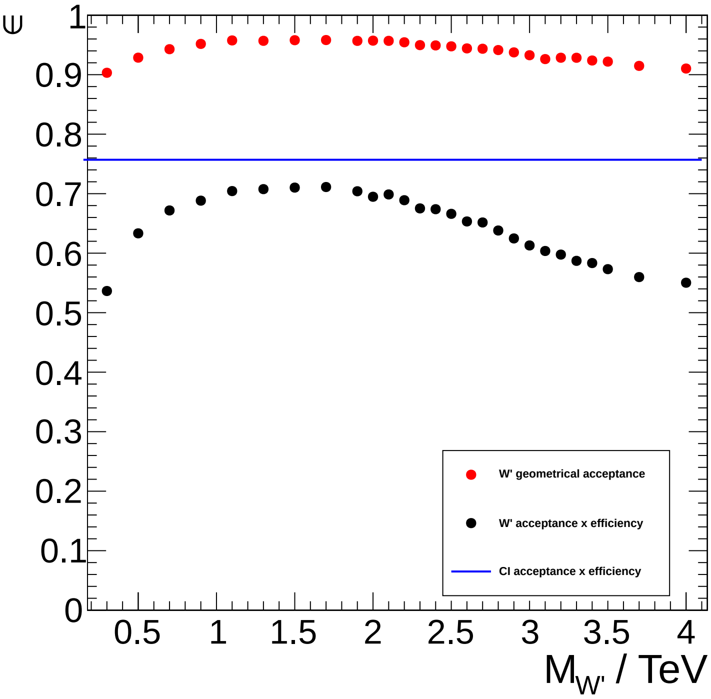

Figure 7.6.: Signal reconstruction acceptance×efficiency for different W' masses in comparison with the CI efficiency. For the W' samples, also the detector acceptance is shown. Here, the acceptance is defined as the ratio of muons fulfilling $|\eta| < 2.1$ and all other muons coming from W' decays. The CI acceptance×efficiency is higher than for W' due to the fact that CI is only simulated above $\hat{p}_T > 300$ GeV (see section 4.3.

are mis-simulated for low transverse momenta, see [92]. The highest event lies at an $\mathrm{M_T}$ of about 1.8 TeV. In the next chapter, the corresponding background expectation for M_T >1.75 TeV is estimated to about 0.46 ± 0.18.

7.5.1. Event Display of the Highest $\mathrm{M_T}$ Event

The highest $\mathrm{M_T}$ event lies at 1.78 TeV. It is a nicely reconstructed muon with all the reconstruction algorithms (see section 3.1.4) considered by cocktail muons in good agreement, which can be seen in table 7.2. The tracker-plus-first-muon-station algorithm (TPFMS) was chosen by the cocktail algorithm, which is another indication of the quality of the measurement, since TPFMS is the first choice - only being rejected, if the quality of the measurement is non-optimal. An event display in the $\rho - \phi$ plane can be seen in figure 7.9. Displayed is the muon track and the direction of the particle flow missing transverse energy.

Reconstruction Algorithm	p_T / GeV
Tracker only	934 ± 179
Picky	913 ± 49
TPFMS (chosen by cocktail)	903 ± 48

Table 7.2.: Comparison of the results of the p_T measurement of the muon in the highest $\mathrm{M_T}$ event. The algorithms agree very well with the p_T from the tracker track being afflicted with the highest uncertainty. The cocktail algorithm chose the tracker-plus-first-muon-station algorithm (TPFMS).

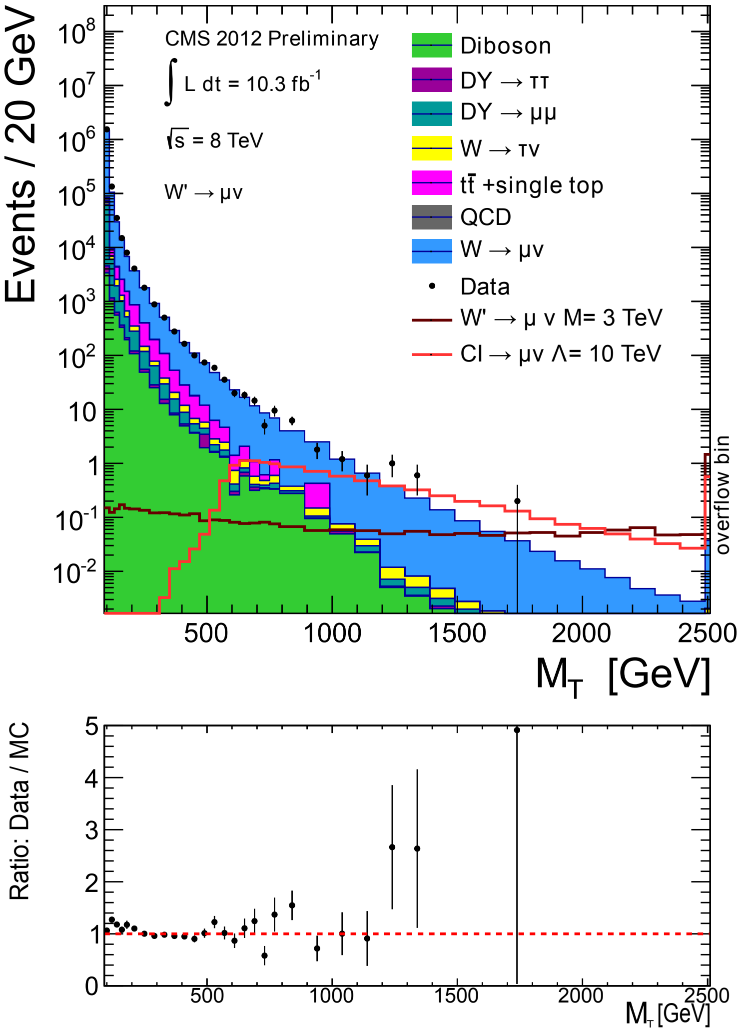

Figure 7.7.: The final distribution of the transverse mass with the ratio between data and simulation. A rebinning is applied to account for the varying detector resolution.

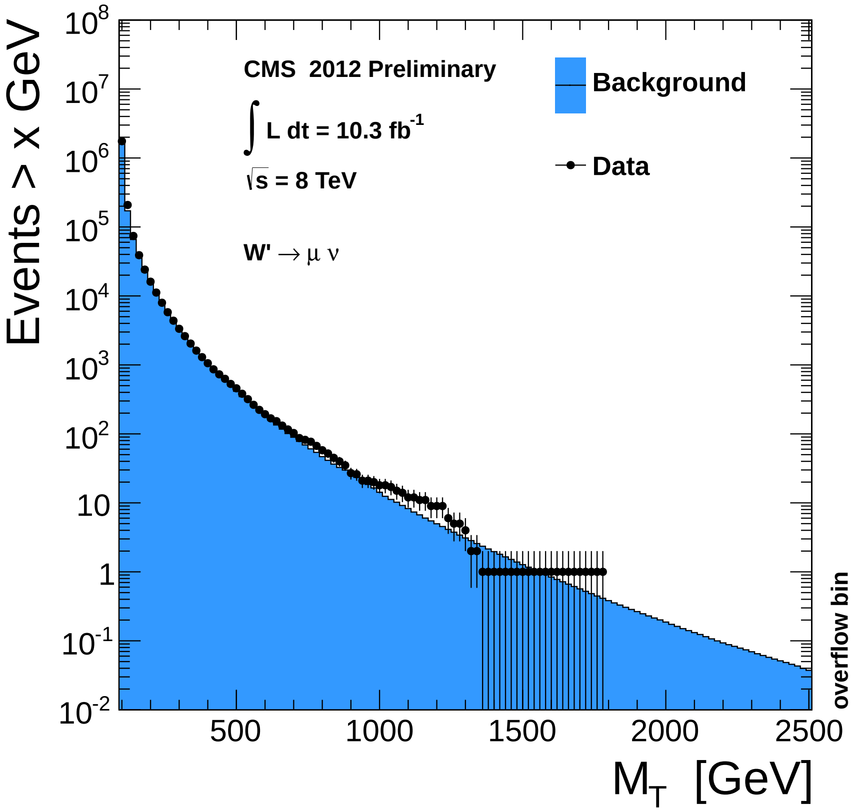

Figure 7.8.: The cumulative M_T-distribution. No excess for high transverse masses has been observed.

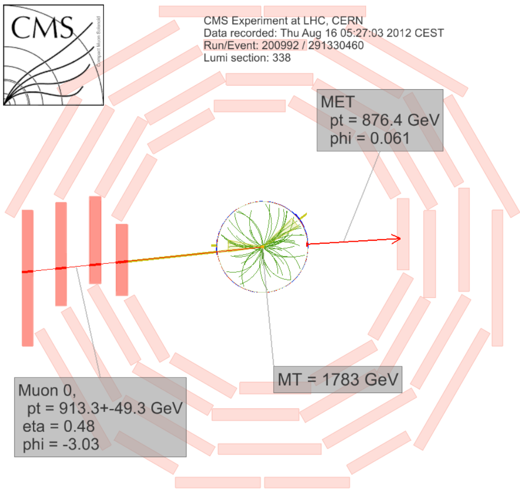

Figure 7.9.: An event display of the highest $\mathrm{M_T}$ event in the muon channel with a muon of $p_T = 903 \pm 48$ GeV in the $\rho - \phi$ plane.

8. Background Determination and Systematic Uncertainties

This section deals with the uncertainties resulting from limited precision of CMS measurements and limited understanding of the detector and the reconstruction. The discussion of uncertainties on cross sections arising from imperfect knowledge of the parton distribution functions has already been performed in section 4.4.

8.1. Systematic Uncertainties

The quantities influencing the transverse mass spectrum are not exactly known, since they are obtained by measurements and therefore afflicted with systematic uncertainties, which propagate into the $\mathrm{M_T}$ distribution. The impact of those uncertainties has to be evaluated before a statistical analysis can be performed. Uncertainties arise from the luminosity measurement as well as from limited precision of detector measurements and the pileup scenario. Uncertainties of quantities that influence the event reconstruction are taken into account by shifting or smearing the considered property by the estimated value of the uncertainty and redoing the $\mathrm{M_T}$ determination afterwards. In the following the considered uncertainties are summarized and discussed in more detail.

- **Luminosity Measurement**
  The luminosity measurement at CMS is performed as stated in section 2.2.5. The integrated luminosity of 10.3 fb^{-1} considered in this analysis is given with a relative uncertainty of 4.4 % [48]. Shifting the luminosity up and down results in a change of expected background events, but leaves the shape of the simulated background unaffected.

- **Muon Momentum Scale**
  Most important for the event reconstruction in this analysis is the measurement of the high-p_T muon. Differences in simulation and data could lead to a scaling of the p_T measurement. This scale uncertainty has been determined specifically for high-p_T muon reconstruction using the muon cocktail algorithm, as performed in this analysis. The scale study utilized cosmic muons traversing the detector and was performed by the muon particle object group [94]. To account for a dependency on the muon-p_T it has been recommended to take $\frac{p_T^\mu}{\mathrm{TeV}} \cdot 5\ \%$ as a scale factor uncertainty, i.e. 2.5% on a muon with a p_T of 0.5 TeV.
  This is taken into account by generating two additional $\mathrm{M_T}$ histograms, in which the muon p_T is shifted up and down by the scale uncertainty, respectively. Since also the MET changes with the muon momentum, it is recalculated, as well.

- **Muon Momentum Resolution**
  Another property of the muon reconstruction that could differ from data in the simulation is the muon momentum resolution. To account for the uncertainty from measurements, the muon p_T is smeared by 3.2% on the p_T. This is motivated by the uncertainty on the resolution of cocktail muons with $p_T > 200$ GeV shown in figure 3.1. The measured resolution lies at 6.2 % with an absolute uncertainty of about 0.8 % (conservatively read off). In order to yield a shift-up of the resolution by the 0.8 %, an additional smearing of 3.2 % is performed, assuming Gaussian addition of resolutions.

- **Missing Transverse Energy**
  Besides the muon p_T, the transverse mass is influenced by the MET measurement. The MET is only indirectly measured as the negative of the sum over all measured transverse momenta per event. Thus, the uncertainties on the different objects propagate into the MET uncertainty and have to be estimated. Since for events containing high-p_T-muons, the MET is mostly driven by the leading muon, the main source of MET and its uncertainties is already covered by the above two points.
  The remaining MET is predominantly made up by hadronic components. All other components have negligible impact on the MET in this analysis. The uncertainty on the MET resolution is covered by smearing the transverse momentum of the hadronic component by 10 %, which is motivated by studies of the CMS MET working group showing that the MET is underestimated in simulation by up to 10 % [95].

  The hadronic component of MET is also scaled by a factor of 0.1 as a conservative estimate, since the recommendation of the MET Working Group is to assume 10% uncertainty on the unclustered energy [53]. This term comprises all jets with transverse momenta under 10 GeV and all other objects reconstructed by the particle-flow algorithm (see section 3.2), which do not lie within a jet. Therefore, unclustered energy mainly consists of hadronic activity and the estimate of the uncertainty is reasonable. The uncertainties on the jet energy scale correction of jets with a p_T >10 GeV, which also contribute to the MET uncertainty [53], are also covered with this approach.

- **Pileup**
  All simulated events are assigned a weight accounting for the relative frequency of the number of simulated vertices compared to data, cf. section 7.1. The estimation of vertices per event in data is done by multiplying the measured instantaneous luminosity with the total inelastic cross section of pp-collisions. For the latter the measurement for a LHC center-of-mass energy of 7 TeV (68 mb) has been extrapolated to 69 mb for 8 TeV. Studies on $Z \rightarrow \mu\mu$ events show better agreement for the number of vertices between data and simulation, if one takes 73.5 mb as pp-cross section. As recommended in reference [88], the official extrapolated value is used for reweighting. But since the difference is not yet understood, it is taken

into account as a systematic uncertainty. This is done by evaluating another $\mathrm{M_T}$ background estimation after reweighting according to a total inelastic *pp*-cross section of 73.5 mb.

- **NLO Correction of W**
  The continuous NLO k-factor for the simulated W background was derived from a fit on the $\mathrm{M_T}$ binned k-factor as illustrated in figure 5.3. The uncertainty emerging from the fit are taken into account by shifting the k-factor up and down by one standard deviation, yielding a background expectation for the standard model W slightly shifted by about 1-2 %.

- **Scaling Factors**
  Since the efficiencies of the used trigger, the muon quality selection and the isolation are not perfectly simulated, scaling factors are applied on the background expectation, as described in section 7.3. Since those scaling factors come with a statistical uncertainty, the $\mathrm{M_T}$ spectrum is additionally shifted up and down to estimate the arising uncertainty on the background prediction. The effect is rather negligible, because the uncertainty is given as 0.05 % (see figure 7.1), averaged over the whole range in the pseudorapidity, which is three orders of magnitude less than the scale factor from the luminosity uncertainty.

- **Fit Error**
  A last uncertainty comes from a fit to the final distribution, which is explained in the next section. The uncertainty is made up by the biggest difference between the main function and two control functions and by the uncertainties on the fit parameters.

The largest uncertainties stem from the scaling of the MET and of the muon p_T with the latter being more dominant at high M_T, since the scale uncertainty increases with the muon momentum. The impact of MET and muon resolution is comparatively smaller, since the background does not contain narrow resonances below 100 GeV and is therefore not very sensitive to smearing. The uncertainties coming from scaling of the W k-factor, the pileup and scale factors are found to be negligible compared to the other sources. A display of the impact of the most influencing uncertainty sources is displayed in figure 8.1. The strong fluctuations at about 1 TeV and above 2 TeV are due to a lack of statistics in the simulation. The former is made up by $t\bar{t}$ and the first W tail, simulated up to $p_T^\mu = 500$ GeV, the latter by the W Monte-Carlo sample, which corresponds to $p_T^\mu > 500$ GeV.

8.2. Background Evaluation

The background prediction in this analysis is taken from simulation. As previously shown, a W' or contact interaction would be mostly visible at high $\mathrm{M_T}$ where the steeply falling background, mostly coming from the W, would not dominate any more. Since some backgrounds, especially multi-jet and $t\bar{t}$ lack statistics for higher transverse masses so called spiking can occur, which means that the few events at very high masses get a relatively high weight from the normalization to the integrated luminosity and produce a very high event prediction in a single bin, caused by possibly only one simulated event. Furthermore, the W background prediction begins to lack statistics at very high masses. In order to account for these two problems, a function is fit to the simulated event prediction in the $\mathrm{M_T}$ range from 300 to 4000 GeV and its integral considered as background expectation. In order to account for systematic uncertainties, the same function is also fit to all smeared distributions and the difference to the unchanged spectrum is computed. All uncertainties arising from scaling of a property up and down are conservatively treated and the maximal deviation is taken as uncertainty.

Three functions have been found to describe the steepy falling M_T spectrum of the standard model background reasonably well.

- $f_1(M_T) = \frac{a}{(M_T^3 + b \cdot M_T + c)^d}$
- $f_2(M_T) = \frac{a}{(M_T^2 + b \cdot M_T + c)^d}$
- $f_3(M_T) = \frac{a(1+M_T)^b}{M_T^{c+d \cdot \log(M_T)}}$

Since f_1 was shown to describe the spectrum best [83] it is taken for the final background prediction and is also fit to all smeared spectra. f_2 and f_3 are considered as control functions and their difference to f_1 is added as uncertainty as well as uncertainties which arise from the fit parameters of f_1. However, both are found to be comparatively small. The spectrum with the three fits is shown in figure 8.1.

The result of the background estimation compared to data is given in table 8.1. The total uncertainty is calculated as the sum of squares of all uncertainty sources. All deviations between data and simulation are well-covered by the systematic uncertainties, therefore no significant deviation is found, especially for high transverse masses, where a possible signal would appear.

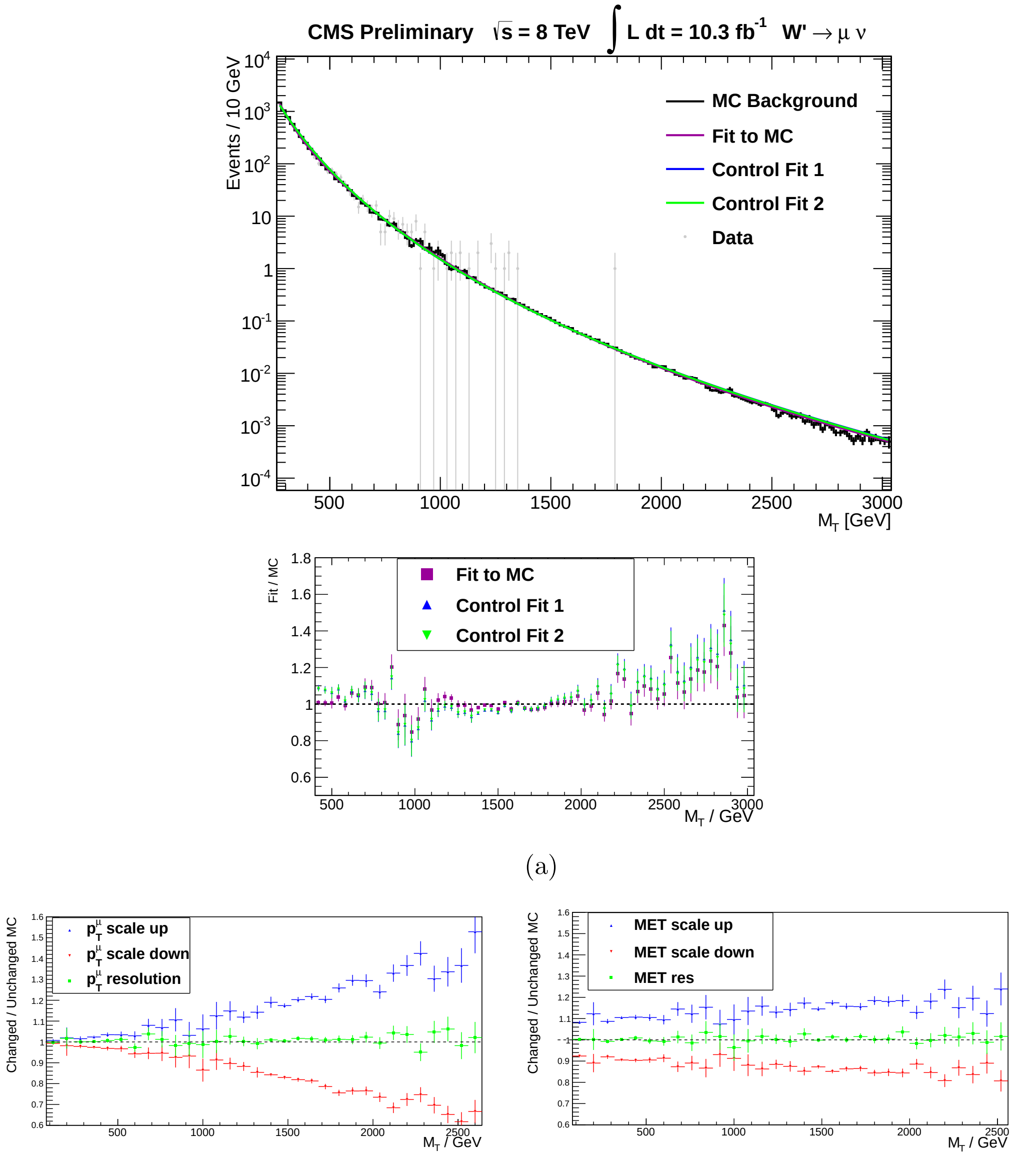

(a)

(b)

(c)

Figure 8.1.: (a) The transverse mass spectrum with the three fit functions. The ratio of the fits and the simulation is shown in (a) It can be seen that for M_T of 800-1000 GeV the statistical fluctuation of the simulation is relatively strong. This is caused by the diminishing statistics of the second W background sample for 100 GeV$< p_T <$ 500 GeV. At $M_T = 2.2$ TeV the simulation starts to lack statistics causing a decrease of background expectation. This is compensated by the fit. Also shown is the impact of the systematic uncertainties represented by the ratios between the smeared/scaled and the unchanged background expectation for (b) the muon and (c) the MET.

$M_T >$ / GeV	N_{ev} (Data)	N_{ev} (fit)	total uncert.	N_{ev} (Sim)
> 300	3341	3340	490	3430
> 400	1058	1070	170	1060
> 500	458	421	66	414
> 600	193	188	31	181
> 800	58	46.4	9.0	46.9
> 1000	18	14.0	3.1	14.1
> 1200	9	4.9	1.2	4.9
> 1400	1	1.91	0.56	1.94
> 1600	1	0.82	0.28	0.83
> 1750	1	0.46	0.18	0.48

Table 8.1.: Number of predicted events by the fit to simulation with total systematic uncertainty compared to data. No statistically significant deviations are observed. The highest event yields a transverse mass of about 1.8 TeV.

9. Statistical Analysis and Limit Setting

No significant deviations from the standard model expectation in the signal region have been discovered in this analysis as shown in the previous chapter. In order to quantify the result and relate it to the signal predictions, a statistical analysis is performed to derive an exclusion limit for the possible signals. It is sufficient to simply take the background and signal expectation above a certain transverse mass and compare it to the sum of all data events above this $\mathrm{M_T}$ threshold. This approach is called single-bin counting and discussed later on. In order to derive a limit on a certain physics model, one adds the predicted signal contribution to the background prediction and calculates the compatibility to the data in a statistical manner which is explained in the next section.

9.1. Bayesian Statistics

The method for deriving an upper cross-section limit chosen in this analysis is based on a Bayesian approach. In order to exclude a SSM W' or a contact interaction in the HNC model, it is calculated as a function of $m_{W'}$ and Λ, respectively, and afterwards compared to the signal cross sections, listed in sections 4.2.1 and 4.3.2.
The following introduction to Bayesian statistics is adapted from [96, 27].

If one is armed with a background expectation b, a signal expectation s and a number of measured events N_{data}, two options are widely common in particle physics to calculate an exclusion limit to a certain confidence interval.
The first method, named $\mathrm{CL_s}$, is based on *frequentist* statistics: First, the probability of the occurrence of N_{data} events is calculated for the signal-plus-background hypothesis $s + b$ and for the background-only hypothesis b. A confidence interval is then derived from the two probabilities.
In the second approach, which is less CPU-intensive for comparable results (as shown in previous analyses [25, 97]), the strategy is different. Instead of comparing the signal-plus-background hypothesis to N_{data}, the reversed approach is taken. A Poisson-Likelihood as a function of the signal contribution s at constant b under the precondition of N_{data} observed events is defined as

$$L(s|N_{\mathrm{data}}) = \frac{(s+b)^{N_{\mathrm{data}}}}{N_{\mathrm{data}}!} \cdot e^{-(s+b)}. \tag{9.1}$$

The parameter of interest s is composed of the total signal cross section (times the branching ratio to $\mu\nu$) and the signal efficiency ε, divided by $\mathcal{L}$.

A special feature of Bayesian statistics is that it is capable of taking into account information about the parameter of interest, which is known *a priori*, like physical boundaries for cross section or even subjective beliefs. This is applied by introducing the prior function $\pi(s)$ into the Likelihood function. If one wants to derive a probability $p(s|N_{\text{data}})$, the Likelihood has first to be normalized:

$$p(s|N_{\text{data}}) = \frac{L(s|N_{\text{data}}) \cdot \pi(s)}{\int L(s'|N_{\text{data}}) \cdot \pi(s') ds'} \tag{9.2}$$

$p(s|N_{\text{data}})$ is called the *posterior* probability density function (p.d.f.). In this analysis, a flat prior function $\pi(s)$ is used, which is 1 for $s > 0$, else 0. This is motivated by the fact that nothing is known about the cross sections of W' and CI, but they should be positive. Some quantities, e.g. b and $\mathcal{L}$, that enter the Likelihood function are afflicted with a systematic uncertainty. This is taken into account by inserting an additional prior function $\pi(\vec{\nu}) = \prod\limits_i \pi(\nu_i)$ into the Likelihood. Every component of the vector of *nuisance parameters* $\vec{\nu}$ represents the uncertainty of a certain parameter, e.g. the luminosity. Integrating over the different $\pi(\nu_i)$ leads to an additional smearing of the Likelihood function. The $\pi(\nu_i)$ are considered to follow a log-normal distribution [98] in ν_i, since this describes the distribution of a non-negative random variable. The posterior probability now reads

$$p(s|N_{\text{data}}) = \frac{\int L(s|N_{\text{data}}) \cdot \pi(s) \cdot \pi(\vec{\nu}) d\vec{\nu}}{\int \int L(s'|N_{\text{data}}) \cdot \pi(s') \cdot \pi(\vec{\nu}) ds' d\vec{\nu}}. \tag{9.3}$$

An upper limit $s_{95\%}$ on the signal contribution s to a confidence level of 95 % is now derived from solving the following equation numerically:

$$\text{C.L.} = 0.95 = \int_{-\inf}^{s_{95\%}} p(s'|N_{\text{data}}) ds'. \tag{9.4}$$

The observed upper cross-section limit $\sigma_{95\%}$ is now simply calculated by $\sigma_{95\%} = s_{95\%}/\mathcal{L}$.

Beside the observed limit an expected limit can be estimated using only the background expectation and not taking into account the observed data. It is derived by dicing 400 pseudo-experiments following the posterior probablility function. The calculation also includes dicing of the nuisance parameters, which follows their prior functions, to account for the systematic uncertainties. The expected limit is then defined as the median limit of the 400 pseudo-experiments. The expected limit is provided together with 1-σ (0,68-quantile) and 2-σ (0,95-quantile) bands that allow for an estimation how significant the observed and expected limits deviate. Deviations occur, if the observed event yield differs from the background prediction.
If the observed number of events is lower, the observed limit is lower than the expected limit, since a lower signal cross section can be excluded. If more data is measured than expected, a possible signal cannot be ruled out and therefore the observed cross-section limit is relatively higher.

Since theories that predict a W' often presume lepton-universality, an additional exclusion potential can be attained by combining the results of the electron and muon search channel. This is done by obtaining a combined posterior p.d.f. by simply multiplying the two Likelihoods. The confidence level is then calculated by integrating over the common parameter of interest, the cross section $\sigma_{W'}$. The systematic uncertainties are taken into account by integrating over all the nuisance parameters in the different channels. All uncertainties are thereby assumed to be uncorrelated except the luminosity, which is fully correlated. The common parameter of interest is the signal cross section. This is possible, since it is assumed to be equal in both channels.

An analogous procedure has not been performed in terms of contact interaction, because the limit in the electron channel was not available, when this thesis was written. Since the relationship between the energy scales Λ_μ Λ_e is not predefined by the HNC model, a combined limit could only be given in a $\Lambda_\mu - \Lambda_e$ parameter space, where no correlation between the energy scales is assumed.

9.2. Single-bin-counting Experiment

Since the shape of the CI signal contains no narrow resonance and the Jacobian peak of the W' is smeared very strongly for high masses due to the detector resolution and increasing width, almost no information gets lost, if one integrates from a lower border to infinity and just uses the background expectation and data of this one "bin". This is a contrast to a shape-based statistical analysis, as it is done in searches for narrow resonances, like the $Z' \to ee$ [99], where the observed spectrum has to be scanned for narrow deviations. For the limit setting, the integral of simulated background and signal is compared to data above the $\mathrm{M_T}$ threshold.

The parameter of interest s can be simply calculated from the signal efficiency ε, divided by $\mathcal{L}$. The value of ε, besides the total signal cross section, contains the model-specific information and is dependent on $M_{W'}$ (see figure 7.6), but not on Λ, as explained in section 4.3. These properties manifest in the shape of the exclusion limits, shown in the following.

The majority of potential signal events for a W' with a mass of 300 GeV lies in a completely different $\mathrm{M_T}$ regime than for a W' with $M = 3.5$ TeV. For high W' masses and for contact interaction, high lower thresholds of the $M_T$search window are generally expected to result in a smaller excluded cross section than lower ones, since the signal-to-background ratio is more advantageous at high transverse masses due to a steeply falling background. In order to choose the search window for the limit setting, the lower threshold is optimized for the best expected limit. Since the expected limit does not depend on observed events, the optimization requires no consideration of the look-elsewhere effect, which accounts for the probability of deviations in data due to statistical fluctuation, if a wide range of bins is analysed. The optimization is performed for every W' mass, but only needed once for the contact interaction, since ε stays the same and only the cross section σ_{CI} scales down with increasing Λ. The optimization is done by performing 400 pseudo-experiments per search window. All the expected limits are then compared and the bin with the lowest expected upper cross-section limit is chosen. The lower bounds of the search windows are chosen in steps of 50 GeV.

While the minimum of the expected limit is very narrow for small W' masses, it broadens for higher $M_{W'}$. This can lead to statistical fluctuation of the estimated minimal expected limit, therefore a sufficient number of dicing is needed.

The limit computation, including optimizing the search window is performed using a RooStats-based [60] tool made for the Higgs analysis [61].

9.3. The Contact Interaction Limit

The expected and observed upper cross-section limit as well as the cross section of the contact interaction depending on the energy scale Λ can be seen in figure 9.1. The projection of the intersection of the observed limit and the CI cross section is taken as the upper limit on the energy scale. It is conservatively estimated, compatible with the PDF uncertainty within one standard deviation, to

$$\Lambda_{\mathrm{CI}\rightarrow\mu\nu} > 10.0 \text{ TeV} \quad \text{at } 95\ \%\ \text{C.L.} \tag{9.5}$$

The observed and expected limits are flat, since the signal efficiency ε is the same for all energy scales.
The corresponding quantitative information can be found in table 9.1, where the expected and observed limits are compared to the signal cross section and the number of observed data above the $\mathrm{M_T}$ threshold, optimized for best expected limit, is compared to the number of background and signal events. The optimization yielded 1100 GeV as lower bound of the search window. This is lower than the value found for heavy W', which is due to the fact that the CI spectrum does fall faster with high-$\mathrm{M_T}$ as shown in figure 7.7. The observed limit is found to be worse than expected, lying between the upper 1-σ and 2-σ band, which is due to 12 measured events at a background expectation of 8.1 ± 1.9 events.

9.4. The W' Mass Limit

The cross-section limit for a W' decaying to muon and neutrino as a function of $M_{W'}$ is shown in figure 9.2 with the detailed information in table 9.2. For masses of 2.3 TeV and above, the best expected limit was found in the mass windows with a lower bound of 1.65 and 1.70 TeV. Above 1.70 TeV the background expectation of 0.6 ± 0.2 is compatible with one observed event, which worsens the observed limit slightly with respect to the expected limit. Overall, the observed limit is found to lie well in between the 1-σ band of the expected limit.
At low W' masses, the upper limit strongly improves for an increasing $M_{W'}$ due to the advantageous signal-to-background ratio at high M_T. For very high masses, the limit begins to get worse again, because the off-shell production at low transverse masses begins to play a role. The optimization then finds search windows, with a decreasing lower bound in M_T, where the background is higher, which worsens the limit.
The upper limit on the W' mass from the muonic decay channel can be derived by the

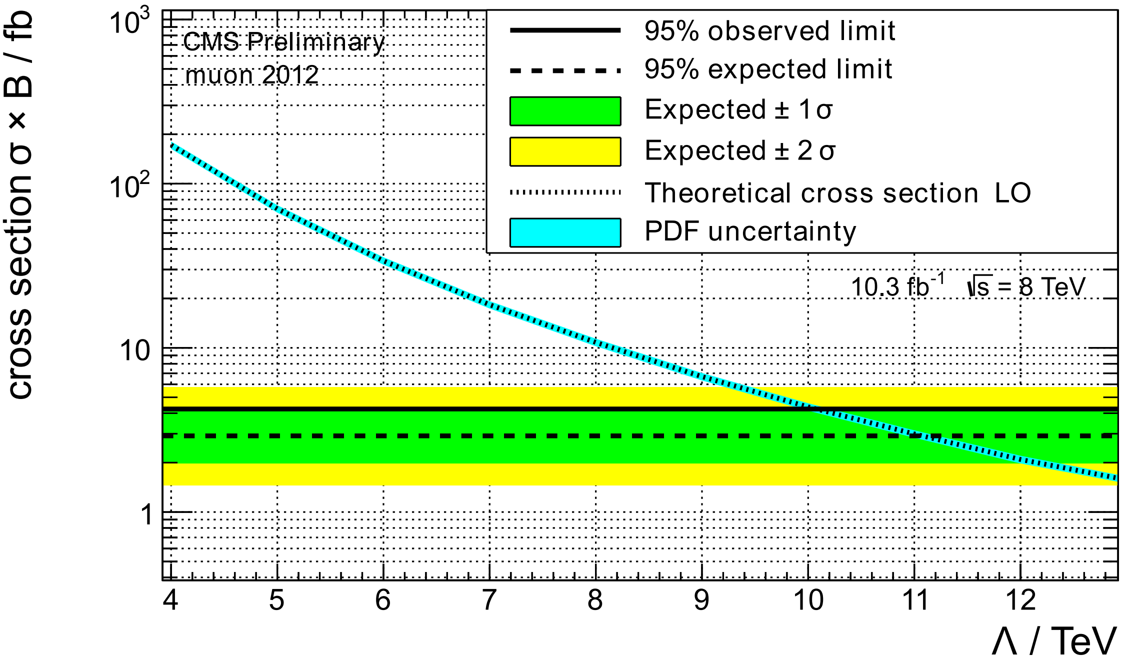

Figure 9.1.: Cross-section limit of a helicity-non-conserving contact interaction. The observed and expected cross section limits and the theoretical cross section as a function of the energy scale Λ are shown.

intersection of theoretical cross section and the observed limit to

$$M_{W'} > 2.9\ \text{TeV} \quad \text{at } 95\ \%\ \text{C.L.} \tag{9.6}$$

9.4.1. The Electron Limit and Channel Combination

The limit in the electron channel, analysed by Philipp Millet [100] and corresponding to the same integrated luminosity of 10.3 fb^{-1} is shown in figure A.1 in the appendix. The electron limit has a very similar shape for high masses due to a high-$\mathrm{M_T}$ event at 2.4 TeV. The lower W' mass limit also lies at 2.9 TeV.

A combination is made under the assumption that the branching ratios and cross sections in both channels are the same. The tau channel is also investigated, but has much less exclusion power because of a softer spectrum due to at least one additional neutrino. The combined limit is shown in figure 9.3 and table 9.3. The combined expected and observed limits are significantly improved by nearly a factor of 2 with respect to the single-channel limits. While the expected limit lies at $M_{W'} > 3.2$ TeV the observed upper limit on the W' mass derived from a combination of muon and electron channel is

$$M_{W'} > 3.0\ \text{TeV} \quad \text{at } 95\ \%\ \text{C.L.} \tag{9.7}$$

Λ / TeV	$M_T >$ X GeV	N_{data}	N_{sig}	N_{bgk}	σ_{CI} / fb	$\sigma_{\text{exp}}^{\text{excl}}$ / fb	$\sigma_{\text{obs}}^{\text{excl}}$ / fb
3	1100	12	1540 ± 120	8.1 ± 1.9	541.79	2.91	4.24
5	1100	12	489 ± 39	8.1 ± 1.9	171.82	2.91	4.24
6	1100	12	200 ± 16	8.1 ± 1.9	70.30	2.91	4.24
7	1100	12	96.5 ± 7.7	8.1 ± 1.9	33.87	2.91	4.24
8	1100	12	52.2 ± 4.2	8.1 ± 1.9	18.31	2.91	4.24
9	1100	12	30.8 ± 2.5	8.1 ± 1.9	10.80	2.91	4.24
10	1100	12	19.0 ± 1.5	8.1 ± 1.9	6.68	2.91	4.24
11	1100	12	12.4 ± 1.0	8.1 ± 1.9	4.37	2.91	4.24
12	1100	12	8.51 ± 0.68	8.1 ± 1.9	2.99	2.91	4.24
13	1100	12	5.95 ± 0.48	8.1 ± 1.9	2.09	2.91	4.24

Table 9.1.: The detailed information to the CI cross-section limit. Stated are the optimized $\mathrm{M_T}$ threshold, the number of expected signal, background and observed data and the observed and expected limit, compared to the signal cross section.

A combination with the electron and muon limit corresponding to 2011 data at $\sqrt{s}$=7 TeV, as performed in [1], has not been considered for the bigger dataset, which was used in this analysis, since the contribution would be negligible and was even only marginally improving the derived limit. This is due to the fact that already twice the data was recorded for this analysis and also a high increase of sensitivity for heavier W', because of the higher $\sqrt{s}$.

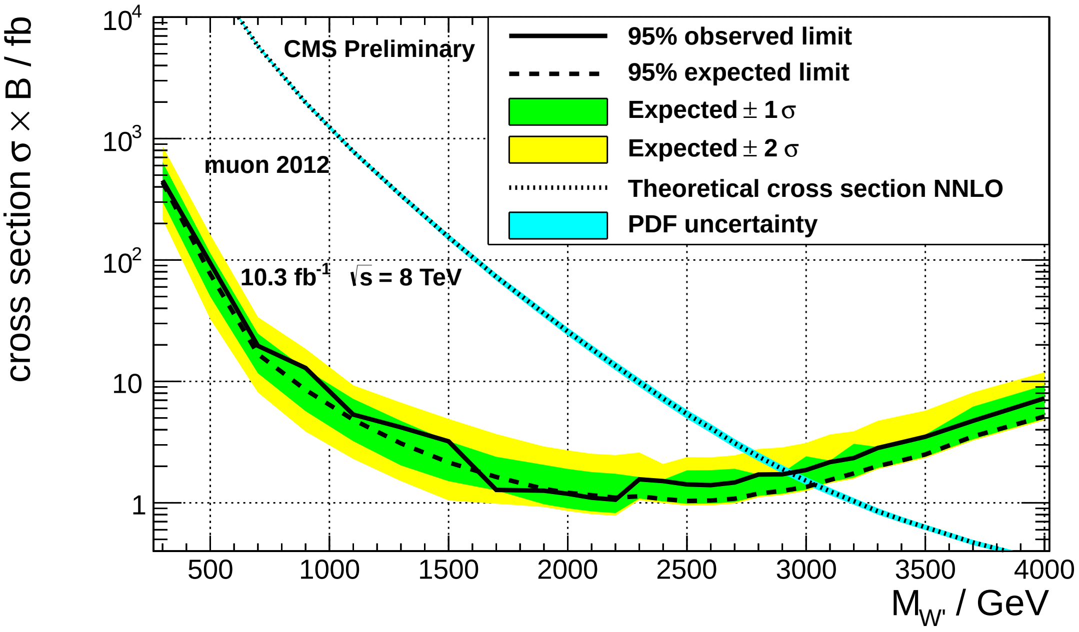

Figure 9.2.: Cross-section limit of W' decaying to muon and neutrino. The observed and expected cross section limits and the theoretical cross section as a function of the W' mass are shown.

$M_{W'}$ / GeV	M_T > X GeV	N_{data}	N_{sig}	N_{bgk}	$\sigma_{W'}$ / fb	$\sigma_{\mathrm{exp}}^{\mathrm{excl}}$ / fb	$\sigma_{\mathrm{obs}}^{\mathrm{excl}}$ / fb
500	450	730	51700 ± 4900	660 ± 100	22500	76.7	94.2
900	750	82	6120 ± 540	64 ± 12	1980	8.52	12.9
1300	1000	18	1239 ± 99	14.0 ± 3.1	341	3.09	4.19
1700	1400	1	202 ± 31	1.91 ± 0.56	72.7	1.63	1.28
2000	1450	1	90.0 ± 8.8	1.53 ± 0.47	25.8	1.21	1.19
2300	1700	1	28.0 ± 3.7	0.55 ± 0.21	9.83	1.13	1.56
2600	1650	1	13.0 ± 1.4	0.67 ± 0.24	4.12	1.05	1.40
2900	1650	1	4.90 ± 0.55	0.67 ± 0.24	1.90	1.25	1.72
3100	1700	1	2.58 ± 0.34	0.55 ± 0.21	1.24	1.54	2.17
3300	1700	1	1.37 ± 0.19	0.55 ± 0.21	0.85	2.00	2.83
3500	1650	1	0.82 ± 0.11	0.67 ± 0.24	0.63	2.50	3.50
4000	1650	1	0.21 ± 0.03	0.67 ± 0.24	0.33	5.15	7.26

Table 9.2.: The detailed information to the W' cross-section limit. Stated are the optimized $\mathrm{M_T}$ threshold, the number of expected signal, background and observed data and the observed and expected limit, compared to the signal cross section.

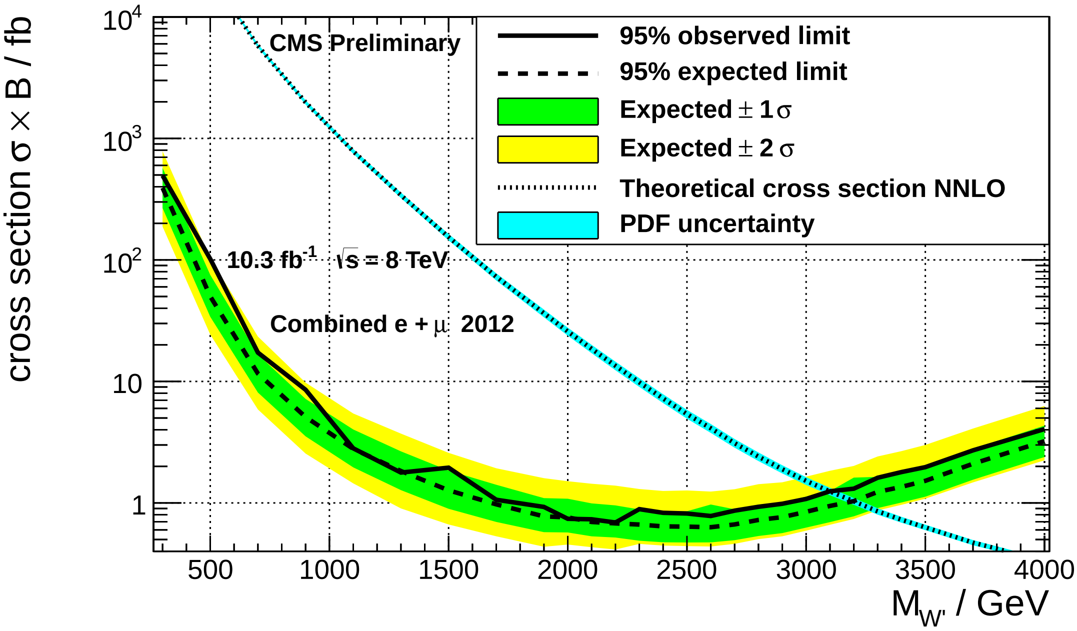

Figure 9.3.: The combined W' cross-section limit using information from the muon and the electron channel. The observed and expected cross section limits and the theoretical cross section as a function of the W' mass are shown.

$M_{W'}$ / GeV	$\sigma_{W'}$ / fb	$\sigma_{\text{exp}}^{\text{excl}}$ / fb	$\sigma_{\text{obs}}^{\text{excl}}$ / fb
900	2000	5.1	8.5
1700	73	0.97	1.1
2300	9.8	0.66	0.89
2900	1.9	0.76	0.99
3100	1.2	0.94	1.3
3300	0.85	1.2	1.6
3500	0.63	1.5	2.0
4000	0.33	3.2	4.1

Table 9.3.

10. Conclusion

In this thesis the search for two possible extensions of the standard model has been performed using a 2012 CMS dataset corresponding to an integrated luminosity of 10.3 fb^{-1} at a center-of-mass energy of $\sqrt{s} = 8$ TeV. The first subject of the search has been a helicity-non-conserving contact interaction, which is an effective theory with an energy scale Λ and could either be a reference model to theories predicting compositeness of the quarks and leptons or the exchange of a heavy neutral scalar particle, which is predicted in some standard model extensions. The second topic has been the search for a new heavy charged gauge boson, called W', which can decay into a muon and a neutrino. In order to have a simple model as a reference for the various different W' models that are predicted, standard-model-like couplings have been assumed as well as an exclusive coupling to right-handed (anti-)particles.

After a simulation-based background estimation the data was found to be in good agreement with the standard model prediction, and therefore the considered standard model extensions can be ruled out up to a W' mass of 2.9 TeV in the muon channel and up to an energy scale Λ of 10.0 TeV. By combining the muon and electron channel, masses up to $M_{W'}$ =3.0 TeV can be excluded.

With data from an earlier 2012 dataset corresponding to 3.7 fb^{-1} a publication of results partly based on this analysis was achieved [1], excluding a W' decaying to muon up to $M_{W'} = 2.75$ GeV and a HNC contact interaction up to $\Lambda = 8.7$ TeV, therefore yielding world's best limits from direct searches in both cases. A combination of electron and muon limit of 2011 and 2012 data yielded a $M_{W'}$ limit of 2.85 TeV. With respect to 2011, the search in the $\mu\nu$ channel has been extended by also considering the HNC model. The analysis of the HNC model in the electron channel is desirable as well and currently already ongoing. Possible left-handed W' bosons interfering with the W have been already considered in the searches in 2011 and have be not covered by this analysis due to the fact that the official production, which was mandatory, was delayed heavily, but now completed and therefore incorporated into the analysis chain as well. The search for a W' in the tau channel is currently being performed as well.

A. Appendix

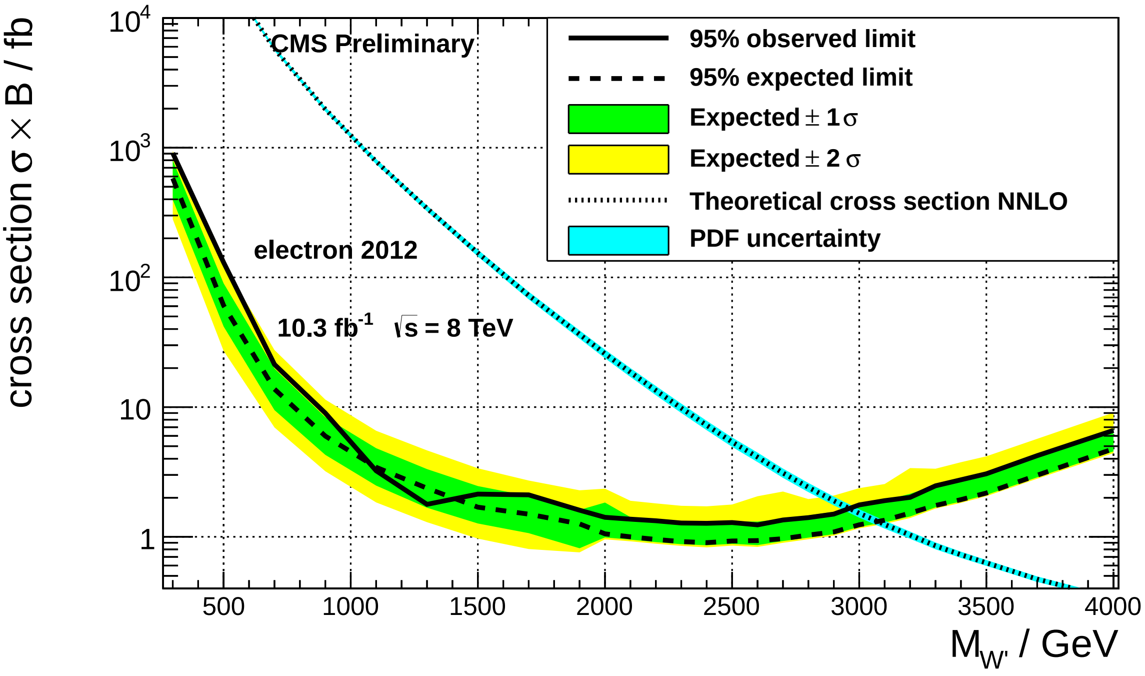

Figure A.1.: The information corresponding to the W' cross-section limit from the decay channel to electron and neutrino. Shown are the optimized $\mathrm{M_T}$ threshold, the number of expected signal, background and observed events and the observed and expected limit, compared to the signal cross section.

	CT10			MSTW2008			NNPDF 2.1
[%]	$\Delta\sigma^{\mathrm{PDF}}$	$\Delta\sigma^{\alpha_s}$	total	$\Delta\sigma^{\mathrm{PDF}}$	$\Delta\sigma^{\alpha_s}$	total	total
$M_{W'} = 300$ GeV	+ 2.2) - 2.5	+ 0.1 -0.2	+ 2.2 - 2.5	+ 2.1 - 1.6	+ 0.3 - 0.3	+ 2.1 - 1.7	± 1.8
$M_{W'} = 500$ GeV	+ 2.4 - 3.2	+0.2 - 0.2	+ 2.4 - 3.2	+ 2.3 - 1.8	<+0.1 - 0.0	+ 2.3 - 1.8	± 2.2
$M_{W'} = 700$ GeV	+ 2.9 - 3.9	+0.4 - 0.4	+ 2.9 - 3.9	+ 2.6 - 2.0	+0.2 -0.2	+ 2.6 - 2.0	± 2.8
$M_{W'} = 1100$ GeV	+ 4.0 - 5.1	+0.6 - 0.6	+ 4.1 - 5.2	+ 3.2 - 2.2	+0.5 -0.5	+ 3.3 - 2.2	± 3.7
$M_{W'} = 1300$ GeV	+ 4.7 - 5.7	+0.7 - 0.7	+ 4.7 - 5.8	+ 3.5 - 2.3	+0.6 -0.6	+ 3.6 - 2.3	± 4.0
$M_{W'} = 1500$ GeV	+ 5.5 - 6.5	+0.6 - 0.6	+ 5.6 - 6.5	+ 3.9 - 2.4	+0.7 -0.7	+ 4.0 - 2.5	± 4.4
$M_{W'} = 1900$ GeV	+ 7.1 - 7.6	+0.5 - 0.5	+ 7.2 - 7.6	+ 4.3 - 2.6	+0.8 -0.8	+ 4.4 - 2.7	± 4.9
$M_{W'} = 2000$ GeV	+ 7.4 - 7.8	+0.5 - 0.5	+ 7.5 - 7.8	+ 4.3 - 2.7	+0.8 -0.8	+ 4.4 - 2.8	± 5.1
$M_{W'} = 2200$ GeV	+ 8.2 - 8.2	+0.3 - 0.4	+ 8.2 - 8.2	+ 4.4 - 2.9	+0.7 -0.7	+ 4.4 - 2.9	± 5.5
$M_{W'} = 2400$ GeV	+ 8.4 - 8.3	+0.3 - 0.3	+ 8.4 - 8.3	+ 4.3 - 2.9	+0.5 -0.5	+ 4.3 - 3.0	± 5.4
$M_{W'} = 2600$ GeV	+ 8.7 - 8.2	+0.1 - 0.2	+ 8.7 - 8.2	+ 4.2 - 3.0	+0.4 -0.4	+ 4.2 - 3.0	± 5.5
$M_{W'} = 2800$ GeV	+ 8.6 - 7.7	+ <0.1 - 0.0	+ 8.6 - 7.7	+ 4.0 - 3.0	+0.2 -0.2	+ 4.0 - 3.0	± 5.7
$M_{W'} = 3000$ GeV	+ 8.0 - 6.8	+ 0.1 -0.1	+ 8.0 - 6.8	+ 3.7 - 2.8	+0.1 -0.1	+ 3.7 - 2.8	± 5.6
$M_{W'} = 3200$ GeV	+ 7.0 - 5.9	+ 0.1 >-0.1	+ 7.0 - 5.9	+ 3.2 - 2.4	<+0.1 >-0.1	+ 3.2 - 2.4	± 5.7
$M_{W'} = 3300$ GeV	+ 6.6 - 5.6	+ 0.1 -0.1	+ 6.6 - 5.6	+ 3.1 - 2.3	+ <0.1 - 0.0	+ 3.1 - 2.3	± 5.0
$M_{W'} = 3400$ GeV	+ 6.1 - 5.1	+ 0.1 -0.1	+ 6.1 - 5.1	+ 2.9 - 2.2	+ 0.1 - 0.1	+ 2.9 - 2.2	± 4.7
$M_{W'} = 3700$ GeV	+ 4.8 - 4.1	+ 0.1 -0.1	+ 4.8 - 4.1	+ 2.4 - 1.8	+ 0.1 - 0.1	+ 2.4 - 1.8	± 4.9
$M_{W'} = 4000$ GeV	+ 3.7 - 3.6	+ <0.1 >-0.1	+ 3.7 - 3.6	+ 2.1 - 1.6	+ 0.1 - 0.1	+ 2.1 - 1.6	± 3.9

Table A.1.: Summary of the PDF uncertainties on the W' production cross section for different values of $M_{W'}$.

	CT10			MSTW2008			NNPDF 2.1
[%]	$\Delta\sigma^{\mathrm{PDF}}$	$\Delta\sigma^{\alpha_s}$	total	$\Delta\sigma^{\mathrm{PDF}}$	$\Delta\sigma^{\alpha_s}$	total	total
$\Lambda = 3$ TeV	+ 4.7 - 5.7	+ 0.5 - 0.5	+ 4.8 - 5.7	+ 3.5 - 2.2	+ 0.5 - 0.5	+ 3.5 - 2.3	± 4.0
$\Lambda = 5$ TeV	+ 4.7 - 5.7	+ 0.5 - 0.5	+ 4.7 - 5.7	+ 3.4 - 2.2	+ 0.5 - 0.5	+ 3.5 - 2.3	± 4.0
$\Lambda = 6$ TeV	+ 4.7 - 5.7	+ 0.5 - 0.5	+ 4.8 - 5.8	+ 3.4 - 2.3	+ 0.5 - 0.5	+ 3.5 - 2.3	± 4.0
$\Lambda = 7$ TeV	+ 4.7 - 5.7	+ 0.5 - 0.5	+ 4.7 - 5.7	+ 3.5 - 2.3	+ 0.5 - 0.5	+ 3.5 - 2.3	± 4.0
$\Lambda = 8$ TeV	+ 4.8 - 5.7	+ 0.5 - 0.5	+ 4.9 - 5.7	+ 3.4 - 2.2	+ 0.5 - 0.5	+ 3.5 - 2.3	± 4.1
$\Lambda = 9$ TeV	+ 4.7 - 5.7	+ 0.5 - 0.5	+ 4.8 - 5.8	+ 3.4 - 2.2	+ 0.5 - 0.5	+ 3.5 - 2.3	± 4.1
$\Lambda = 10$ TeV	+ 4.7 - 5.7	+ 0.5 - 0.5	+ 4.8 - 5.7	+ 3.4 - 2.2	+ 0.5 - 0.5	+ 3.4 - 2.3	± 4.2
$\Lambda = 11$ TeV	+ 4.7 - 5.7	+ 0.5 - 0.5	+ 4.7 - 5.7	+ 3.4 - 2.3	+ 0.4 - 0.4	+ 3.5 - 2.3	± 4.1
$\Lambda = 12$ TeV	+ 4.8 - 5.9	+ 0.6 - 0.6	+ 4.9 - 6.0	+ 3.5 - 2.3	+ 0.6 - 0.6	+ 3.6 - 2.4	± 4.3
$\Lambda = 13$ TeV	+ 4.4 - 5.2	+ 0.5 - 0.5	+ 4.5 - 5.2	+ 3.2 - 2.2	+ 0.5 - 0.5	+ 3.3 - 2.2	± 4.5
$\Lambda = 14$ TeV	+ 4.9 - 6.0	+ 0.6 - 0.7	+ 4.9 - 6.0	+ 3.5 - 2.4	+ 0.6 - 0.6	+ 3.5 - 2.5	± 4.6

Table A.2.: Summary of the PDF uncertainties on the contact interaction cross section for different values of the energy scale Λ.

Table A.3.: Analysed Monte Carlo samples for various background processes (with $\ell = e, \mu$). In case only LO cross sections are known, the column for NNLO stays empty. $\hat{p}_T$ stands for the scale of the hard interaction in the respective case. Two different pileup scenarios, corresponding to production in the CMSSW versions [56] 52X and 53X, respectively, have been used for the official production, with the latter being much closer at the actual pileup. For further information, see section 7.1. The (*) denotes that for the sample a $\mathrm{M_T}$ -binned NLO k-factor has been used, see section 5.2.1.

Generator	Process	Kinematic cuts (in GeV,)	σ_{LO} (pb)	σ_{NNLO} (pb)	Pileup Scenario	# of Events
`PYTHIA`	W $\rightarrow \mu\nu$	no cuts	9130	12100	53X	~5M
`PYTHIA`	W $\rightarrow \mu\nu$	$500 < \hat{p}_T > 100$ GeV	1.46	(*)	53X	~1M
`PYTHIA`	W $\rightarrow \mu\nu$	$\hat{p}_T > 500$ GeV	0.00152	(*)	53X	~1M
`PYTHIA`	W $\rightarrow \tau\nu$	no cuts	9170	12100	52X	~2.5M
`PYTHIA`	W $\rightarrow \tau\nu$	$500 < \hat{p}_T > 100$ GeV	1.46	(*)	52X	~1M
`PYTHIA`	W $\rightarrow \tau\nu$	$\hat{p}_T > 500$ GeV	0.00153	(*)	52X	~1M
`PYTHIA`	Z/$\gamma* \rightarrow \mu\mu$	$m_{\mu\mu} > 20$ GeV	1510	1920	52X	~2M
`PYTHIA`	Z/$\gamma* \rightarrow \mu\mu$	$m_{\mu\mu} > 120$ GeV	3.9	11.9	52X	~0.5M
`PYTHIA`	Z/$\gamma* \rightarrow \mu\mu$	$m_{\mu\mu} > 200$ GeV	1.18	1.49	52X	~ 50k
`PYTHIA`	Z/$\gamma* \rightarrow \mu\mu$	$m_{\mu\mu} > 500$ GeV	0.0356	0.0451	52X	~50K
`PYTHIA`	Z/$\gamma* \rightarrow \mu\mu$	$m_{\mu\mu} > 800$ GeV	0.00451	0.00572	52X	~50K
`PYTHIA`	Z/$\gamma* \rightarrow \mu\mu$	$m_{\mu\mu} > 1300$ GeV	0.00015	0.00045	52X	~50K
`PYTHIA`	Z/$\gamma* \rightarrow \mu\mu$	$m_{\mu\mu} > 1600$ GeV	0.00009	0.00012	52X	~50K
`PYTHIA`	Z/$\gamma* \rightarrow \tau\tau$	$m_{\tau\tau} > 20$ GeV	1510	1920	52X	~2M
`PYTHIA`	Z/$\gamma* \rightarrow \tau\tau$	100 GeV$< m_{\tau\tau} > 200$ GeV	44.3	58.5	53X	~200k
`PYTHIA`	Z/$\gamma* \rightarrow \tau\tau$	200 GeV$< m_{\tau\tau} > 400$ GeV	1.45	2.00	53X	~1M
`PYTHIA`	Z/$\gamma* \rightarrow \tau\tau$	400 GeV$< m_{\tau\tau} > 800$ GeV	0.110	1.45	53X	~1M
`PYTHIA`	Z/$\gamma* \rightarrow \tau\tau$	$m_{\tau\tau} > 800$ GeV	0.0057	0.0075	53X	~1M
`Madgraph`	$t\bar{t}$	no cuts	136	225 (NLO)	53X	~1.2M
`Powheg`	$t \rightarrow bl\nu$ (s-Channel)	no cuts	2.82	3.89	53X	~300k
`Powheg`	$t \rightarrow bl\nu$ (t-Channel)	no cuts	47.0	55.5	53X	~400k
`Powheg`	$t \rightarrow bl\nu$ (tW-Channel DR)	no cuts	10.7	11.2	53X	~500k
`Powheg`	$\bar{t} \rightarrow bl\nu$ (s-Channel)	no cuts	1.57	1.76	53X	~140k
`Powheg`	$\bar{t} \rightarrow bl\nu$ (t-Channel)	no cuts	25.0	30.0	53X	~2M
`Powheg`	$\bar{t} \rightarrow bl\nu$ (tW-Channel DR)	no cuts	10.7	11.2	53X	~500k
`PYTHIA`	WW	no cuts	33.6	57.1	53X	~10M
`PYTHIA`	WZ	no cuts	12.6	32.3	53X	~10M
`PYTHIA`	ZZ	no cuts	5.2	8.3	53X	~10M
`PYTHIA`	WW	$\hat{p}_T > 500$ GeV	0.00523	0.00890	53X	~1M
`PYTHIA`	WZ	$\hat{p}_T > 500$ GeV	0.00170	0.00435	53X	~1M
`PYTHIA`	ZZ	$\hat{p}_T > 500$ GeV	0.00106	0.00170	53X	~1M
`PYTHIA`	QCD μ enriched	20 GeV$< \hat{p}_T < 30$ GeV	$2.87 \cdot 10^8$	-	53X	~8M
`PYTHIA`	QCD μ enriched	30 GeV$< \hat{p}_T < 50$ GeV	$6.61 \cdot 10^7$	-	53X	~5M
`PYTHIA`	QCD μ enriched	50 GeV$< \hat{p}_T < 80$ GeV	$8.08 \cdot 10^6$	-	53X	~10M
`PYTHIA`	QCD μ enriched	80 GeV$< \hat{p}_T < 120$ GeV	$1.02 \cdot 10^6$	-	52X	~10M
`PYTHIA`	QCD μ enriched	120 GeV$< \hat{p}_T < 170$ GeV	$1.58 \cdot 10^5$	-	52X	~8M
`PYTHIA`	QCD μ enriched	170 GeV$< \hat{p}_T < 300$ GeV	$3.40 \cdot 10^4$	-	52X	~8M
`PYTHIA`	QCD μ enriched	300 GeV$< \hat{p}_T < 470$ GeV	1760	-	52X	~4M
`PYTHIA`	QCD μ enriched	470 GeV$< \hat{p}_T < 600$ GeV	115	-	52X	~4M
`PYTHIA`	QCD μ enriched	600 GeV$< \hat{p}_T < 800$ GeV	27.0	-	52X	~4M
`PYTHIA`	QCD μ enriched	800 GeV$< \hat{p}_T < 1000$ GeV	3.57	-	52X	~4M
`PYTHIA`	QCD μ enriched	1000 GeV$< \hat{p}_T$	0.774	-	52X	~4M

$M_{W'}$	No Selection	*Preselection*	Quality Selection & only 1 μ	p_T^μ/MET	$\Delta\phi(p_T^\mu$,MET)
0.3 TeV	$1.58197\cdot10^{6}$ 100%	$1.11\cdot10^{6}$ 70.1% 70.1%	$1.01\cdot10^{6}$ 63.9% 91.1%	$9.08\cdot10^{5}$ 57.4% 89.8%	$8.52\cdot10^{5}$ 53.8% 93.8%
0.5 TeV	$2.32\cdot10^{5}$ 100%	$1.84\cdot10^{5}$ 79.2% 79.2%	$1.68\cdot10^{5}$ 72.3% 91.3%	$1.56\cdot10^{5}$ 67.2% 92.8%	$1.5\cdot10^{5}$ 64.5% 96.1%
0.7 TeV	$5.97\cdot10^{4}$ 100%	$4.86\cdot10^{4}$ 81.5% 81.5%	$4.45\cdot10^{4}$ 74.5% 91.4%	$4.21\cdot10^{4}$ 70.6% 94.8%	$4.09\cdot10^{4}$ 68.5% 97.1%
0.9 TeV	$2.05\cdot10^{4}$ 100%	$1.66\cdot10^{4}$ 81.3% 81.3%	$1.53\cdot10^{4}$ 74.9% 92.1%	$1.46\cdot10^{4}$ 71.3% 95.2%	$1.42\cdot10^{4}$ 69.6% 97.7%
1.1 TeV	$8.08\cdot10^{3}$ 100%	$6.69\cdot10^{3}$ 82.7% 82.7%	$6.13\cdot10^{3}$ 75.8% 91.6%	$5.87\cdot10^{3}$ 72.7% 95.9%	$5.76\cdot10^{3}$ 71.3% 98.1%
1.3 TeV	$3.52\cdot10^{3}$ 100%	$2.89\cdot10^{3}$ 82.1% 82.1%	$2.66\cdot10^{3}$ 75.6% 92%	$2.57\cdot10^{3}$ 72.9% 96.5%	$2.52\cdot10^{3}$ 71.6% 98.1%
1.5 TeV	$1.59\cdot10^{3}$ 100%	$1.31\cdot10^{3}$ 82.1% 82.1%	$1.2\cdot10^{3}$ 75.2% 91.6%	$1.16\cdot10^{3}$ 72.9% 97%	$1.15\cdot10^{3}$ 72.1% 98.9%
1.7 TeV	750 100%	611 81.5% 81.5%	564 75.2% 92.3%	547 72.9% 96.9%	541 72.1% 98.8%
1.9 TeV	376 100%	302 80.4% 80.4%	278 74.1% 92.2%	271 72% 97.2%	267 71.1% 98.8%
2.0 TeV	266 100%	212 79.8% 79.8%	196 73.6% 92.2%	189 71.2% 96.8%	187 70.3% 98.7%
2.1 TeV	192 100%	154 80.3% 80.3%	141 73.8% 92%	137 71.7% 97.1%	136 70.8% 98.8%
2.2 TeV	139 100%	110 79.4% 79.4%	102 73.1% 92.2%	98.3 70.7% 96.7%	96.8 69.7% 98.5%
2.3 TeV	101 100%	79.8 78.6% 78.6%	73.1 72% 91.6%	70.4 69.4% 96.4%	69.5 68.5% 98.7%
2.4 TeV	74.8 100%	58.4 78.2% 78.2%	53.5 71.6% 91.6%	51.7 69.2% 96.6%	51.1 68.3% 98.7%
2.5 TeV	55.6 100%	42.8 77% 77%	39.4 70.9% 92.1%	38 68.4% 96.5%	37.6 67.5% 98.8%
2.6 TeV	42.5 100%	32.4 76.2% 76.2%	29.8 70% 91.8%	28.7 67.5% 96.5%	28.3 66.5% 98.5%
2.7 TeV	32 100%	24.4 76.1% 76.1%	22.4 70% 91.9%	21.6 67.3% 96.3%	21.2 66.1% 98.2%
2.8 TeV	24.8 100%	18.7 75.1% 75.1%	17.1 68.8% 91.6%	16.4 66% 95.9%	16.1 64.8% 98.2%
2.9 TeV	19.6 100%	14.6 74.4% 74.4%	13.3 67.8% 91.1%	12.6 64.6% 95.3%	12.4 63.3% 97.9%
3.0 TeV	15.7 100%	11.5 73.4% 73.4%	10.5 67% 91.4%	10 63.9% 95.3%	9.77 62.3% 97.6%
3.1 TeV	12.8 100%	9.31 72.5% 72.5%	8.5 66.2% 91.2%	8.07 62.9% 95%	7.88 61.3% 97.6%
3.2 TeV	10.6 100%	7.61 71.4% 71.4%	6.97 65.5% 91.7%	6.62 62.2% 94.9%	6.45 60.6% 97.4%
3.3 TeV	8.81 100%	6.23 70.8% 70.8%	5.68 64.5% 91.1%	5.38 61% 94.7%	5.23 59.4% 97.4%
3.4 TeV	7.51 100%	5.32 70.8% 70.8%	4.86 64.7% 91.3%	4.59 61.1% 94.4%	4.45 59.2% 97%
3.7 TeV	4.87 100%	3.35 68.7% 68.7%	3.06 62.8% 91.4%	2.87 58.9% 93.8%	2.77 56.8% 96.5%
4 TeV	3.45 100%	2.32 67.4% 67.4%	2.12 61.7% 91.4%	1.99 57.9% 93.8%	1.91 55.5% 96%

Λ_{CI}	No Selection	*Preselection*	Quality Selection & only 1 μ	p_T^μ/MET	$\Delta\phi(p_T^\mu$,MET)
3 TeV	$5.59\cdot10^{3}$ 100%	$4.8\cdot10^{3}$ 85.7% 85.7%	$4.42\cdot10^{3}$ 79.1% 92.2%	$4.33\cdot10^{3}$ 77.4% 97.8%	$4.29\cdot10^{3}$ 76.8% 99.2%
4 TeV	$1.77\cdot10^{3}$ 100%	$1.52\cdot10^{3}$ 85.7% 85.7%	$1.4\cdot10^{3}$ 79.1% 92.2%	$1.37\cdot10^{3}$ 77.4% 97.8%	$1.36\cdot10^{3}$ 76.8% 99.2%
5 TeV	726 100%	622 85.7% 85.7%	574 79.1% 92.2%	562 77.4% 97.8%	557 76.8% 99.2%
6 TeV	350 100%	300 85.7% 85.7%	277 79.1% 92.2%	271 77.4% 97.8%	268 76.8% 99.2%
7 TeV	189 100%	162 85.7% 85.7%	150 79.1% 92.2%	146 77.4% 97.8%	145 76.8% 99.2%
8 TeV	112 100%	95.6 85.7% 85.7%	88.2 79.1% 92.2%	86.3 77.4% 97.8%	85.6 76.8% 99.2%
9 TeV	69 100%	59.1 85.7% 85.7%	54.5 79.1% 92.2%	53.4 77.4% 97.8%	53 76.8% 99.2%
10 TeV	45.1 100%	38.7 85.7% 85.7%	35.7 79.1% 92.2%	34.9 77.4% 97.8%	34.6 76.8% 99.2%
11 TeV	30.9 100%	26.5 85.7% 85.7%	24.4 79.1% 92.2%	23.9 77.4% 97.8%	23.7 76.8% 99.2%
12 TeV	21.6 100%	18.5 85.7% 85.7%	17.1 79.1% 92.2%	16.7 77.4% 97.8%	16.6 76.8% 99.2%
13 TeV	16.3 100%	14 85.7% 85.7%	12.9 79.1% 92.2%	12.6 77.4% 97.8%	12.5 76.8% 99.2%

Table A.4.: Selection efficiencies and predicted event counts according to $\mathcal{L}_{\text{int}} = 10.3\ \text{fb}^{-1}$ for the W' and CI signals. The left percentage corresponds to the remaining events relative to the event number before all selections. The right percentage denotes the efficiency relative the the selection stage given before.

Bibliography

[1] "Search for leptonic decays of W' bosons in pp collisions at sqrt(s)=8 TeV,". `http://cdsweb.cern.ch/record/1461725/files/EXO-12-010-pas.pdf`.

[2] A. Pich, "The Standard model of electroweak interactions," `arXiv:hep-ph/0502010 [hep-ph]`.

[3] T. Hebbeker, "Skript zur Vorlesung Einführung in die Elementarteilchenphysik," RWTH 2010.

[4] CMS Collaboration, "Observation of a new boson at a mass of 125 GeV with the CMS experiment at the LHC," *Phys.Lett.* **B716** (2012) 30–61, `arXiv:1207.7235 [hep-ex]`.

[5] ATLAS Collaboration, "Observation of a new particle in the search for the Standard Model Higgs boson with the ATLAS detector at the LHC," *Phys.Lett.* **B716** (2012) 1–29, `arXiv:1207.7214 [hep-ex]`.

[6] "Wikipedia article on the Standard Model," 2012. `http://en.wikipedia.org/wiki/Standard_Model`.

[7] P. A. M. Dirac, "The quantum theory of the electron," *Proc. R. Soc. Lond.* **117** (Feb, 1928) 610–624. `http://rspa.royalsocietypublishing.org/content/117/778/610.citation#cited-by`.

[8] D. J. Gross and F. Wilczek, "Asymptotically free gauge theories," *Phys. Rev. D* **8** (Nov, 1973) 3633–3652. `http://link.aps.org/doi/10.1103/PhysRevD.8.3633`.

[9] S. Glashow, "Partial Symmetries of Weak Interactions," *Nucl.Phys.* **22** (1961) 579–588.

[10] S. Weinberg, "A model of leptons," *Phys. Rev. Lett.* **19** (Nov, 1967) 1264–1266. `http://link.aps.org/doi/10.1103/PhysRevLett.19.1264`.

[11] F. Englert and R. Brout, "Broken symmetry and the mass of gauge vector mesons," *Phys. Rev. Lett.* **13** (Aug, 1964) 321–323. `http://link.aps.org/doi/10.1103/PhysRevLett.13.321`.

[12] P. W. Higgs, "Broken symmetries, massless particles and gauge fields," *Physics Letters* **12** no. 2, (1964) 132 – 133. `http://www.sciencedirect.com/science/article/B6X44-46WP33M-12/2/385879093eff5919fee5c0a669409d1c`.

[13] G. S. Guralnik, C. R. Hagen and T. W. B. Kibble, "Global conservation laws and massless particles," *Phys. Rev. Lett.* **13** (Nov, 1964) 585–587. `http://link.aps.org/doi/10.1103/PhysRevLett.13.585`.

[14] T. W. B. Kibble, "Symmetry breaking in non-Abelian gauge theories," *Phys. Rev.* **155** (1967) 1554–1561.

[15] F. Zwicky, "On the Masses of Nebulae and of Clusters of Nebulae," *ApJ* **86** (Nov, 1937) 217.

[16] D. Clowe, M. Bradac, A. H. Gonzalez *et al.*, "A direct empirical proof of the existence of dark matter," *Astrophys.J.* **648** (2006) L109–L113, `arXiv:astro-ph/0608407 [astro-ph]`.

[17] V. Gribov and B. Pontecorvo, "Neutrino astronomy and lepton charge," *Phys.Lett.* **B28** (1969) 493.

[18] A. D. Sakharov, "Violation of CP in variance, C asymmetry, and baryon asymmetry of the universe," *Soviet Physics Uspekhi* **34** no. 5, (1991) 392. `http://stacks.iop.org/0038-5670/34/i=5/a=A08`.

[19] R. N. Mohapatra and J. C. Pati, "Left-right gauge symmetry and an "isoconjugate" model of CP violation," *Phys. Rev. D* **11** (Feb, 1975) 566–571. `http://link.aps.org/doi/10.1103/PhysRevD.11.566`.

[20] W. Grimus, "Introduction to left-right symmetric models," 1993.

[21] R. N. Mohapatra and G. Senjanović, "Neutrino mass and spontaneous parity nonconservation," *Phys. Rev. Lett.* **44** (Apr, 1980) 912–915. `http://link.aps.org/doi/10.1103/PhysRevLett.44.912`.

[22] G. Beall, M. Bander and A. Soni, "Constraint on the mass scale of a left-right-symmetric electroweak theory from the $K_L - K_S$ mass difference," *Phys. Rev. Lett.* **48** (Mar, 1982) 848–851. `http://link.aps.org/doi/10.1103/PhysRevLett.48.848`.

[23] G. Altarelli, B. Mele and M. Ruiz-Altaba, "Searching for New Heavy Vector Bosons in p$\bar{\text{p}}$ Colliders," *Z. Phys.* **C45** (1989) 109.

[24] T. Sjöstrand, S. Mrenna and P. Z. Skands, "PYTHIA 6.4 Physics and Manual," *JHEP* **05** (2006) , `arXiv:hep-ph/0603175`. `http://arxiv.org/pdf/hep-ph/0603175v2`.

[25] S. Thüer, "Search for heavy charged gauge bosons in the decay channel $W' \to \mu\nu$ with CMS data," Master's thesis, RWTH, 2012.

[26] P. B. Renton, "Precision electroweak tests of the standard model," *Reports on Progress in Physics* **65** no. 9, (2002) 1271. `http://stacks.iop.org/0034-4885/65/i=9/a=202`.

[27] K. Nakamura *et al.* (Particle Data Group), "Review of Particle Physics," *J. Phys.* **G 37, 075021** (2010) .

[28] D. Kim, Y. Oh and S. C. Park, "W' in new physics models at the LHC," `arXiv:1109.1870 [hep-ph]`.

[29] D. Kim *et al.*, "UED driven W' decay," *CMS Analysis Note: AN-11-471* (2011) .

[30] K. A. H. Terazawa, M. Yasue and M. Hayashi, "Observable Effects of the Possible Substructure of Leptons and Quarks," *Phys. Lett.* **B112** (1982) 387, `arXiv:hep-ph/1110.0713v1`.

[31] GEM Collaboration, "GEM Technical Design Report," 1993.

[32] K. D. Lane, F. E. Paige, T. Skwarnicki and W. J. Womersley, "Simulations of supercollider physics," *Phys.Rept.* **278** (1997) 291–371, `arXiv:hep-ph/9412280 [hep-ph]`.

[33] P. K. Lane, "Private communication," 2012.

[34] Dr. A. Knochel, , "Private communication," 2012.

[35] CDF Collaboration, "Search for quark lepton compositeness and a heavy W' boson using the $e\nu$ channel in $p\bar{p}$ collisions at $\sqrt{s} = 1.8$ TeV," *Phys.Rev.Lett.* **87** (2001) 231803, `arXiv:hep-ex/0107008 [hep-ex]`.

[36] J. Ellis *et al.*, "QCD and collider physics," *Camb.Monogr.Part.Phys.Nucl.Phys.Cosmol.* **8** (1996) 1–435.

[37] X. C. Vidal and R. C. Manzano, "Taking a closer look at LHC: Beta and Emittance," 2012. `http://www.lhc-closer.es/php/index.php?i=1&s=4&p=18&e=0`.

[38] L. Evans and P. Bryant, "LHC Machine," *Journal of Instrumentation* **3** no. 08, (2008) S08001. `http://stacks.iop.org/1748-0221/3/i=08/a=S08001`.

[39] CMS Collaboration, "Public Results on Luminosity in CMS. TWiki Website," 2012. `https://twiki.cern.ch/twiki/bin/view/CMSPublic/LumiPublicResults`.

[40] CMS Collaboration, "The CMS experiment at the CERN LHC," *JINST* **3** no. S08004, (2008) .

[41] The Atlas Collaboration, "The ATLAS Experiment at the CERN Large Hadron Collider," *JINST* **3** (2008) S08003. `http://jinst.sissa.it/LHC/`.

[42] The LHCb Collaboration, "The LHCb Detector at the LHC," *Journal of Instrumentation* **3** no. 08, (2008) S08005. `http://stacks.iop.org/1748-0221/3/i=08/a=S08005`.

[43] The ALICE Collaboration, "The ALICE experiment at the CERN LHC," *Journal of Instrumentation* **3** no. 08, (2008) S08002. `http://stacks.iop.org/1748-0221/3/i=08/a=S08002`.

[44] CMS Collaboration, "Performance of CMS muon reconstruction in pp collision events at sqrt(s) = 7 TeV," *ArXiv e-prints* (June, 2012) , `arXiv:1206.4071 [physics.ins-det]`.

[45] CMS Collaboration, *The CMS muon project: Technical Design Report.* Technical Design Report CMS. CERN, Geneva, 1997.

[46] CMS Collaboration, "The tridas project technical design report, volume 2: Data acquisition and high-level trigger," *CERN/LHCC* **2002-26** (2002) .

[47] S. Van der Meer, "Calibration of the effective beam height in the ISR," *CERN-ISRPO* **D77** (1968) 68–31.

[48] CMS Collaboration, "CMS Luminosity Based on Pixel Cluster Counting - Summer 2012 Update," 2012.

[49] CMS Collaboration, "Muon reconstruction in the CMS detector," *CMS Note* **2008/097** (2008) .

[50] The CMS Collaboration, "Performance of CMS muon reconstruction in pp collision events at $\sqrt{s} = 7$ TeV," `arXiv:1206.4071 [physics.ins-det]`.

[51] J. Caudron, "Retuning of muon cocktail for high pT muons with fully segment based fit. Talk," 2012. `https://indico.cern.ch/getFile.py/access?contribId=7&resId=0&materialId=slides&confId=184964`.

[52] The CMS Collaboration, "Particle-flow event reconstruction in CMS and performance for jets, taus, and MET," Apr, 2009.

[53] The Missing ET Working Group, "Official Prescription for calculating uncertainties on Missing Transverse Energy (MET)," 2012. `https://twiki.cern.ch/twiki/bin/viewauth/CMS/MissingETUncertaintyPrescription`.

[54] The CERN Collaboration, "Website of the European Organization for Nuclear Research," 2012. `http://public.web.cern.ch/public/en/About/Global-en.html,`.

[55] The LHC Collaboration, "The Worldwide LHC Computing Grid," 2012. `http://wlcg.web.cern.ch/`.

[56] The CMS Collaboration, "CMSSW Application Framework. Twiki Website," 2012. `https://twiki.cern.ch/twiki/bin/view/CMSPublic/WorkBookCMSSWFramework#ReviewStatus`.

[57] "Data Formats and Data Tiers. Twiki website," 2012. `https://twiki.cern.ch/twiki/bin/view/CMSPublic/WorkBookDataFormats`.

[58] C. Magass *et al.*, "Aachen 3A Susy Analysis. Twiki Website," 2012. `https://twiki.cern.ch/twiki/bin/viewauth/CMS/Aachen3ASusy`.

[59] I. Antcheva, M. Ballintijn, B. Bellenot, M. Biskup *et al.*, "ROOT: A C++ framework for petabyte data storage, statistical analysis and visualization," *Comput.Phys.Commun.* **182** (2011) 1384–1385.

[60] S. Schmitz *et al.*, "The RooStats page. Twiki Website," 2012. `https://twiki.cern.ch/twiki/bin/view/CMS/RooStats`.

[61] The CMS Collaboration, "Documentation of the RooStats-based statistics tools for Higgs PAG. Twiki Website," 2012. `https://twiki.cern.ch/twiki/bin/view/CMS/SWGuideHiggsAnalysisCombinedLimit#Introduction`.

[62] GEANT4 Collaboration, "GEANT4: A simulation toolkit," *Nucl. Instrum. Meth.* **A506** (2003) 250.

[63] R. Gavin, Y. Li, F. Petriello and S. Quackenbush, "FEWZ 2.0: A code for hadronic Z production at next-to-next-to-leading order," *Comput.Phys.Commun.* **182** (2011) 2388–2403, `arXiv:1011.3540 [hep-ph]`.

[64] D. Kim *et al.*, "PDF Uncertainties and K-factor for the W' Search at 8 TeV Collisions," *CMS Analysis Note: AN-12-172* (2012) .

[65] The LHC4PDF Working Group, "Recommendation for LHC cross section calculations," 2012. `http://www.hep.ucl.ac.uk/pdf4lhc/`.

[66] H. L. Lai, M. Guzzi, J. Huston, Z. Li, P. M. Nadolsky *et al.*, "New parton distributions for collider physics," *Phys.Rev.* **D82** (2010) 074024, `arXiv:1007.2241 [hep-ph]`.

[67] A. D. Martin, W. J. Stirling, R. S. Thorne and G. Watt, "Parton distributions for the LHC," *The European Physical Journal C* **63** (2009) 189–285. `http://dx.doi.org/10.1140/epjc/s10052-009-1072-5`.

[68] R. D. Ball, V. Bertone *et al.*, "Impact of Heavy Quark Masses on Parton Distributions and LHC Phenomenology," *Nucl.Phys.* **B849** (2011) 296–363, `arXiv:1101.1300 [hep-ph]`.

[69] G. Sterman *et al.*, "Handbook of perturbative QCD," *Rev. Mod. Phys.* **67** (Jan, 1995) 157–248. `http://link.aps.org/doi/10.1103/RevModPhys.67.157`.

[70] D. Bourilkov, R. C. Group and M. R. Whalley, "LHAPDF: PDF use from the Tevatron to the LHC," `arXiv:hep-ph/0605240 [hep-ph]`.

[71] M. R. Whalley D. Bourilkov *et al.*, "The Les Houches accord PDFs (LHAPDF) and LHAGLUE," `arXiv:hep-ph/0508110 [hep-ph]`.

[72] The CMS Luminosity Group, "The official CMS Luminosity Calculation. TWiki Website," 2012. `https://twiki.cern.ch/twiki/bin/viewauth/CMS/LumiCalc#lumiCalc2_py_and_pixel_LumiCalc`.

[73] The CMS DQM Group, "Data Certification at DQM Group. TWiki Website," 2012. `https://twiki.cern.ch/twiki/bin/view/CMS/DataCertificationatDQMGroup`.

[74] J. Alwall *et al.*, "MadGraph/MadEvent v4: the new web generation," *JHEP* **09** (2007) 028, `arXiv:0706.2334v1`.

[75] C. Oleari, "The POWHEG-BOX," *Nucl.Phys.Proc.Suppl.* **205-206** (2010) 36–41, `arXiv:1007.3893 [hep-ph]`.

[76] W.-M. Yao *et al.*, "Review of Particle Physics," *Journal of Physics G* **33** (2006) 68–31. `http://pdg.lbl.gov`.

[77] S. Brensing *et al.*, "Radiative corrections to W^- boson hadroproduction: Higher-order electroweak and supersymmetric effects," *Phys.Rev.* **D77** (2008) 073006, `arXiv:0710.3309 [hep-ph]`.

[78] C. Calame *et al.*, "Precision electroweak calculation of the production of a high transverse-momentum lepton pair at hadron colliders," *JHEP* **0710** (2007) 109, `arXiv:0710.1722 [hep-ph]`.

[79] S. Frixione and B. R. Webber, "Matching NLO QCD computations and parton shower simulations," *JHEP* **0206** (2002) 029, `arXiv:hep-ph/0204244 [hep-ph]`.

[80] M. Olschewski, "Private communication," 2012.

[81] G. Balossini *et al.*, "Combination of electroweak and QCD corrections to single W production at the Fermilab Tevatron and the CERN LHC," *JHEP* **1001** (2010) 013, `arXiv:0907.0276 [hep-ph]`.

[82] CMS Collaboration, "Baseline Muon Selections. Twiki Website," 2012. `https://twiki.cern.ch/twiki/bin/view/CMSPublic/SWGuideMuonId`.

[83] T. Poljansek, "Suche nach einem neuen schweren Eichboson W' im myonischen Zerfallskanal mit 2012er CMS Daten," Bachelor's thesis, 2012.

[84] C. Hof, "Detection of new heavy charged gauge bosons with the future cms detector," diploma thesis, RWTH, 2005.

[85] C. Magass, "Search for new heavy charged gauge bosons," PhD thesis, RWTH Aachen, 2007.

[86] W. Bender, "Studie zum Nachweis schwerer, geladener Eichbosonen in leptonischen Zerfallskanälen mit dem CMS-Detektor," diploma thesis, RWTH Aachen, 2008.

[87] K. Padeken, "Private communication," 2012.

[88] The CMS Collaboration, "Utilities for Accessing Pileup Information for Data. TWiki Website," 2012. `https://twiki.cern.ch/twiki/bin/viewauth/CMS/PileupJSONFileforData#Calculating_Your_Pileup_Distribu`.

[89] "Wikipedia article on the Crystal Ball function," 2012. `http://en.wikipedia.org/wiki/Crystal_Ball_function`.

[90] The Muon Particle Object Group, "Tag and Probe. TWiki Website," 2012. `https://twiki.cern.ch/twiki/bin/view/CMS/MuonTagAndProbe`.

[91] The Muon Particle Object Group, "Reference muon id and isolation efficiencies. TWiki Website," 2012. `https://twiki.cern.ch/twiki/bin/viewauth/CMS/MuonReferenceEffs`.

[92] E. Navarro and I. Josa, "Muon Efficiencies 2012 in 53X. Presentation in the muon DPG-PH meeting.," 2012. `https://indico.cern.ch/getFile.py/access?contribId=3&resId=0&materialId=slides&confId=214870`.

[93] A. Güth, "Analysis of W and Z production at $\sqrt{s}$=7 TeV with the CMS detector," diploma thesis, RWTH, 2011.

[94] The Muon Particle Object Group, "Reference muon momentum scale and resolution. TWiki Website," 2012. `https://twiki.cern.ch/twiki/bin/viewauth/CMS/MuonReferenceResolution`.

[95] CMS Collaboration, "Missing transverse energy performance of the CMS detector," *JINST* **6** no. 09, (2011) P09001. `http://stacks.iop.org/1748-0221/6/i=09/a=P09001`.

[96] J. Heinrich, C. Blocker, J. Conway *et al.*, "Interval estimation in the presence of nuisance parameters. 1. Bayesian approach," *ArXiv Physics e-prints* (Sept., 2004) , `arXiv:physics/0409129`.

[97] J.-F. Schulte, "Search for heavy charged gauge bosons in the decay channel $W' \to e\nu$ with CMS data," Master's thesis, RWTH, 2012.

[98] I. N. Bronstein *et al.*, *Taschenbuch der Mathematik*. Verlag Harri Deutsch, Frankfurt am Main, 6. ed., 2005.

[99] CMS Collaboration, "Search for High-Mass Resonances Decaying to Electron Pairs in the CMS Experiment with 4.7 fb^{-1} of data," *CMS Analysis Note AN-11-444* .

[100] P. Millet, "Private communication," 2012.

Selbständigkeitserklärung

Hiermit versichere ich, dass ich die Arbeit selbständig verfasst und keine anderen als die angegebenen Quellen und Hilfsmittel benutzt sowie Zitate kenntlich gemacht habe.

Fabian Schneider

Aachen, den 21. 12. 2012